AD-A256 690

PL-TR-92-2126

THE EARTH'S RADIATION BELTS, AURORAL ZONES, AND POLAR CAPS: PARTICLE MODELS, EVENT STUDIES, AND EFFECTS ON MATERIALS

R. L. Carovillano

Boston College
140 Commonwealth Avenue
Chestnut Hill, MA 02167-3800

DTIC
ELECTE
SEP 2 5 1992
S   D

16 April 1992

Final Report
30 April 1986-31 December 1991

APPROVED FOR PUBLIC RELEASE; DISTRIBUTION UNLIMITED
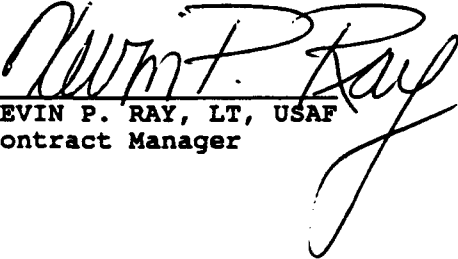
PHILLIPS LABORATORY
AIR FORCE SYSTEMS COMMAND
HANSCOM AIR FORCE BASE, MASSACHUSETTS 01731-5000

92 9 24 028

92-25804

"This technical report has been reviewed and is approved for publication"

KEVIN P. RAY, LT, USAF
Contract Manager

E. G. MULLEN
Branch Chief

WILLIAM SWIDER
Deputy Director

This document has been reviewed by the ESD Public Affairs Office (PA) and is releasable to the National Technical Information Service (NTIS).

Qualified requestors may obtain additional copies from the Defense Technical Information Center. All others should apply to the National Technical Information Service.

If your address has changed, or if you wish to be removed from the mailing list, or if the addressee is no longer employed by your organization, please notify PL/TSI, Hanscom AFB, MA 01731. This will assist us in maintaining a current mailing list.

Do not return copies of this report unless contractual obligations or notices on a specific document requires that it be returned.

REPORT DOCUMENTATION PAGE

Public reporting burden for this collection of information is estimated to average 1 hour per response, including the time for reviewing instructions, searching existing data sources, gathering and maintaining the data needed, and completing and reviewing the collection of information. Send comments regarding this burden estimate or any other aspect of this collection of information, including suggestions for reducing this burden, to Washington Headquarters Services, Directorate for Information Operations and Reports, 1215 Jefferson Davis Highway, Suite 1204, Arlington, VA 22202-4302, and to the Office of Management and Budget, Paperwork Reduction Project (0704-0188), Washington, DC 20503.

1. AGENCY USE ONLY (Leave blank)	2. REPORT DATE April 16, 1992	3. REPORT TYPE AND DATES COVERED FINAL 30 APR. 1986–31 DEC. 1991

4. TITLE AND SUBTITLE "The Earth's Radiation Belts, Auroral Zones, and Polar Caps: Particle Models, Event Studies, and Effects on Materials"	5. FUNDING NUMBERS F19628-86-C-0029
6. AUTHOR(S) R. L. Carovillano	PR 62101F PR 7601 TA 20 WUAB

7. PERFORMING ORGANIZATION NAME(S) AND ADDRESS(ES) Boston College 140 Commonwealth Avenue Chestnut Hill, MA 02167-3800	8. PERFORMING ORGANIZATION REPORT NUMBER

9. SPONSORING/MONITORING AGENCY NAME(S) AND ADDRESS(ES) Phillips Laboratory Hanscom AFB, MA 01731-5000 Contract Manager: Lt. Kevin Ray/GPSP	10. SPONSORING/MONITORING AGENCY REPORT NUMBER PL-TR-92-2126

11. SUPPLEMENTARY NOTES

12a. DISTRIBUTION/AVAILABILITY STATEMENT APPROVED FOR PUBLIC RELEASE: DISTRIBUTION UNLIMITED	12b. DISTRIBUTION CODE

13. ABSTRACT (Maximum 200 words)

Projects include: (1) An empirical DMSP data base of the most poleward ion precipitation boundary: The data base was analyzed statistically and analytically. At each MLT there is great variance, and the ion boundary correlates best with AE. The average boundary is a circle offset from the geomagnetic pole that expands with geomagnetic activity. (2) An analytical model of convection and currents in the height-integrated ionosphere coupled to field aligned currents: Results include the effect of the auroral conductivity; the deterministic coupling between Region I and Region II currents; the generation of auroral electrojet currents; the electrical shielding of low latitudes; two cell and multiple cell convection patterns; and conductivity gradient effects. (3) Energy dispersion discovered at the ion polar cap boundary: Interpretations have the ions originating in the plasma sheet boundary layer. (4) Various tasks and services with Air Force data bases: Tasks included particle event studies, the auroral boundary index, the polar rain index, and several CRRES projects including the static radiation belt model. Services included algorithm development, provision for data storage, access, and documentation.

14. SUBJECT TERMS Ion dispersion; empirical ion polar cap boundary, analytical fit, statistical analysis and magnetic activity dependence; ionospheric convection, field aligned currents; CRRES, DMSP, SCATHA, and P78-1 data bases, THDB, auroral boundary index, polar rain index.	15. NUMBER OF PAGES 172
	16. PRICE CODE

17. SECURITY CLASSIFICATION OF REPORT UNCLASSIFIED	18. SECURITY CLASSIFICATION OF THIS PAGE UNCLASSIFIED	19. SECURITY CLASSIFICATION OF ABSTRACT UNCLASSIFIED	20. LIMITATION OF ABSTRACT SAR

TABLE OF CONTENTS

DTIC QUALITY INSPECTED 3

LIST OF FIGURES

LIST OF TABLES

AUTHOR CREDITS

Author credits to this final report are listed below by chapter. The persons named made noteworthy contributions to at least a portion of the work described.

Chapter 2: R. L. Carovillano, N.C. Heinemann, E. K. Grimes

Chapter 3: R. L. Carovillano, L. Zhang

Chapter 4: H.- C. Yeh, R. L. Carovillano, N. C. Heinemann, A. M. Martel, M. S. Gussenhoven, D. A. Hardy.

Chapter 5: Daniel Madden, M. S. Gussenhoven, E. Holeman

1. INTRODUCTION

This report presents or summarizes the work done to meet contract objectives. The scope of the research performed includes theoretical and empirical modelling of the earth's radiation belts and the polar caps, performing case studies of events observed by Air Force satellites, and the development of models and numerical codes on the effects on materials of energy deposited in sensitive regions of space by characteristic nuclear processes.

A significant number of contract objectives were met in the successful completion of four separate subcontracts. The other tasks performed are reported in this document. Because of the delay in the lanch of the Combined Release and Radiation Effects Satellite (CRRES) resulting from the Challenger disaster, the original contract plan was greatly descoped in manpower level and tasks.

The organization of this report is as follows. The determination of an empirical data base for the poleward boundary of ion precipitation as determined from Air Force satellites is described in Chaper 2. An extensive statistical analysis was performed on the data base to determine regularities in location and the correlations between the ion boundary location and parameters such as AE, Kp, and the interplanetary magnetic field (IMF). At each MLT the empirical ion boundary displayed considerable variance and a modest correlation at best with any magnetic activity parameter. Nevertheless, the *average* ion boundary shows great regularity in MLT and activity. Thus, functional fits are made to the average ion poleward boundary, and heuristic parameters are introduced that represent properties associated with the polar cap.

Chapter 3 consists of a description of the analytical model developed on the global distribution of ionospheric electric fields and currents as determined in the compling to field aligned currents (FACs). The objective in this work is to display the many physical effects that result from the many variables that participate in the coupling. Region I currents, Region II currents, and the so-called DPZ and DPY currents are introduced seriatim. The model developed uses height-integrated Hall and Pedersen conductivities and represents the ionosphere as a spherical shell. The auroral zone may have an enhanced conductivity compared to the polar cap and the sub auroral zone. Day-night conductivity gradients are not included.

Chapter 4 describes the discovery and analysis of energy dispersion events observed in precipitating ions at the poleward edge of the night side auroral oval. The events are observed in the energy range 30 eV to 30 keV by the DMSP SSJ/4 detectors on the low altitude (840 km) F6 and F7 satellites. The dispersion in the precipitating ions may extend from a few keV to 30 keV,

the lower limit being an observational criterion and the upper limit set by the SSJ/4 instrument. The ion dispersion events have a limited spatial extent (From a practical lower limit of about 75 km to several hundred kilometers) and consist of high intensity keV ion precipitation at times just poleward of an inverted-V during active magnetic conditions. Interpretations are suggested which designate the source particles of the observed dispersion to be ions in the plasma sheet boundary layer (PSBL). The observed disperison results from the PSBL ions moving earthwards along a flux tube and $E \times B$ drifting from about 15-20 R_E. The low altitude dispersion is distributed along the local convection trajectory. In the field-aligned motion, higher energy ions arrive at low altitudes before lower energy ions, and the convection of the low altitude flux tube during the difference in arrival times produces the low altitude dispersion in energy. The latitudinal scale of the events is small and reflects the narrowness of the PSBL.

In Chapter 5 a description is given of services provided to scientists wishing to access Air Force particle data bases and of tasks performed on certain of these data bases. The tasks include contributions to particle event studies, extending the catolog of values for the auroral boundary index, development of the polar rain index, and several CRRES projects including the static radiation belt model. Services include algorithm development, provision for data storage, access, and documentation.

2. POLEWARD BOUNDARY OF ION PRECIPITATION

A. Introduction

Observations from DMSP F6 and F7 satellites have been used to determine the most poleward latitude at which ions precipitate. With varying degrees of coverage, all magnetic local times (MLT) are included in the data base enabling us to construct a poleward boundary of ion precipitation as a function of chosen parameters. The assembled ion boundaries may then be regarded to represent, empirically or statistically in terms of ions, the poleward boundary of the aurora, the equatorward boundary of the polar rain, or the "polar cap" boundary.

The polar cap is of interest theoretically [e.g., *Siscoe and Cummings*, 1969; *Coroniti and Petcheck*, 1972] because it may reflect properties of basic processes such as magnetic merging. In particular, the concept of flux in the polar cap as a measure of the flux in the magnetotail is used by numerous models [e.g., *Siscoe*, 1982; *Siscoe and Huang*, 1985; *Moses and Siscoe*, 1988; *Moses et al.*, 1987, 1989]. This relates to the positive correlation of substorm occurrence and southward interplanetary magnetic field (IMF) which is widely interpreted in terms of magnetic merging wherein magnetic flux is transferred from the IMF to open magnetospheric field lines originating in the polar cap. At the beginning of the merging process and prior to the onset of reconnection in the tail region, the amount of energy transferred to the magnetosphere is proportional to the increase in polar cap magnetic flux which, in turn, is proportional to the size (area) of the polar cap (*Holzer and Slavin*, 1978, 1979). In this regard, and also in common use, the "polar cap" consists of the high latitude region of open field lines with direct connection to the interplanetary magnetic field. Unfortunately, this notion provides only a poor working definition of the polar cap since it is not specific when applied to measurable quantities. Nevertheless, for quantifiable tracking of energy transfer in a process which depends on the identification of the polar cap, such as magnetic merging, an empirical specification of the polar cap boundary is useful or necessary. The boundary has been defined in various ways from different, measured quantities. These

boundaries are not necessarily coincident, even with the same type of measurement. We briefly review some of the current empirical determinations or definitions of the polar cap below.

Several reports on the determination of the polar cap boundary have been made from auroral images [*Meng et al.*, 1977; *Nakai and Kamide*, 1983; *Holzworth and Meng*, 1984 (DMSP); *Craven and Frank*, 1985, 1987 (DE-1); *Shepherd et al.*, 1989 (VIKING)] which provide the most global, essentially instantaneous, picture of a boundary that encloses the polar cap.

Particle measurements that relate to the polar cap boundary have also been made (*Frank and Ackerson*, 1972; *Hoffman and Burch*, 1973; *Winningham et al.*, 1975; *Makita and Meng*, 1984; *Meng and Makita*, 1986; *Makita et al.*, 1983, 1988; *Lassen et al.*, 1988), though the relationship between precipitating particles and the location of the polar cap boundary is not settled. *Heelis et al.* (1980), *Bythrow et al.* (1981), *Torbert et al.* (1981), *Makita et al.* (1983), and *Meng and Makita* (1985) among others define the open-closed field line boundary as the equatorward boundary of the polar rain. This boundary presumably would be the low altitude mapping of the boundary between the lobe and the boundary plasma sheet, following the definitions of *Winningham et al.* (1975). Recently, however, *Holzer et al.* (1986) have used the boundary between the central plasma sheet and the boundary plasma sheet (again as defined by *Winningham et al.*, 1975) to delineate the open field line region in their magnetic flux transfer model, and concluded that this boundary gives a better measure of flux transfer to the magnetosphere than does the equatorward polar rain boundary.

Polar cap boundary definitions have also been proposed using low altitude convection data. *Gurnett and Frank* (1973) suggested that the boundary between open and closed field lines lies in the region where the reversal from sunward to anti-sunward plasma convection occurs. *Eastman et al.* (1976) proposed, however, that there should be a confined region of anti-sunward flow on closed field lines. *Heelis et al.* (1980) gave further evidence for this in their analysis of Atmospheric Explorer data, by showing that the convection reversal is equatorward of the polar rain boundary, which was their open/closed field line boundary. Despite these possible adjustments, *Reiff et al.* (1981) used the convection reversal as the polar cap boundary to good

effect in calculating the polar cap potential drop. The cross-cap potential difference is a quantitative measure of the strength of solar wind-magnetospheric coupling, and is a major consideration in large scale magnetospheric models such as the Rice Convection Model (*Wolf*, 1983) which have reproduced many features of magnetospheric-ionospheric dynamics using the cross-cap potential difference as an initial condition.

Field-aligned currents are also used to delineate the polar cap boundary. *Iijima and Potemra* (1976) defined Region I and II current sheets, located at auroral latitudes, as roughly coinciding with discrete and diffuse auroral regions, respectively. If Region I currents are at the boundary of or on open field lines, as suggested by the current driving mechanisms of *Stern* (1983), then the Iijima and Potemra observations place discrete auroras on open field lines in agreement with the work of *Holzer et al.* (1986). Using AE-C data, *Coley* (1983) concluded that both Region I and II currents normally occur on closed field lines and that significant particle precipitation spans both current sheets.

What emerges from these studies and others is a set of observations from which it is difficult to extract a unique empirical definition of the polar cap boundary that is in every case consistent with current notions of open and closed field line processes. The polar cap boundary definitions depend upon the type of data used and how the complex hierarchy of physical processes is ordered by an individual researcher of research group. The empirical relationships among particle precipitation, field-aligned currents, and ionospheric convection patterns are not yet clearly established, and more definitive observations are needed to establish such relationships and the dynamical nature of the relationships.

B. Instrumentation and Data Overview

<u>Orbits and Instrumentation</u>. Ion poleward boundaries were determined using measurements from DMSP F6 and F7 satellites which are in sun-synchronous, circular, polar orbits. The orbits are centered approximately on the 0600-1800 and 1030-2230 magnetic local time (MLT) meridians, respectively. The DMSP satellites are at an altitude of 840 km, with an orbital period of

101 minutes and a geographical inclination of 99°. Because of the offset between the geomagnetic and geographic poles, the DMSP satellites sweep out a large portion of the auroral regions each day. At corrected geomagnetic latitudes above 70° where nearly all poleward particle precipitation boundaries occur, all MLT's are traversed.

Each satellite has two SSJ/4 sensors, one to measure electrons and one ions. Each sensor consists of two cylindrical electrostatic analyzers that measure the particle flux in 20 channels, spaced logarithmically in energy from 30 eV to 30 keV. The satellites are three-axis stabilized and each detector is mounted such that its look direction always points toward the local vertical, thus measuring precipitating rather than backscattered or trapped particles. The geometric factor of the low energy (30 eV to 1 keV) ion analyzer is 3.2×10^{-2} cm^2 sr with $\Delta E/E = 9.8\%$. The geometric factor of the high energy (1 keV to 30 keV) ion analyzer is 8.6×10^{-4} cm^2 sr with $\Delta E/E = 9.3\%$. The geometric factors for the ion detectors are unusually large compared to others flown at similar altitudes, resulting in count levels well above background in the auroral oval. The ion detectors employ a post acceleration of 1000 volts to provide channeltron efficiency at low energies. Details of the detectors and their calibration are given by *Hardy et al.*, [1984].

Data overview. Figure 1 is a survey plot of data collected by DMSP F7 over the north pole on 18 January 1984. Figure 1, Panel A shows ions; Panel B, electrons. In each panel, the following are plotted, from top to bottom, as a function of universal time in seconds: the particle average energy (EAVE) in keV; the particle total energy flux (JETOT) in keV/cm^2 s sr; and the total particle number flux (JTOT) in particles/cm^2 s sr. The geographic latitude and longitude (GLAT and GLON) at the subsatellite position; and the corrected geomagnetic latitude, longitude and magnetic local time (MLAT, MLON and MLT) mapped to 110 kilometers, are given every two minutes.
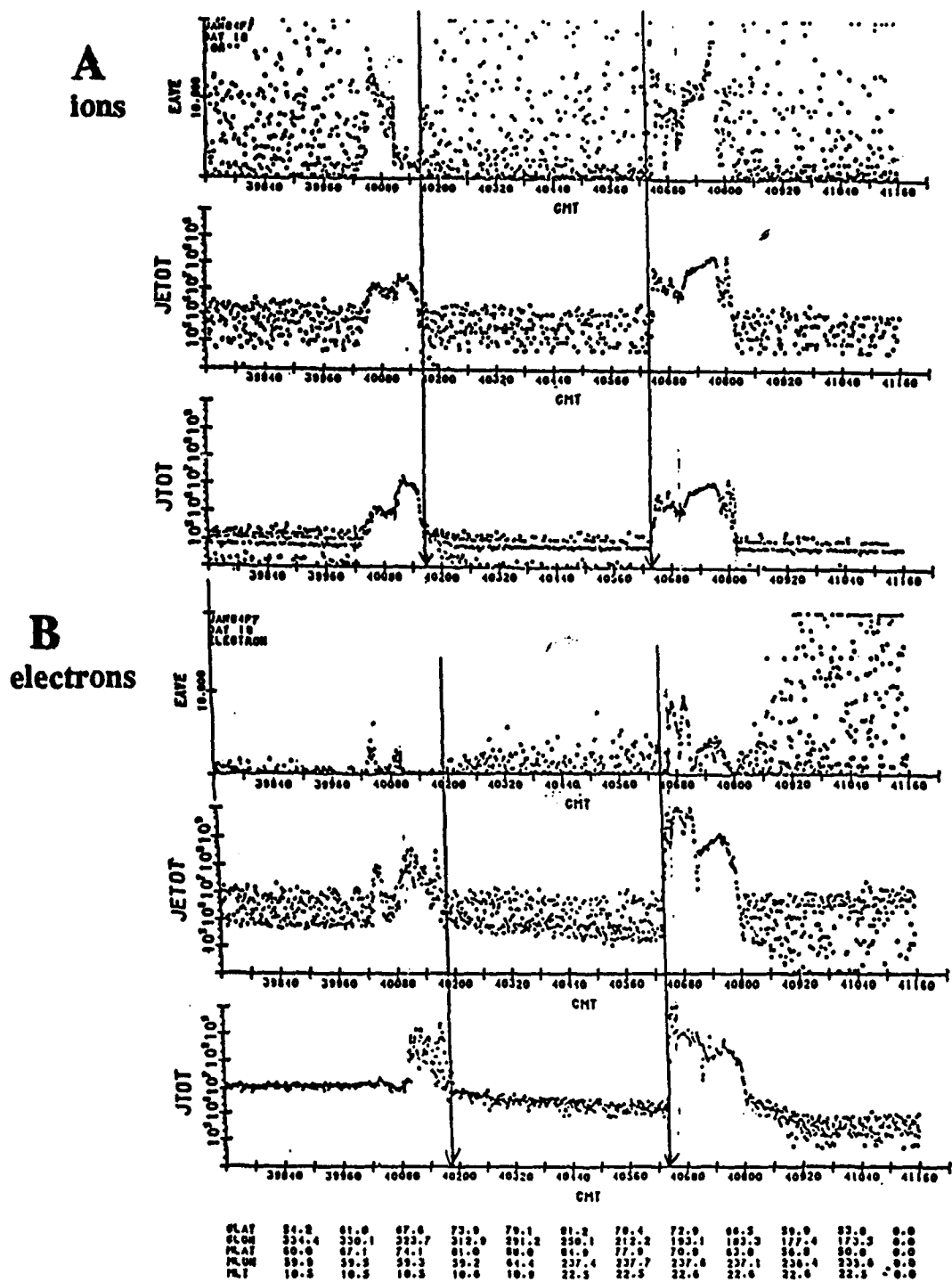
Figure 1 A. Integral flux in (cm² s sr)⁻¹ (bottom panel), energy flux in keV/cm² s sr (middle panel), and average energy in keV (top panel) of precipitating ions measured by the DMSP F7 satellite over the north pole on January 18, 1984. B. The same format as in part A, but for precipitating electrons. The abscissa gives the universal time (in seconds), geographic latitude and longitude, corrected geomagnetic latitude and longitude and magnetic local time. The magnetic coordinates are projected along the magnetic field to an altitude of 110 km. The vertical lines mark ion (A) and electron (B) poleward boundary choices that are unambiguous, but not the same.

A simple criterion is used to determine the ion poleward boundaries. Figure 1A gives an example. Beginning at the most poleward point of the orbit (near the center of the pass) and moving toward the auroral zones, the poleward boundary of ion precipitation is chosen where a clear rise in the ion number flux (JTOT) occurs, which is not followed by a clear return to polar cap precipitation levels. This criterion works well in the example and in nearly all cases. In Figure 1A the ion poleward boundaries are marked by an arrow on the JTOT scale, at 40164 UT on the dayside and at 40640 UT on the night side. In this pass the poleward electron boundaries (shown by arrows in Figure 1B) are about the same as the ion poleward boundaries on the dayside and identical on the nightside. All boundaries are unambiguous.

Figure 2 illustrates ion and electron measurements where the electron precipitation profile is quite different from that shown in Figure 1B. The format of the plot, which shows data measured by DMSP F7 during an earlier north pole pass on 18 January 1984, is identical to Figure 1. The ion poleward boundaries shown in Figure 2A at 28180 UT on the dayside and at 28600 UT on the nightside are unambiguous, but it is not clear where to locate the electron poleward boundaries. While it is nearly always possible to choose the ion poleward boundary with certainty, poleward electron boundaries may be obscured by precipitation across the polar cap as much as 50% of the time (*Hardy*, 1984). It is an advantage to use precipitating ion data for studies of the poleward auroral boundary.

C. Ion Poleward Boundary Data Bases

The ion poleward boundaries used in this study were measured by the DMSP F6 and F7 satellites, mostly in the early months of 1984 when Interplanetary Magnetic Field (IMF) data coverage was most complete. The full data base assembled is denoted D(all) and consists of 2319 ion precipitation boundaries determined using the criterion described above. For each measured event in D(all), the values of MLAT, MLT, UT, AE, and Kp were recorded. IMF By and IMF Bz were also recorded for a subset of the full data base consisting of 1466 ion boundaries. The latter
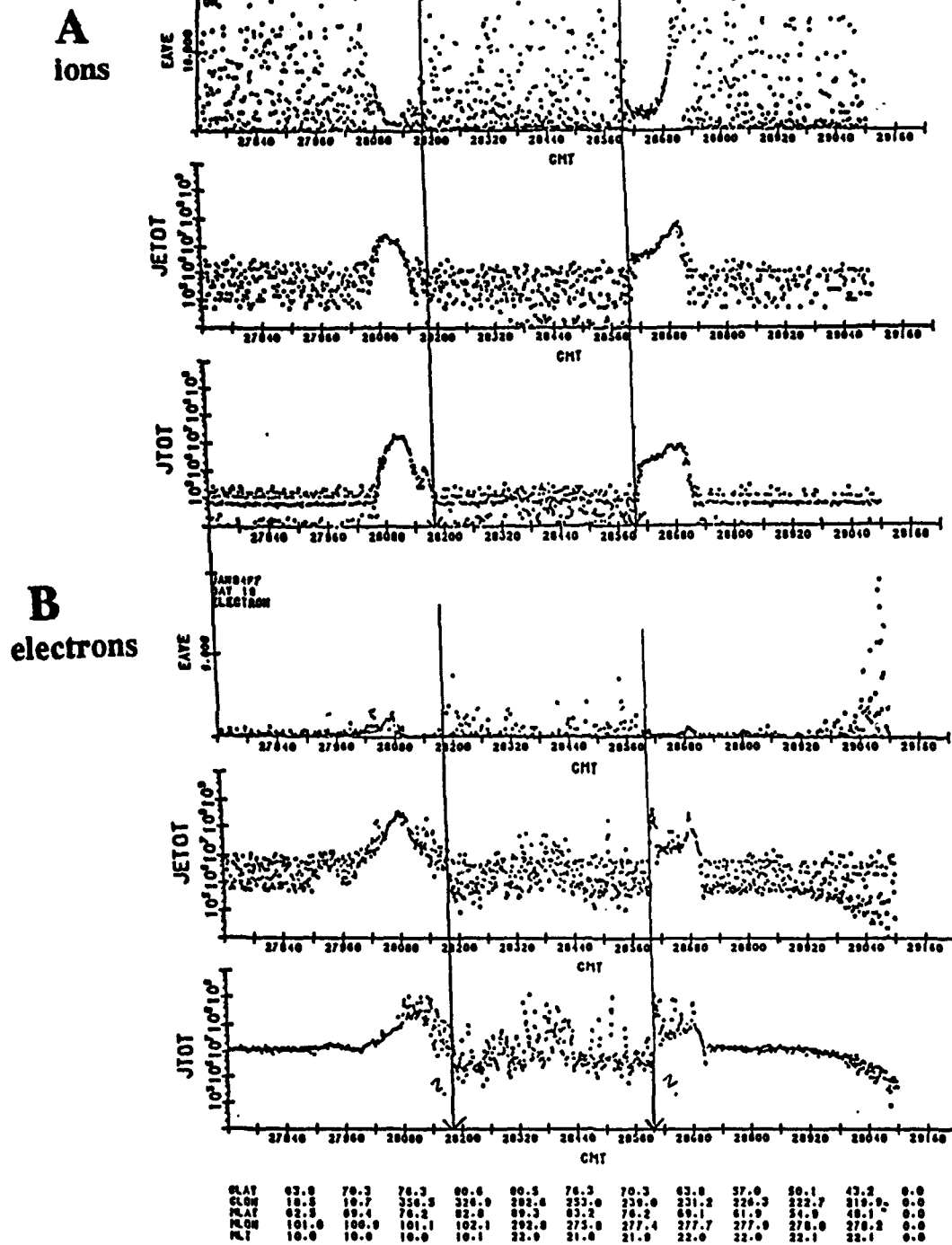
Figure 2. A plot for 4 January 1980 in the same format as Figure 1. In this case, the ion (A) poleward boundary choices are clear, while the electron (B) poleward boundary choices are not.

data base is denoted D(IMF). The 3-hour Kp averages and the one-hour AE averages are from standard sources. Hourly averaged values of IMF By and Bz were offset in time as follows to allow for propagation by the solar wind. If the UT at which the boundary was measured is before the half hour of its UT hourly interval, the hourly averaged value of IMF By (and Bz) from the previous hour is used. If the UT of the measured boundary is after the half hour in a UT hourly interval, the IMF By (and Bz) hourly averaged value for that UT hour is used. Because it has been reported that the poleward boundary of the aurora is offset such that the geomagnetic pole is not at the geometric center of the area enclosed by the poleward boundary (e.g., *Meng et al.*, 1977), the poleward boundaries were also sorted into one hour MLT bins.

Some overall characteristics of the two data bases are as follows. The averages and standard deviations of the latitude λ (in degrees) and the magnetic parameters are given in Table 1.

TABLE 1. Averages and standard deviations of data base parameters.

Data base:	D(all)	D(IMF)
λ :	75.1 (4.45)	75.0 (4.32)
AE :	305 (274)	296 (247)
Kp :	3.05 (1.64)	3.03 (1.59)
IMF Bz :	----	-0.555 (3.54)
IMF By :	----	0.783 (4.61)

Averages and standard deviations (in parentheses) are given for the latitude λ in degrees and the magnetic parameters for the data bases D(all) and D(IMF). AE and the IMF are in nT.

The correlation coefficient between two parameters A and B is denoted r(A,B). The correlation coefficients among the parameters in D(all) are:

$$r (\lambda, AE) = -0.39$$

$$r (\lambda, Kp) = -0.34$$

$$r (AE, Kp) = 0.76$$

The correlation coefficients among the parameters in D(IMF) are given in Table 2.

There is little difference in any of the averages and correlation coefficients in the two data bases D(all) and D(IMF), as should be expected. Also, the latitude of the ion boundary correlates weakly, at best, with any of the magnetic parameters. The only appreciable correlation is between AE and Kp, which approaches 0.8. With these uninspiring results, one might look forward with anticipation to sorting the data by MLT. Thus the averages, standard deviations, and correlation coefficients are given for each MLT for D(all), in Table 3.

TABLE 2. Correlation coefficients among parameters in D(IMF).

	IMF By	IMF Bz	AE	Kp
λ	0.06	0.28	-0.34	-0.27
IMF By		0.20	0.13	0.23
IMF Bz			-0.48	-0.39
AE				0.78

The matrix of numbers gives the correlation coefficients for the parameters labeling the columns and rows. Thus, r(AE, Kp) = 0.78.

Several interpretations are suggested by Table 3. The average location of the ion poleward boundary is about $(79\pm3)^\circ$ at local noon and about $(73\pm4)^\circ$ at local midnight. The average latitude is higher at dawn than dusk suggesting roughly a 1 to 2 degree offset or shift of the boundary "center" towards dusk. AE and Kp correlate well at each MLT. The boundary location λ correlates slightly better with AE than Kp at most MLT. The boundary correlation tends to be poorest within two or three hours of midnight and best near local noon. The latter comment is tempered by the comparitively small number of measurements in the cusp region.

Similar results and comments apply to the smaller data base D(IMF) when separated by MLT. The added information comes from the IMF. All correlations with IMF By are small, and the correlation coefficient $r(\lambda, By)$ is particularly small, rarely exceeding 0.2. The remaining correlation coefficients are listed in Table 4. At most MLTs, the ion boundary λ correlates best with AE, next best with Kp then IMF Bz though the ordering is not pronounced. The strongest and most consistent correlation is between AE and Kp, which is of no particular significance to the boundary study itself. IMF Bz correlates better and more consistently in MLT with AE than with Kp, though the correlation is never strong.

D. Linear Regression Analyses

Calculations were performed to determine the best linear description of the ion boundary location. The boundary is represented by

$$\hat{\lambda}(x) = a + b x \qquad (1)$$

where $\hat{\lambda}$ is the "predicted" or theoretical boundary latitude and the regressor, x is the magnetic activity parameter. A least squares fit to the data is used to determine the regression coefficients, a and b, for each MLT. In turn, we present the results for x given by Kp, AE, and IMF Bz.

Kp. Using Kp as the regressor, the determined regression coefficients are given in Table 5. Also given in Table 5 is $r(\lambda, \hat{\lambda})$, i.e., the correlation coefficient between the observed are predicted boundary latitude. The correlation is generally poorest on the night side and best on the day side. Figure 3 is presented to complement Table 5 and to display the quality of the fit at the selected MLT intervals 00-01 and 09-10. In Figure 3A, the straight line is the linear regression fit to the data, with the equation for the fit and the correlation coefficient $r(\lambda, \hat{\lambda})$ shown in the upper right taken from Table 5. Also shown in Figure 3A are the average ion poleward boundary and standard deviation for each whole level of Kp (grouped according to 0, 0+; 1-, 1, 1+; ...; $\geq$5-).

12

TABLE 3. Statistical properties of D(all) by MLT.

MLT	#	latitude	AE	Kp	r(λ,AE)	r(λ,Kp)	r(AE,Kp)
0	90	72.7(3.96)	294(229)	2.94(1.69)	-0.13	-0.13	0.80
1	98	74.3(3.27)	274(223)	2.89(1.43)	-0.15	-0.08	0.71
2	90	74.9(3.74)	279(222)	2.72(1.37)	-0.23	-0.10	0.70
3	109	76.2(3.93)	274(245)	2.78(1.79)	-0.47	-0.45	0.86
4	144	76.2(3.47)	274(215)	3.06(1.55)	-0.27	-0.27	0.82
5	127	77.2(4.26)	286(257)	2.84(1.61)	-0.55	-0.49	0.82
6	136	77.8(3.59)	270(231)	3.03(1.58)	-0.55	-0.46	0.78
7	71	77.7(3.90)	279(289)	2.86(1.68)	-0.56	-0.54	0.83
8	81	78.2(3.50)	281(235)	3.08(1.65)	-0.60	-0.51	0.76
9	78	77.3(3.98)	377(326)	3.48(1.77)	-0.75	-0.76	0.84
10	88	78.6(3.26)	333(342)	3.20(1.80)	-0.77	-0.66	0.79
11	19	79.7(3.41)	336(240)	3.09(1.44)	-0.58	-0.47	0.81
12	16	78.1(3.23)	438(317)	3.75(1.69)	-0.72	-0.78	0.90
13	35	77.5(3.46)	398(258)	3.44(1.38)	-0.68	-0.50	0.77
14	18	78.0(4.72)	278(247)	2.79(1.65)	-0.78	-0.79	0.62
15	18	76.1(5.17)	299(251)	3.20(1.50)	-0.83	-0.79	0.71
16	49	74.0(4.95)	437(324)	3.60(1.74)	-0.77	-0.68	0.81
17	78	76.3(4.76)	265(263)	2.95(1.43)	-0.61	-0.67	0.74
18	120	74.7(4.25)	313(242)	3.29(1.56)	-0.53	-0.55	0.80
19	155	74.9(4.23)	314(282)	3.18(1.71)	-0.61	-0.51	0.81
20	132	73.0(4.66)	331(279)	2.99(1.53)	-0.58	-0.53	0.79
21	159	73.0(3.66)	291(246)	2.88(1.45)	-0.22	-0.19	0.78
22	247	72.3(3.21)	273(256)	2.99(1.63)	-0.14	-0.16	0.78
23	161	72.6(3.95)	265(247)	2.82(1.61)	-0.13	-0.14	0.80

The first column denotes the beginning of the one-hour MLT interval. The second column gives the number of measured ion boundaries in the MLT bin. The next three columns give the average and standard deviation by MLT for the latitude in degrees, AE, and Kp, respectively. The final three columns give the correlation coefficients among the parameters by MLT.

TABLE 4. Correlation coefficients of parameters by MLT for D(IMF).

MLT	#	r(λ,Bz)	r(λ,AE)	r(λ,Kp)	r(Bz,AE)	r(Bz,Kp)	r(AE,Kp)
00	62	0.23	-0.06	-0.06	-0.57	-0.38	0.77
01	71	0.25	-0.12	-0.09	-0.49	-0.39	0.72
02	59	0.19	-0.06	0.05	-0.56	-0.26	0.72
03	67	0.45	-0.49	-0.38	-0.56	-0.58	0.85
04	99	0.31	-0.14	-0.13	-0.26	-0.22	0.83
05	78	0.53	-0.50	-0.36	-0.49	-0.46	0.78
06	78	0.27	-0.50	-0.40	-0.49	-0.40	0.77
07	48	0.47	-0.57	-0.49	-0.51	-0.61	0.80
08	48	0.40	-0.63	-0.57	-0.41	-0.48	0.76
09	45	0.48	-0.82	-0.77	-0.55	-0.36	0.88
10	50	0.53	-0.61	-0.48	-0.44	-0.35	0.71
11	12	0.45	-0.58	-0.48	-0.32	-0.09	0.85
12	9	0.81	-0.74	-0.81	-0.56	-0.69	0.94
13	22	0.38	-0.65	-0.43	-0.55	-0.50	0.77
14	15	0.41	-0.75	-0.78	-0.54	-0.05	0.59
15	15	0.61	-0.80	-0.77	-0.62	-0.57	0.69
16	29	0.32	-0.56	-0.42	-0.60	-0.64	0.88
17	52	0.34	-0.56	-0.65	-0.35	-0.20	0.70
18	68	0.37	-0.53	-0.54	-0.45	-0.46	0.79
19	99	0.37	-0.57	-0.43	-0.50	-0.48	0.78
20	79	0.45	-0.54	-0.48	-0.44	-0.28	0.79
21	112	0.28	-0.21	-0.12	-0.44	-0.18	0.75
22	149	0.26	-0.16	-0.16	-0.51	-0.43	0.78
23	100	0.18	-0.14	-0.10	-0.52	-0.41	0.81

In the table, Bz denotes IMF Bz and the second column (#) gives the total number of measurements by MLT. The remaining columns give the indicated correlation coefficients.

Figure 3B is the same as Figure 3A, but for the ion poleward boundaries measured between 09-10 MLT. Despite the great scatter of the data, the linear regression fit (solid line) accurately represents the *average* boundary location (dashed line). The average ion poleward boundaries vary quite smoothly with magnetic activity at each MLT. Similar fits have been calculated for each one-hour MLT bin with similar results.

Table 5. Kp Linear Regression Ion Boundary Parameters.

MLT	#	a	b	$r(\lambda, \hat{\lambda})$
00-01	90	73.6	-0.31*	-0.13
01-02	98	74.9	-0.18*	-0.08
02-03	90	75.7	-0.28*	-0.10
03-04	109	78.9	-0.98	-0.45
04-05	144	78.1	-0.61	-0.27
05-06	127	81.0	-1.31	-0.49
06-07	136	81.0	-1.04	-0.46
07-08	71	81.2	-1.24	-0.54
08-09	81	81.5	-1.09	-0.51
09-10	78	83.2	-1.70	-0.76
10-11	88	82.5	-1.20	-0.66
11-12	19	83.1	-1.10	-0.47
12-13	16	83.7	-1.50	-0.78
13-14	35	81.3	-1.25	-0.50
14-15	18	84.3	-2.25	-0.79
15-16	18	84.9	-2.73	-0.79
16-17	49	80.9	-1.92	-0.68
17-18	78	82.9	-2.24	-0.67
18-19	120	79.6	-1.48	-0.55
19-20	155	78.9	-1.26	-0.51
20-21	132	77.8	-1.60	-0.53
21-22	159	74.4	-0.48	-0.19
22-23	247	73.3	-0.31	-0.16
23-00	161	73.6	-0.33*	-0.13

Table 5. Linear regression results, ion boundary latitude versus Kp. The column headings are MLT, the number of observations #, the linear regression coefficients a and b of equation (1), and the correlation coefficient $r(\lambda, \hat{\lambda})$ between the observed boundary and the boundary predicted by the linear regression analysis. The asterik (*) following values of the slope b indicate a t-value of less than 2.

A
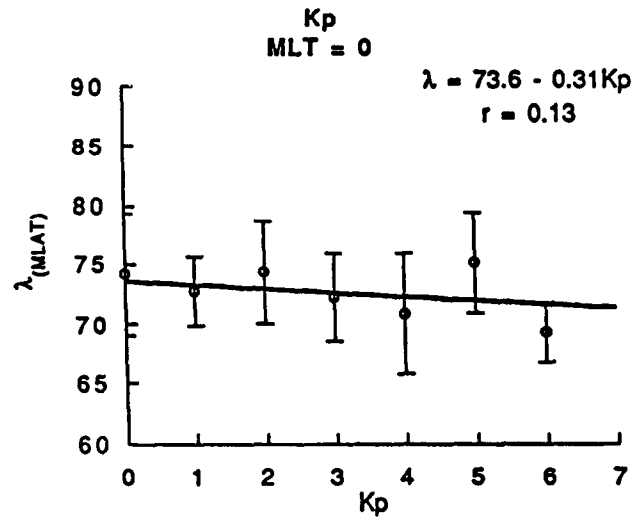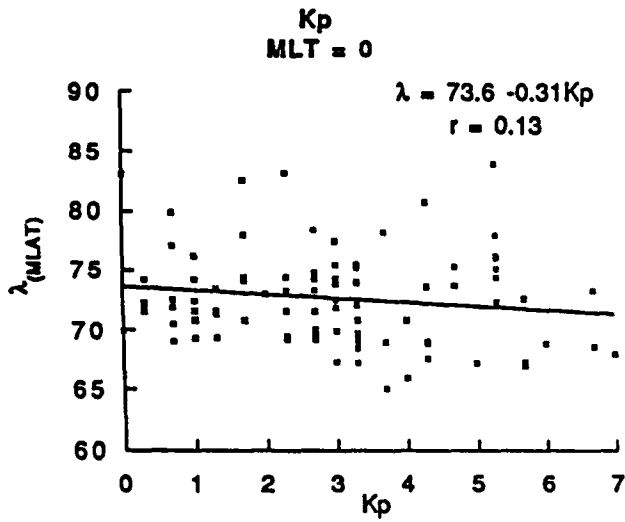
B
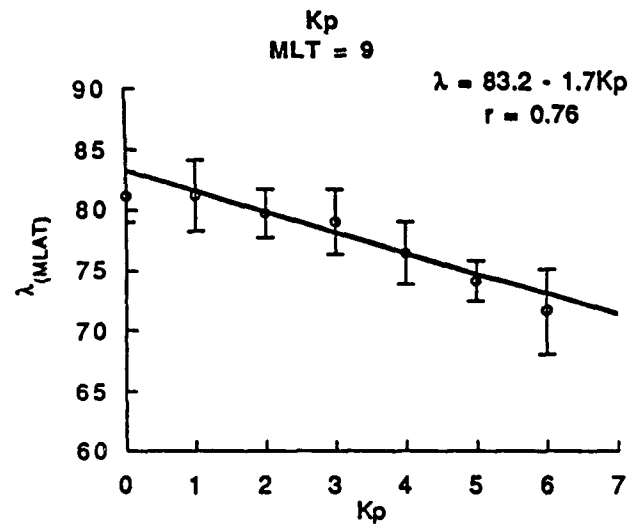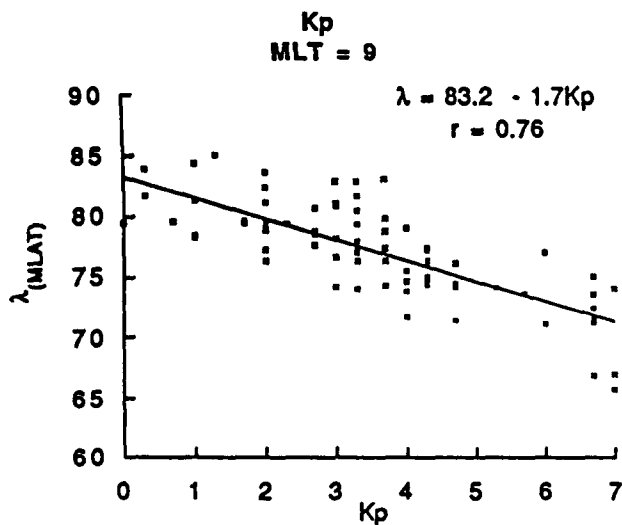
Figure 3 A. Mean values and standard deviations in each Kp bin for the ion poleward boundaries as a function of Kp for the 0000-0100 MLT sector. The solid line is the predicted fit from the linear regression analysis. The dashed line is the linear fit to the average latitude in the seven bins according to the Kp value. The equations for the two linear fits are given on the top right of the plot, along with the correlation coefficient, r. B. The same as A, but for the 0900-1000 MLT sector.

Some immediate conclusions may be drawn from Table 5 (illustrated by Figure 3):

1. The ion poleward boundary reaches the highest latitudes on the dayside (the cusp and cleft regions) and the lowest latitudes near midnight, as expected. The rather crude dawn-dusk symmetry of the boundary suggests at least that the "center" of the ion poleward boundary curve is offset from the noon-midnight meridian.

2. Since the regression coefficient b is always negative, the ion poleward boundary expands equatorward at all MLT with increasing Kp. The rate of expansion is least for the three hour MLT bins before and the three after midnight. The largest rate of expansion with Kp takes place late in the afternoon.

3. There is a significant change in the regression coefficients going from midnight in the MLT bins towards dawn and dusk, both in the location of the ion poleward boundary and its movement towards lower latitudes with increasing Kp. The movement to lower latitudes seems to be largest on the dayside, but because of the small number of data points at some dayside MLTs, the result may not be conclusive.

4. The scatter of the boundary location as reflected in the standard deviations is greater at 00-01 MLT than at 09-10 MLT as is shown in Figure 3. The other MLT bins near midnight also show considerable scatter, indicating that the ion poleward boundary location on the nightside is more variable than on the dayside for any Kp level.

In cases where the correlation coefficient $r(\lambda, \hat{\lambda})$ is very small (generally at MLTs within three hours of midnight) an improved fit can be obtained with a higher order polynomial. Thus, a fifth order polynomial fit in Kp increases the correlation coefficient at 00 MLT from 0.13 to 0.24; at 01 MLT from 0.08 to 0.53; at 02 MLT from 0.10 to 0.44. Other than near midnight, however, the fit was not significantly improved by a higher order polynomial. Thus, for a fifth order polynomial versus a linear fit with the variable Kp, the correlation coefficient increases from 0.46 to 0.52 at 06 MLT; from 0.76 to 0.79 at 09 MLT; from 0.78 to 0.84 at 12 MLT; from 0.79 to 0.85 at 15 MLT; and from 0.55 to 0.58 at 18 MLT.

No matter what fit is made, however, the fact is that the measured ion poleward boundary location has a great deal of variation at each MLT. Although a higher order polynomial with its greater number of free parameters provides an improved fit, reflected in a somewhat larger correlation coefficient, the basic variability of the data cannot be masked. Also, the trend of the linear fit at each MLT, particularly the slope, is manifest in all of the more elaborate fits as well.

AE. A similar linear analysis of the data was made in terms of AE. The results of the linear regression analysis for the latitude of the ion poleward boundary and AE are shown in Table 6, and examples of the fit at selected MLT are shown in Figure 4. The left-hand panel of Figure 4A is a plot of all the measured ion poleward boundaries between 23-24 MLT vs AE. The solid line is the linear regression fit of the boundaries with AE; the equation for the fit is shown in the figure along with the correlation coefficient. Figure 4A also shows the average ion poleward boundary and the standard deviation for each AE bin. The dashed line is the least squares fit to the averages binned by AE. Figure 4B is in the same format as Figure 4A, but for the ion poleward boundaries measured between 08-09 MLT. Similar fits have been calculated for each one-hour MLT bin.

Similar qualitative features are found for the AE results as stated above for Kp. For example, the latitude of the average ion poleward boundary undergoes little change within about 3 hours of local midnight as AE changes. Figure 4 and Table 6 suggest that AE provides a slightly improved ordering of the data than Kp (or the other magnetic parameters).

IMF Bz. Variations in the latitude of the ion poleward boundaries with changes in IMF Bz were also examined. The IMF Bz data base D(IMF) contains 1466 ion poleward boundaries. Linear fits to the ion poleward boundaries are shown in Figure 5 at two chosen times, 22-23 MLT and 10-11 MLT. (In Figure 5, IMF Bz is plotted so that an increase in abscissa corresponds to greater activity. Thus, the plots may be compared directly with the Kp and AE plots.) The solid line is the linear regression fit of the ion boundary with IMF Bz. The equation for the fit is shown in the figure along with the correlation coefficient. The dashed line is the linear fit to the average
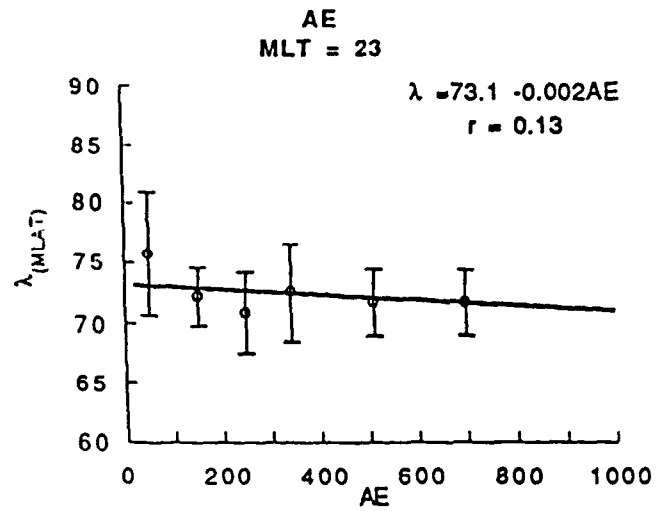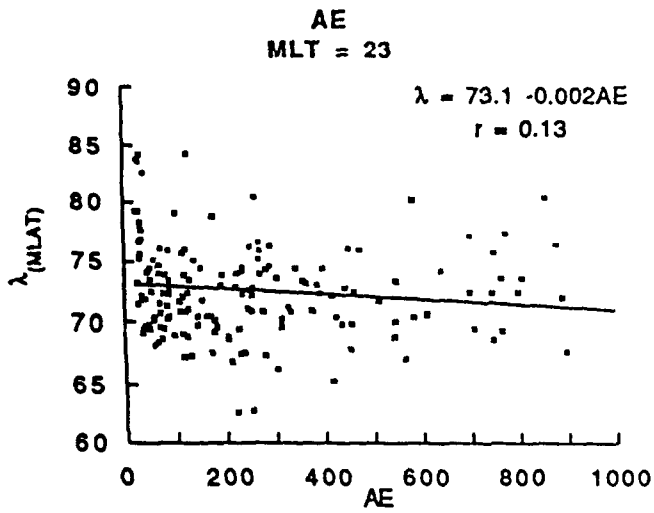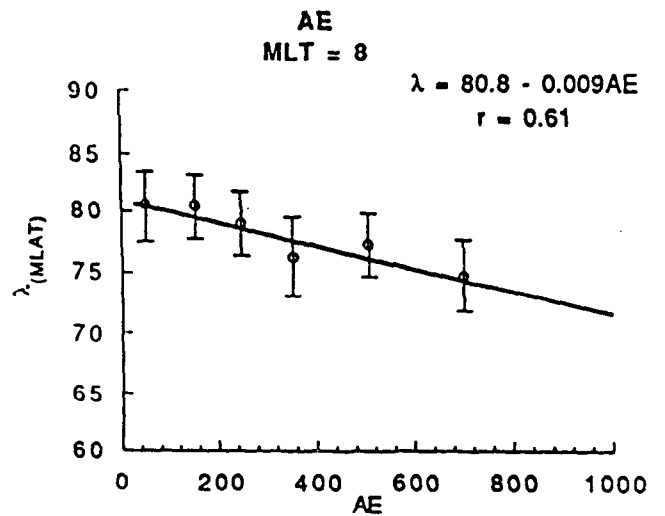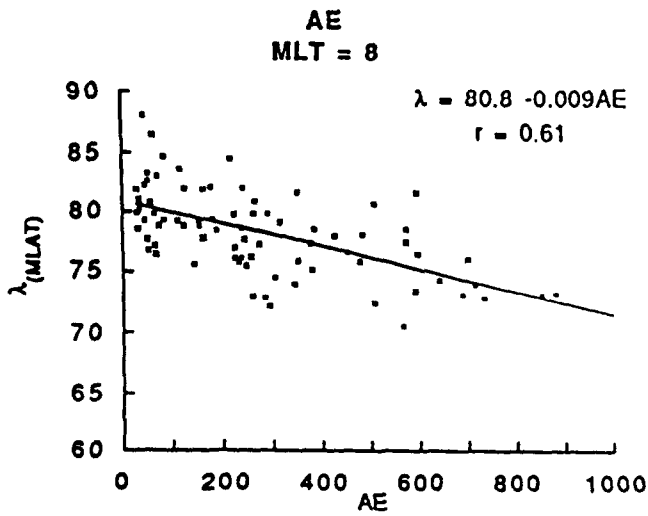
Figure 4. Plots in AE in the same format as Figure 3:   A. By AE bin for the 2300-2400 MLT sector. B. The same as A, but for the 0800-0900 MLT sector.
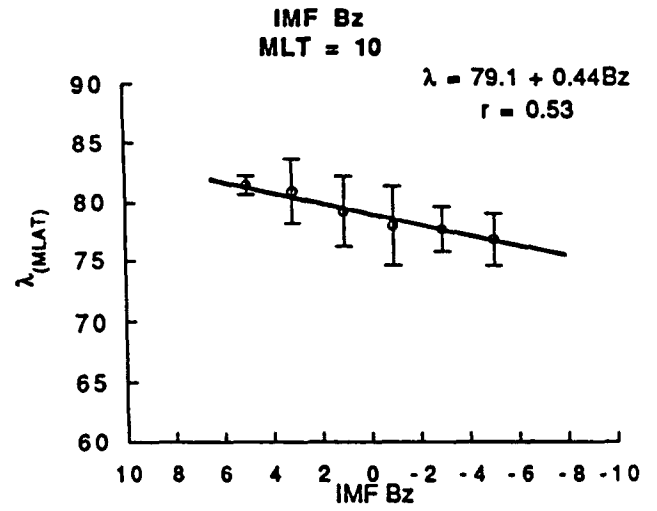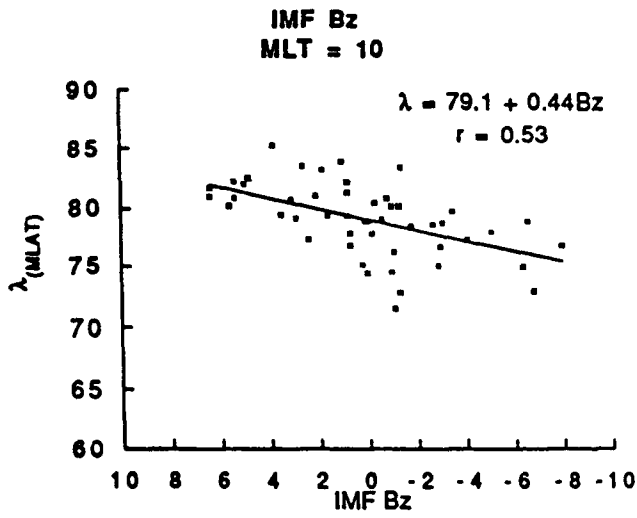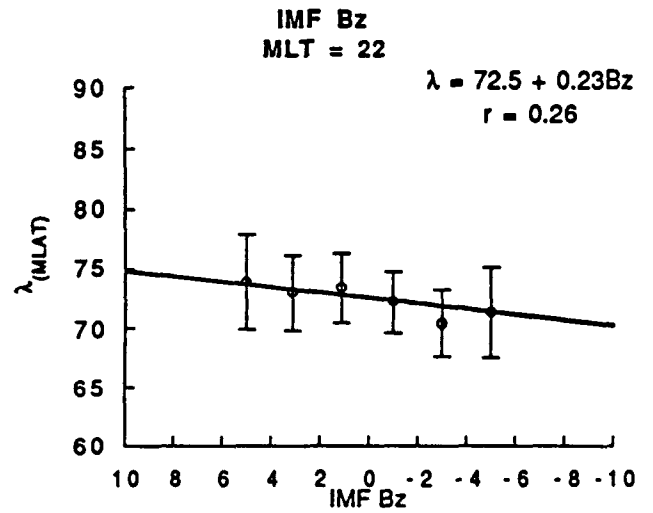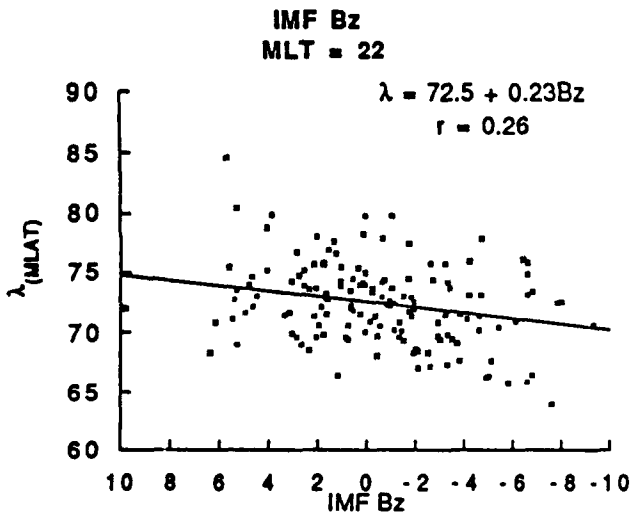
Figure 5. In the same format as Figure 3: A. For each IMF Bz bin for the 1000-11:00 MLT sector. B The same as A, but for the 2200-2300 MLT sector.

ion poleward boundary for each IMF Bz bin; the error bars indicate one standard deviation from the average ion poleward boundary for each IMF Bz bin. Similar results have been calculated for each of the one-hour MLT bins. The coefficients from equation (1) relating the latitude of the ion poleward boundary and IMF Bz are shown in Table 7.

Table 6. AE Linear Regression Ion Boundary Parameters.

MLT	#	a	100b	r(λ, $\hat{\lambda}$)
00-01	90	73.3	-0.229*	-0.13
01-02	98	74.9	-0.213*	-0.14
02-03	90	76.0	-0.380	-0.23
03-04	109	78.2	-0.761	-0.47
04-05	144	77.4	-0.433	-0.27
05-06	127	79.8	-0.908	-0.55
06-07	136	80.1	-0.851	-0.55
07-08	71	79.8	-0.754	-0.56
08-09	81	80.7	-0.893	-0.60
09-10	78	80.7	-0.909	-0.74
10-11	88	81.1	-0.732	-0.77
11-12	19	82.5	-0.824	-0.58
12-13	16	81.3	-0.733	-0.72
13-14	35	81.1	-0.907	-0.68
14-15	18	82.2	-1.49	-0.78
15-16	18	81.3	-1.72	-0.83
16-17	49	79.1	-1.17	-0.76
17-18	78	79.2	-1.10	-0.61
18-19	120	77.6	-0.924	-0.53
19-20	155	77.8	-0.919	-0.61
20-21	132	76.2	-0.963	-0.58
21-22	159	74.0	-0.333	-0.22
22-23	247	72.8	-0.177	-0.14
23-00	161	73.2	-0.209*	-0.13

Table 6. Linear regression results, ion boundary latitude versus AE. Column headings are in the same format as Table 4 except that the regression coefficient b is multiplied by 100.

As with the Kp and AE results, in the IMF Bz linear regression analysis the nightside correlations are poor compared to the dayside ones, and there is also more scatter in the nightside boundaries. Also, with IMF Bz, the correlation coefficient between the observed and predicted latitudes r(λ, $\hat{\lambda}$) is almost always small and usually less at most MLTs than found for the Kp and AE analyses.

Table 7. IMF Bz Linear Regression Ion Boundary Parameters

MLT	#	a	b	$r(\lambda, \hat{\lambda})$
00-01	62	72.5	0.24*	0.23
01-02	71	74.0	0.21	0.25
02-03	59	74.2	0.16*	0.19
03-04	67	76.4	0.45	0.45
04-05	99	76.2	0.28	0.31
05-06	78	77.8	0.65	0.53
06-07	78	78.1	0.26	0.27
07-08	48	78.3	0.56	0.47
08-09	48	77.9	0.50	0.40
09-10	45	78.0	0.59	0.48
10-11	50	79.1	0.44	0.53
11-12	12	79.8	0.42*	0.45
12-13	9	79.2	0.72	0.81
13-14	22	77.6	0.45*	0.38
14-15	15	77.8	0.64*	0.41
15-16	15	76.6	0.74	0.61
16-17	29	74.1	0.44*	0.32
17-18	52	76.4	0.43	0.34
18-19	68	75.0	0.52	0.37
19-20	99	74.9	0.44	0.36
20-21	79	73.5	0.68	0.45
21-22	112	73.0	0.27	0.28
22-23	149	72.5	0.23	0.26
23-00	100	72.7	0.17*	0.18

Table 7. Linear regression results, ion boundary latitude versus IMF Bz. Column headings are in the same format as Table 4.

One interesting feature of the IMF Bz analysis is that the smallest polar cap (corresponding to largest latitudes) does not occur for IMF Bz = 0. The subset of the data base D(IMF) with IMF Bz > + 4 gave essentially the smallest polar cap, and one that is approximately equal to the polar cap size for AE = 0 or Kp = 0 in the latter two analyses.

In an attempt to discover special effects, other more refined sortings of the ion poleward boundary data base were made, including the following: 1) the AE measurements near midnight were separated according to the sign of the slope of AE, a positive slope corresponding roughly to the substorm growth phase and a negative slope roughly to the substorm recovery phase; 2) the IMF Bz data base was divided between high Kp and low Kp values; 3) the IMF data base was sorted by the sign of IMF By. A problem with such progressively refined groupings is that the data base becomes segmented to the point where confidence in the results may be eroded.

In the case where the AE ≥ 200 nT data base was divided into positive and negative slopes near midnight, no systematic dependence on the slope was found. The results by AE slope for the MLT range 22-03 in one hour bins are shown in Table 8.

TABLE 8. Nightside ion boundary according to AE slope.

MLT	slope	#cases	mean MLAT	σ
21-03	+	153		
21-22	+	29	71.4	3.3
22-23	+	53	70.8	3.4
23-24	+	26	72.6	3.6
00-01	+	16	71.6	4.6
01-02	+	14	73.8	3.8
02-03	+	15	74.6	4.0
21-03	-	147		
21-22	-	29	72.3	2.8
22-23	-	36	72.4	3.8
23-24	-	30	72.3	4.1
00-01	-	17	73.2	2.7
01-02	-	19	74.2	2.4
02-03	-	16	73.6	2.4

Table 8 gives the mean and standard deviation of the ion poleward boundaries in six one-hour MLT bins near midnight separated according to whether AE was increasing or decreasing at the time of measurement.

From Table 8, the mean boundary location for the negative slope AE cases has a slight tendency to be a bit higher than for the positive slope cases. Such a trend would be in the right direction to correspond with a popular view of substorm dynamics where the polar cap enlarges to lower latitudes during the growth phase (positive slope), and contracts toward the pole during the expansion phase (negative slope). In the complete 6 hour MLT range of Table 8, the main characteristic is the very large scatter in the data. The means for both positive or negative AE-slope fall well inside of the large standard deviations for each one-hour MLT bin.

It was disappointing to find that IMF Bz does not organize the ion poleward boundary set very well, as is seen in the small correlation coefficients in Table 7. In an effort to improve the Bz results, a test was made to determine whether IMF Bz would have a different affect on the location of the ion poleward boundary depending on its initial latitude. To examine this possibility, we

23

divided the IMF Bz data base into low (< 3-) Kp and high (≥ 3-) Kp groups. When the boundaries are binned by IMF Bz and larger than one-hour MLT bins used, the average ion poleward boundaries in the low Kp group are at higher latitudes than those in the high Kp group by a few degrees, although the trend is doubtful near midnight. Perhaps a larger data set that could accommodate finer resolutions in IMF Bz, MLT, and Kp would be more definitive than the results obtained here. An interesting test might be to determine the latitude change, $\Delta\lambda$, of the ion poleward boundary produced by changes in IMF Bz.

The effect of IMF By on the ion poleward boundary would be expected to be most pronounced on the dayside. Unfortunately, our data set is probably not suitable to evaluate an IMF By effect for the following reasons. Only a small number of boundaries are measured in the IMF data base for dayside MLTs between 0800 and 1600 MLT, because many of the dayside boundaries are measured in the southern hemisphere where the satellite is equatorward of the auroral zone for a good part of the day. Also, to evaluate IMF By effects, the north and south pole boundary measurements must be separated. In our data set, the only MLT on the dayside that has enough measurements to evaluate is 10 MLT. For this MLT, the straight line fit of the positive IMF By boundaries is about 1° higher in latitude than the straight line fit of the negative IMF By boundaries over the Kp range from 0 to 6.

E. Empirical Closed Curve Representations

The surprisingly good agreement between the linear fits to the average ion poleward boundaries and the linear regression results with each of the magnetic activity parameters (Figures 3-5, right panels) suggested that a well-ordered statistical representation of the average instantaneous ion poleward boundary, continuous in MLT for each value of Kp (or AE or IMF Bz), could be constructed from our data base. This was done as follows. The size of the data base enabled us to sort the measured ion poleward boundaries into reasonable bins for each of the magnetic parameters: Kp, AE and IMF Bz. The boundary measurements in each parameter bin were then averaged and the standard deviation obtained for each hour MLT. A "cutoff" of nine

boundary data points was arbitrarily designated as the minimum acceptable number of boundaries needed to calculate a meaningful average within a bin. This "cutoff" applies to all parameter bin analysis unless otherwise specified. In general the MLT bins, counterclockwise from 18 to 10 MLT, inclusive, have a sufficient number of data points, while the MLT bins from 11 to 17 MLT, inclusive, are deficient. There are exceptions, however, which tend to occur at the extremes of the Kp (AE or IMF Bz) range. For example, Kp0 contains the smallest number of cases and has only 3 bins with 9 or more boundary points. Also, in the smaller IMF data set D(IMF), there are more bins with insufficient data. The deficient MLT bins are mostly on the dayside between 11 and 17 MLT (as was the case with the larger Kp and AE data base) and in the IMF Bz +4 or -4 parameter bins.

The ion poleward boundaries were sorted into six Kp bins consisting of a whole level of Kp (e.g., the bin denoted Kp1 contains measurements for Kp = 1-, 1, 1+) through Kp = 4. Boundaries measured for Kp ≥ 5- are included in the highest bin. The ion poleward boundaries were sorted into AE bins in the following manner:

AE Bin	Included values (AE)
50	≤ 50 nT
100	51 to 149 nT
200	150 to 249 nT
300	250 to 349 nT
450	350 to 549 nT
600	≥550 nT

The boundaries were sorted into six IMF bins in order to be able to calculate suitable averages for each hour in MLT. The IMF Bz bins are as follows:

IMF Bz Bin	Included values (IMF Bz)
+4	≥ +4.0 nT
+2	+2.0 to +3.9 nT
+0	+0.0 to +1.9 nT
-0	-0.0 to -1.9 nT
-2	-2.0 to -3.9 nT
-4	≤ -4.0 nT

The six cases with IMF Bz = 0.0 nT were divided evenly, at random, between the +0 and -0 IMF Bz bins.

Figures 6, 7 and 8 are composite plots of the ion poleward boundaries averaged in MLT for the Kp, AE and IMF Bz parameter bins, respectively. The panels in each figure are organized so that the lowest level of activity is in the top left panel. Each panel contains the results for the parameter bin that is labelled at the top of the panel. Each plot is in polar coordinates: MLT with noon at the top and dawn on the right; and MLAT with each dashed circle representing an increment of 10° MLAT. For each magnetic parameter level, we show the averaged ion poleward boundary for a given hour MLT bin with an open circle, o. The average boundaries are simply connected; there is no fitting in these plots. The error bars are the standard deviation of the average boundary at each MLT. Where there is no error bar, fewer than 9 boundaries make up the average for that particular MLT bin.

Some immediate conclusions can be made from Figures 6, 7 and 8 about the average ion poleward boundary:

1. The area enclosed by the average ion poleward boundary increases with increasing magnetic activity, no matter which activity parameter is used.

2. The average ion poleward boundary never goes below 70° MLAT (although individual boundaries may, as the error bars show).

3. The average ion poleward boundary moves about 5° equatorward in latitude on the dayside as activity increases, the movement coming primarily when higher levels of activity are reached (about Kp = 4, or AE = 450, or IMF Bz = -2).
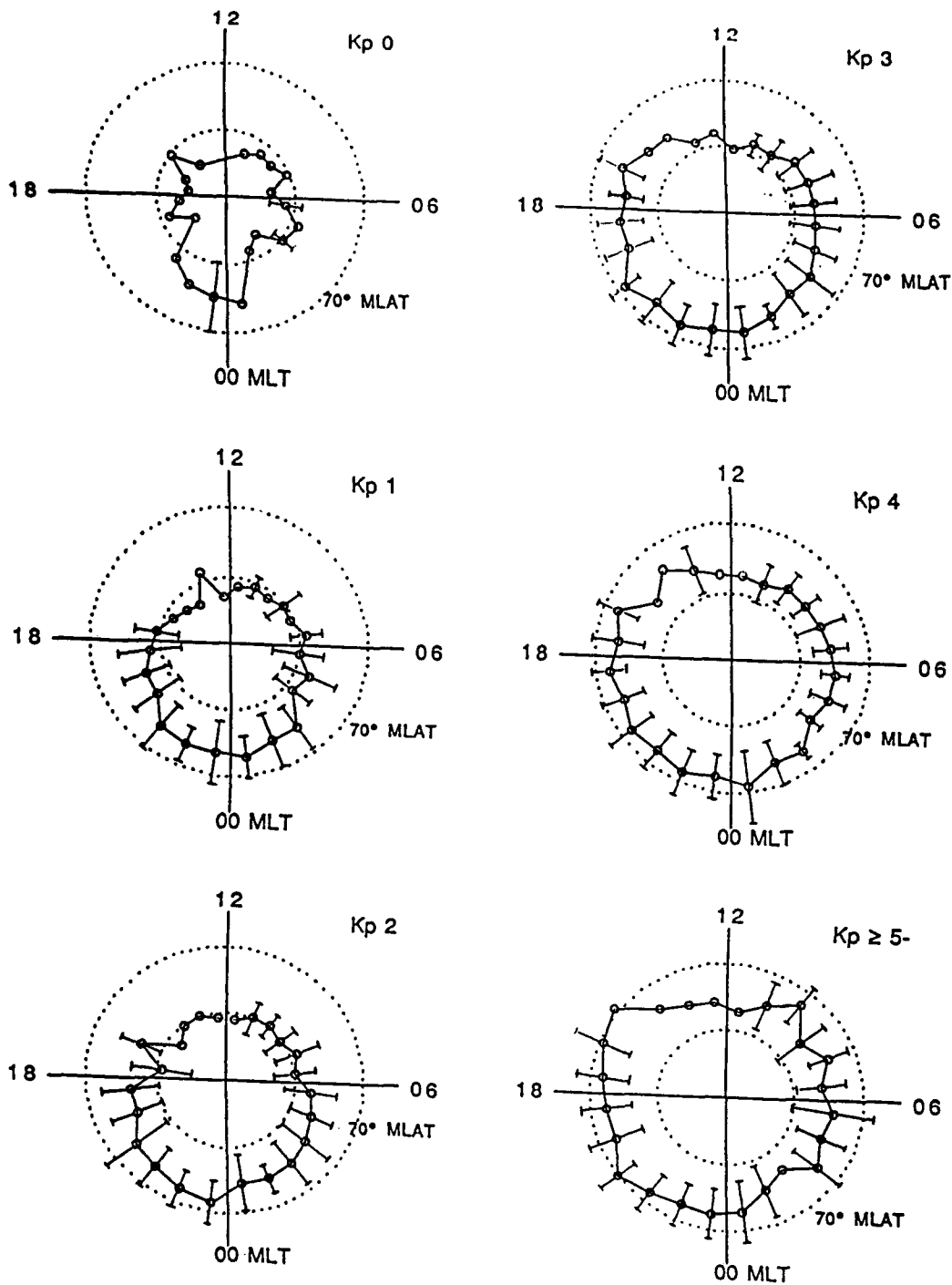
Figure 6. Kp variation of average ion poleward boundary. Polar plots in MLT and MLAT are shown for six designated Kp bins. Each panel specifies the Kp sector and shows the latitude of the average ion poleward boundary (circles) for each one hour MLT bin. The dotted circles are at 10 degree increments from the pole. The error bars denote one standard deviation from the average in each MLT bin. When no error bar is shown, the average consists of fewer than 9 boundary measurements. The average boundaries in successive MLT bins are simply connected by straight lines.
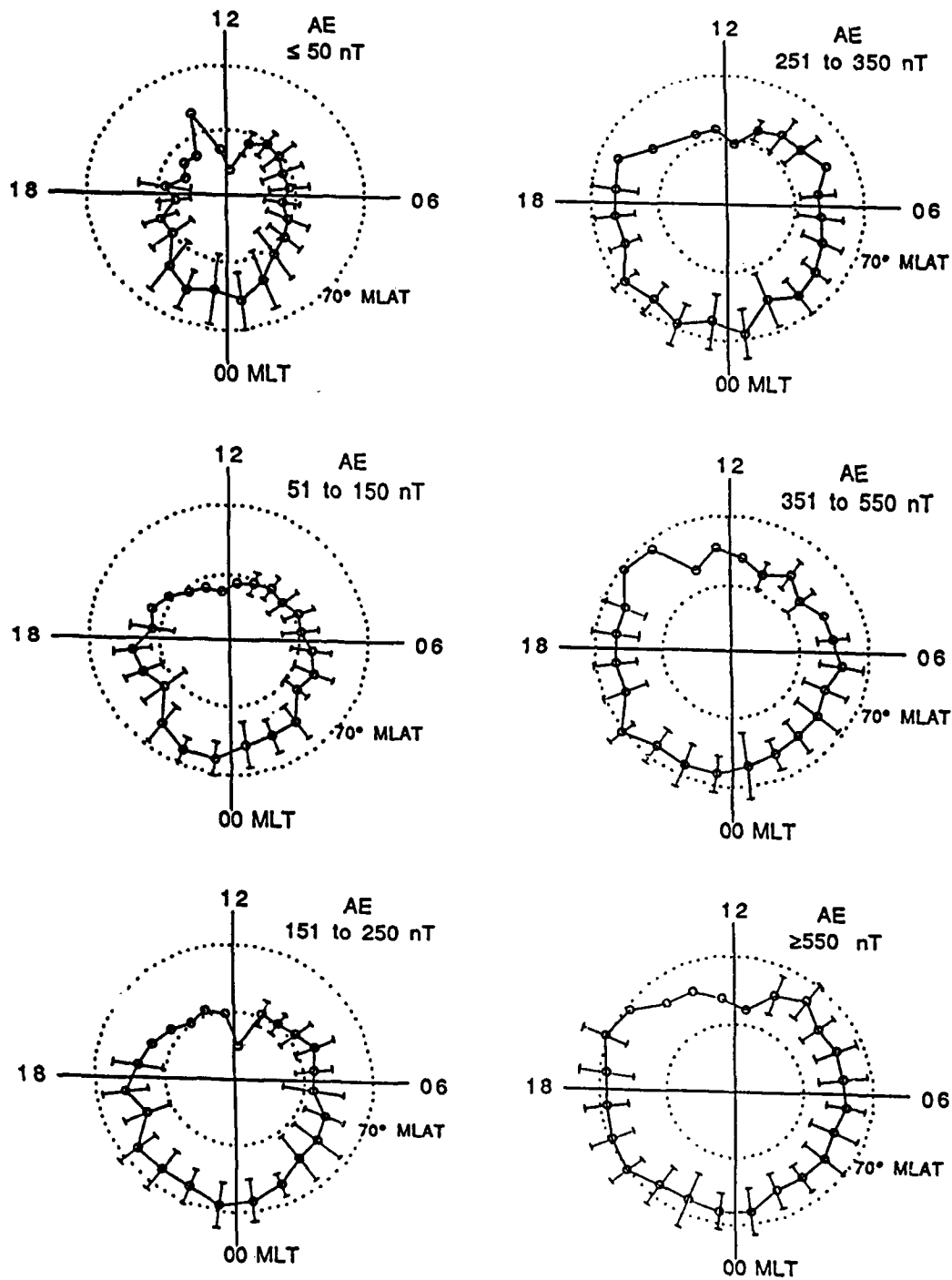
Figure 7. AE variation of the average ion poleward boundary in the same format as Figure 6.
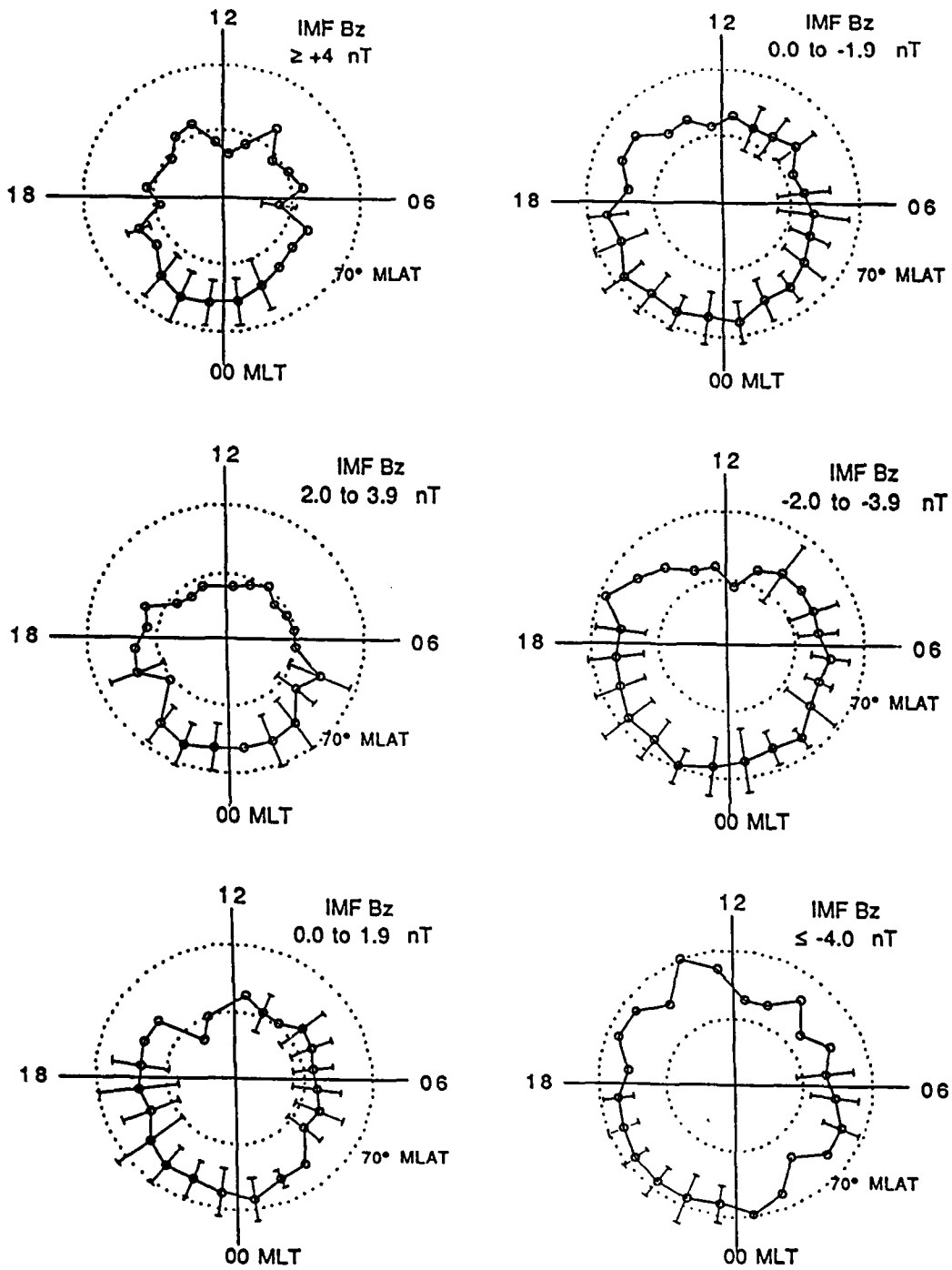
Figure 8. IMF Bz variation of the average ion poleward boundary in the same format as Figures 6 and 7.

4. The average ion poleward boundary moves about 5° equatorward in latitude on the nightside as activity increases to Kp = 2, after which there is essentially no further movement of the average ion poleward boundary to lower latitudes.

5. The average ion poleward boundary moves somewhat more than 5° equatorward in latitude near dawn and dusk, with a more regular trend with increasing activity.

6. The center of the closed empirical boundary is located in the premidnight quadrant, corresponding to a net displacement from the geomagnetic pole towards midnight and dusk.

F. Functional Fits to the Polar Cap Boundary

For each Kp bin, the best fourth order fit was obtained to the measured ion poleward boundaries as a function of MLT. The best fit curves by Kp bin are shown in Figure 9. For each Kp bin, the fourth order fits also accurately match the average ion poleward boundary location in MLT. This is demonstrated in Figure 10, top panel for the Kp2 and bottom panel for the Kp4 bin. In Figure 10, the fourth order fit, the average boundary location and its standard deviation for each MLT, and correlation coefficients are shown. The fourth order fit provides an accurate statistical representation of the average ion boundary.

The fourth order fits in Figure 9 exhibit a simple variation in MLT that may be represented by analytical functions for the boundary curves. Two such analytical representations of the boundary were constructed corresponding to a circle and a simple harmonic function.

Representation as a circle. A circle on a sphere may be defined in terms of the spherical coordinates of the radius that passes through the center of the circle and the half-angle subtended by the circle with respect to the center of the sphere. These are denoted (R, θ, ϕ_M) and Φ, respectively. Here R is the radius of the sphere, θ and ϕ_M are the co-latitude and azimuth, respectively, of the center of the circle, and Φ is the half-angle. The radius of the circle is

$$a = R \sin \Phi \qquad\qquad (2)$$

and the equation for the circle is

30
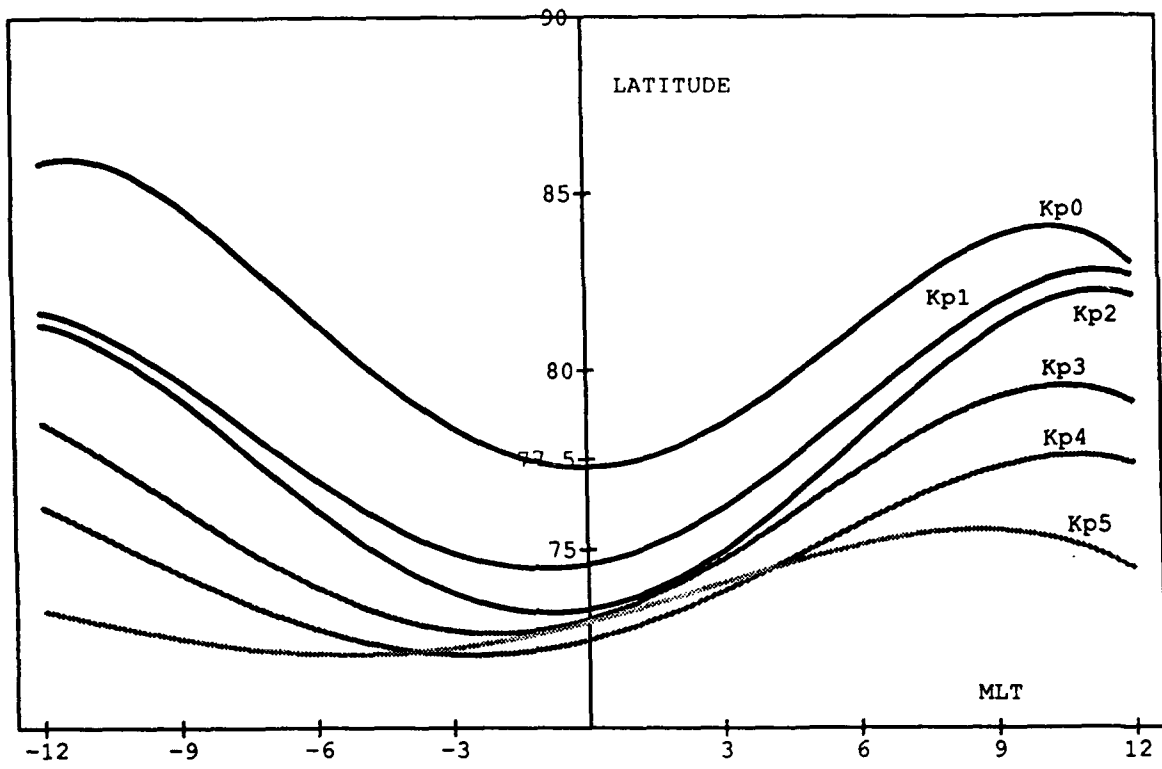
Figure 9. Fourth order fits for the ion boundary binned by Kp versus MLT. All boundaries in the full data set D(all) are used. Zero MLT is midnight and negative MLT is the PM sector.
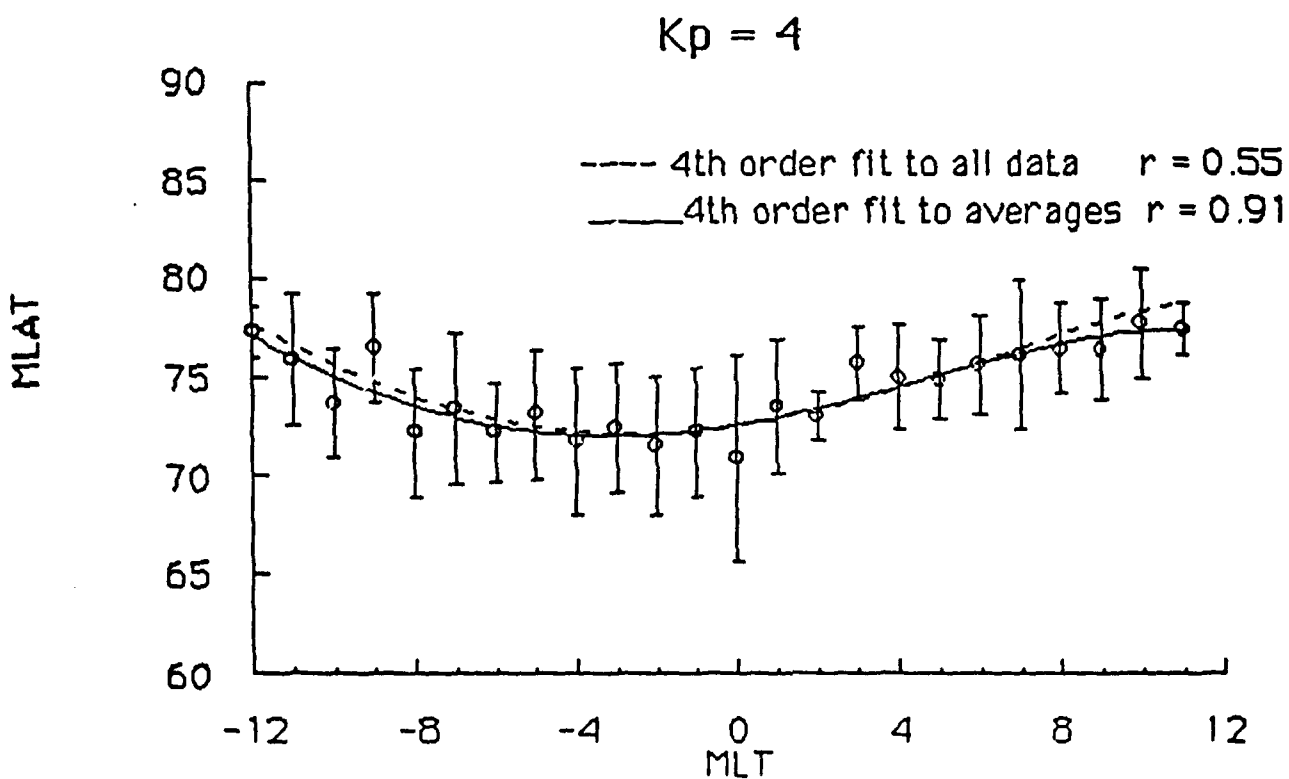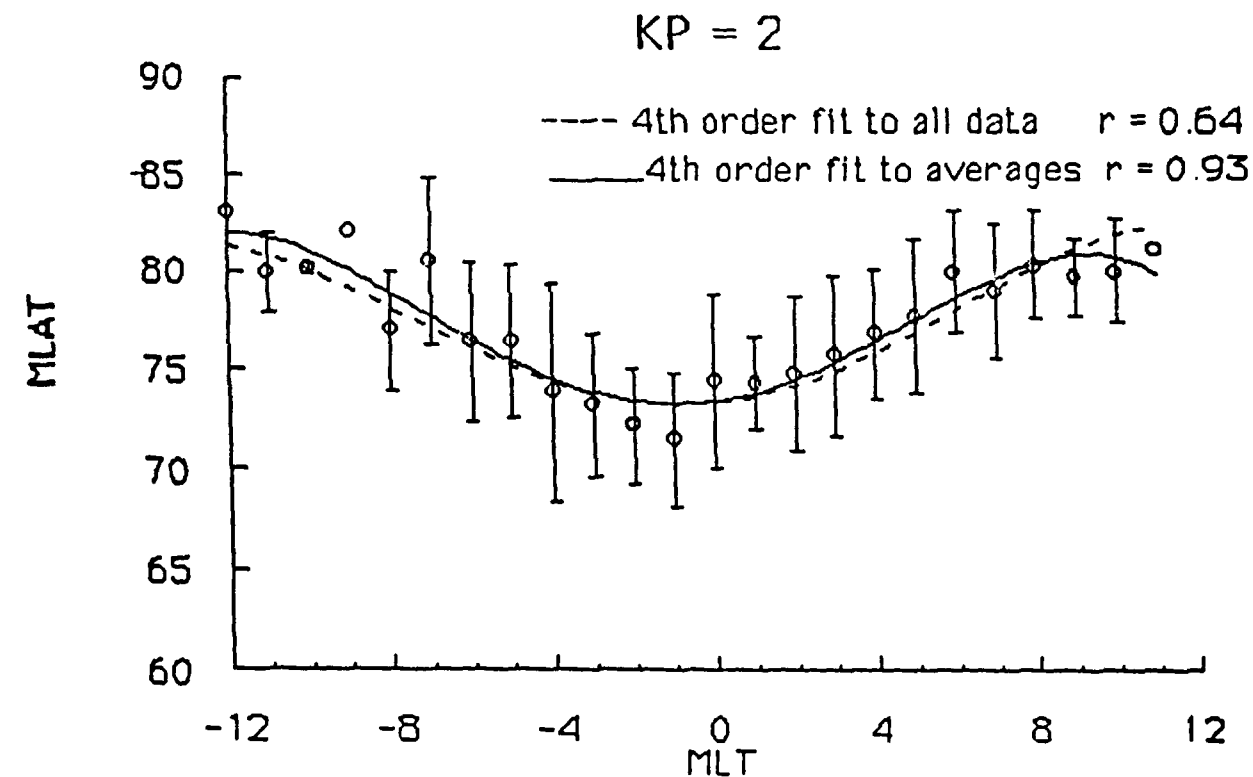
Figure 10. Comparison of fourth order fits in MLT for selected Kp bins. From Figure 9, the fourth order fits (dashed curves) for the Kp2 and Kp4 bins are repeated in the upper and lower panels, respectively. The average boundaries and standard deviations shown in Figure 6 are also plotted; the solid curve in each panel is the fourth order fit to the averages. The correlation coefficients (r) when all the boundary measurements (top) and when the average ion poleward boundary for each one-hour MLT bin (bottom) are fit to a fourth order curve are given at the top right of each panel.

$$\cos(\phi - \phi_M) = \frac{\cos\Phi - \cos\theta\cos\vartheta}{\sin\theta\sin\vartheta} \qquad (3)$$

Here, ϑ is the magnetic co-latitude and ϕ the azimuth (i.e., magnetic longitude or MLT) for points on the circle. At $\phi = \phi_M$ the maximum or most equatorward co-latitude ϑ_M occurs (where $\vartheta_M = \Phi + \theta$).

Circular fit by Kp. The fit of a circle to the fourth order curves is done as follows. As seen from Figure 6, for each Kp there are MLTs on the dayside with no standard deviation shown for points with only a small number of measurements. Such points and MLTs are excluded from the analysis of the circle fit. For the other MLTs an optimal fit is derived for the circle fit to the value of the fourth order curve. The results of this analytical procedure are given in Table 9.

Table 9. Circular representation of the ion polar boundary.

Kp	Φ	θ	ϕ_M degrees (MLT)
0	9.5	3.21	-1.30 (23:55)
1	12.2	3.73	-14.95 (23:00)
2	13.1	4.12	-12.94 (23:08)
3	14.4	3.25	-31.54 (21:54)
4	15.7	2.52	-38.99 (21:24)
5	16.5	1.67	-79.02 (18:44)

In the table, the circle is defined by the angles Φ, θ and ϕ_M for each Kp bin.

The quality of the circle fit to the fourth order curve is usually within about 0.2-0.3 degrees on the nightside and afternoon sector where the data is best, with somewhat larger deviations at the poor data points (where the fourth order curve itself is of little significance). A polar plot of the circle and the fourth order curve is shown in Figure 11 with the cases Kp=2 and Kp=5 superposed in the upper diagram and the cases Kp = 1 and Kp = 4 superposed in the lower diagram. The good quality of the fit is evident. Figure 11 also shows graphically how most of the increase in size of the polar cap with increase in Kp comes from the dayside expansion of the polar cap.

Least square fits for the variation of the angles in Table 9 with Kp are given by:

$$\Phi \, (Kp) = 10.02 + 1.358 \, Kp$$

$$\theta \, (Kp) = 3.280 + 0.6637 \, Kp - 0.2025 \, Kp^2$$

$$\phi_M \, (Kp) = 4.450 - 13.70 \, Kp$$

The linear fit for θ gives a poor representation of actual values, and the linear fit for ϕ_M is also rather poor. Thus a simple dependence of the center of the circle on Kp does not pertain.

The magnetic flux of a dipole field through a closed curve $\theta(\phi)$ on a sphere of radius R is

$$F = \frac{2M}{R} \int_0^\pi d\phi \, \sin^2 \theta(\phi) \tag{4}$$

Here the curve $\theta(\phi)$ is taken to have an axis of symmetry and ϕ is measured with respect to that axis. For the earth's dipole moment and $R = R_E + 110$ km,

$$\frac{2M}{R} = 24.23 \times 10^{16} \, \text{gauss cm}^2 \tag{5}$$

In units of 10^{16} gauss - cm^2, the magnetic flux of the fitted circles by Kp bin are given in Table 10. The least squares fit to the flux is

$$F = (2.324 + 0.787 \, Kp) \times 10^{16} \, \text{gauss - cm}^2 \tag{6}$$

The area on a sphere intercepted by a circle on the sphere of angle Φ is

$$A = 2\pi \, R^2 \, (1 - \cos \Phi)$$

which approximates closely the area of the circle itself (i.e., $\pi R^2 \sin^2 \Phi$). In units of 10^{16} cm^2, the polar cap area by Kp bin is given in Table 10. With less than 1% error, the ratio of polar flux to polar cap area is constant:

$$F/A \approx 0.567 \, \text{gauss} \tag{7}$$

The value 0.567 gauss is essentially the polar magnitude of the dipole field intensity at 110 km.
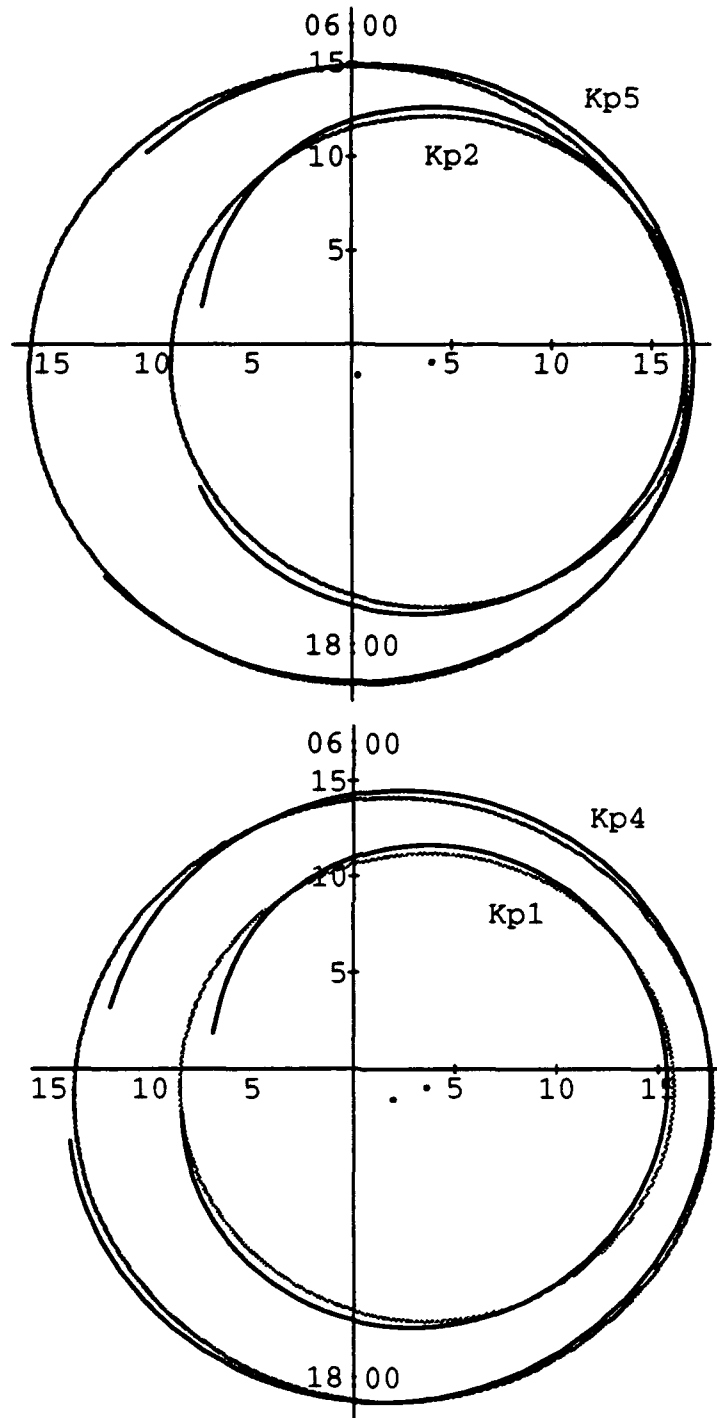
Figure 11. Comparison of the circle and fourth order fits to the average poleward ion boundary. The cases Kp2 and Kp5 are shown in the upper diagram, and Kp1 and Kp4 in the lower diagram. In the figure, the sun is at the left and dawn at the top. The two points in each diagram denote the centers of the circles. The axes tick marks give the latitude in degrees.

35

Table 10. Flux and area of polar cap circles by Kp bin

Kp	0	1	2	3	4	5
F	2.09	3.37	3.88	4.73	5.58	6.11
A	3.66	5.93	6.85	8.36	9.89	10.83

The flux F and area A of the polar cap circular fits are given by Kp bin. F is in units of 10^{16} gauss-cm^2 and A in units of $10^{16} \, cm^2$.

Other features of the polar cap boundary circle are the values of the most equatorward co-latitude (θ_{max}), most poleward latitude (θ_{min}), the co-latitude at noon (θ_{12}), and the midnight co-latitude (θ_{00}). These angles in degrees are given in Table 11 for each Kp bin.

Table 11. Characteristics of the Kp circular fit.

Kp	θ_{max}	θ_{min}	θ_{12}	θ_{00}
0	12.75	6.34	6.34	12.75
1	15.89	8.42	8.51	15.72
2	17.19	8.95	9.02	17.05
3	17.69	11.19	11.58	17.12
4	18.23	13.19	13.68	17.59
5	18.12	14.79	16.06	16.69

The polar angle of the most equatorial boundary (θ_{max}), most polar boundary (θ_{min}), noon boundary location (θ_{12}), and midnight boundary (θ_{00}) of the circle.

Least square functional fits for the angles in degrees are given by:

$\theta_{max} = 13.04 + 2.70 \, Kp - 0.34 \, Kp^2$

$\theta_{00} = 12.99 + 2.76 \, Kp - 0.41 \, Kp^2$

$\theta_{min} = 6.28 + 1.68 \, Kp$

$\theta_{12} = 6.10 + 1.90 \, Kp$

Because the fit to the average ion boundary location is a circle whose center is off-set from the magnetic pole, the maximum co-latitude is not quite coincident with the midnight co-latitude of the circle; and the minimum co-latitude is not quite coincident with the noon co-latitude. The angle θ_{max} always falls in the pre-midnight quadrant and θ_{min} in the pre-noon quadrant. Electron precipitation data suggests that the cusp occurs at θ_{min}, which is where the minimum in electron average precipitation energy occurs. The electron and ion boundary locations give similar but not identical values for θ_{min}. Variation of cusp location with Kp is slightly greater in the ion boundaries.

Estimates for the polar cap area from electron precipitation data are 8.6 (Kp 0 to 2) and 10.9 (Kp 3 to 5). These are somewhat larger values than found for the ions (see Table 10). The ion data shows a more systematic trend in polar cap area and perhaps is based upon a more detailed analysis than made for the electrons.

Circular fit by AE. A similar analysis of the ion precipitation boundary was made by AE. As with the Kp analysis, fourth order fits to the data were made in MLT for each AE bin. Optimal fits of a circle to the fourth order curves were determined analytically for each AE bin. The results for the derived circles are shown in Table 12.

Table 12. Characteristics of the AE circular fit.

AE	Φ	θ	ϕM	F	A
AE0(25)	10.2	3.07	-9.36	2.41	4.22
AE1(100)	12.6	4.15	-13.3	3.61	6.36
AE2(200)	13.8	3.9	-23.0	4.35	7.68
AE3(300)	15.3	2.94	-27.2	5.26	9.32
AE4(450)	15.9	2.36	-44.1	5.70	10.10
AE5(650)	17.2	1.75	-81.9	6.65	11.82

By AE bin are given the angles of the circle in degrees, the magnetic flux in 10^{16} maxwells intercepted by the circle, and the area of the circle in 10^{16} cm^2.

In order to derive functional fits to the parameters, a value of AE is assigned to each AE bin. The assigned value of AE to the bin is shown in parentheses in the first column of Table 12. Using these values for AE, least square functional fits are given by:

$$\Phi = 11.25 + 1.02 \ (AE/100)$$

$$\theta = 4.58 - 0.459 \ (AE/100) \ (for \ AE > 100)$$

$$\phi_M = -0.899 - 11.21 \ (AE/100)$$

$$F = 2.84 + 0.636 \ (AE/100)$$

$$A = 4.88 + 1.16 \ (AE/100)$$

Special angles of the circle (minimum, maximum, noon, and midnight co-latitudes) were derived and gave the following functional fits:

$$\theta_{max} = 16.2 + 0.788 \ (AE/100) - 0.0582 \ (AE/100)^2$$

$$\theta_{00} = 15.9 + 0.847 \ (AE/100) - 0.0991 \ (AE/100)^2$$

$$\theta_{min} = 7.15 + 1.37 \ (AE/100)$$

$$\theta_{12} = 6.95 + 1.59 \ (AE/100)$$

In these expressions, the values AE = 25, 100, 200, 300, 450, and 650 nT are used.

Polar cap flux, merging, and convection parameters. From the analytical circular fits to the polar cap boundary, and the changes in boundary location with magnetic activity, certain heuristic magnetospheric parameters can be determined. These include a geomagnetic tail flux parameter (f), a magnetic merging parameter (m), and a boundary convection parameter (Ceq). The three parameters are defined and evaluated in terms of the circular fits to the boundary as follows.

The magnetic flux in the magnetospheric tail (say, the northern lobe) may be represented by the formula:

$$F_{tail} = (\pi R_T^2/2) B_T \qquad (8)$$

where R_T is the radius of the tail and B_T is the magnetic intensity. For $R_T = 15$ R_E and $B_T = 25$ nT, the tail flux is

$$F_{to} = 3.594 \times 10^{16} \text{ maxwells} \qquad (9)$$

Thus we define

$$F_{tail} = f\ F_{to} \qquad (10)$$

where f is the tail flux parameter given by

$$f = \left(\frac{R_T}{15}\right)^2 \left(\frac{B_T}{25}\right) \qquad (11)$$

If we equate the tail flux to the polar cap flux, then the dependence of the latter on Kp (or AE) gives a relationship for the value of the tail flux as a function of magnetic activity. For Kp we obtain using equations 6 and 10:

$$F_{tail} = F_{pc} = (2.324 + 0.787\ Kp) \times 10^{16} \text{ maxwells}$$

$$f = 0.647 + 0.219\ Kp \qquad (12)$$

As an example, suppose for Kp = 0 that the field intensity in the tail is $B_T = 10$ nT. The tail flux parameter (equations 11 and 12) then determines the tail radius to be $R_T = 19R_E$. Similarly, if $B_T = 30$ nT and Kp = 5, then the tail radius is $R_T = 18R_E$.

Using AE as the activity parameter,

$$F_{tail} = F_{pc} = [\ 2.836 + 0.636\ (AE/100)\ ] \times 10^{16} \text{ maxwells} \qquad (13)$$

$$f = 0.789 + 0.177\ (AE/100) \qquad (14)$$

As examples, if AE = 25 and $B_T = 10$ nT, then $R_T = 21.6\ R_E$; if AE = 500 and $B_T = 30$nT, then $R_T = 17.7\ R_E$

A magnetic merging parameter may also be introduced relating to changes in polar cap flux. Thus, suppose the result of reconnection is to produce a change in magnetic flux which we represent heuristically by

$$F_m = B_{sw} \, L \, v_{sw} \, T \, r \text{ maxwells} \tag{15}$$

Here B_{sw} is the merging component of the IMF that acts over the spatial scale L for the time T. The IMF is convected at the solar wind speed v_{sw}, and r is the fraction of the IMF that merges. To set the scale of the merging, let

$$F_o = (5nT) \, (10R_E) \, (450 \text{ km/sec}) \, (3600 \text{sec}) \, (1/10)$$

$$= 0.517 \times 10^{16} \text{ maxwells}$$

For any other set of parameter values, we write (15) as

$$F_m = m \, F_o \tag{16}$$

Here m is the "merging parameter" given by

$$m = \left(\frac{IMF}{5nT}\right) \left(\frac{L}{10R_E}\right) \left(\frac{v_{sw}}{450}\right) \left(\frac{T}{3600}\right) \frac{r}{(1/10)} \tag{17}$$

A simple dependence of the merging parameter m on magnetic activity is gotten by equating the reconnection flux F_m to the change in polar cap flux, which may be expressed in terms of Kp or AE. Thus, if the increase in Kp is from Kpa to Kpb, equation 16 gives

$$m \, (b, a) = [\, F_{pc} \, (Kpb) - F_{pc} \, (Kpa) \,] \, / \, F_o \tag{18}$$

$$= 1.524 \, (Kpb - Kpa) \tag{19}$$

Equation 19 is gotten from the linear fit of the polar cap flux with Kp, although using the actual values for the flux intercepted by the circular polar cap functions changes results by only a few percent at most. Thus, in a Kp change from 0 to 5, m = 7.6; and a change in Kp from 2 to 4 gives m = 3 0. Because of the multiparameter dependence of m given in equation 17 no simple unambiguous deduction can be made from its value alone.

Expressed in terms of AE, if the increase in AE is from AEa to AEb then the merging parameter is given by:

$$m(b, a) = 1.230 \left[AEb/100 - AEa/100 \right] \qquad (20)$$

Here again the linear fit of the polar cap flux to AE is used (equation 13).

The rate at which the polar cap changes size may be characterized by a convection parameter as follows. If the polar cap circle increases in angle from Φ_1 to Φ_2, the change in polar cap area is

$$A_2 - A_1 = \pi R^2 (\cos \Phi_1 - \cos \Phi_2)$$

To associate the expansion with convection, we write

$$\Phi_2 = \Phi_1 + \int_o^T v_{eq} dt/R$$
$$= \Phi_1 + \overline{v}_{eq} T/R \qquad (21)$$

Here $\overline{v}_{eq}$ is the average of the equatorward (or southward in the northern hemisphere) component of the convection velocity at the expanding polar cap boundary, and T is the duration of the expansion. We introduce a dimensionless convection parameter to represent the expansion by:

$$C_{eq} = \overline{v}_{eq} T/(\overline{v}_{eq} T)_o \qquad (22)$$

where

$$(\overline{V}_{eq}\ T)_o \equiv (10\text{m/sec}){\cdot}(3\ \text{hours}) = 108\ \text{km} \tag{23}$$

Combing equations 15 to 17,

$$C_{eq} = 1.05\ (\Phi_2 - \Phi_1) \tag{24}$$

In equation (24), angles are in degrees. The value $C_{eq} = 1$ corresponds to a change in size of the polar cap of 0.95 degrees taking place in 3 hours at an average convection expansion speed of 10m/sec (or in 1 hour at an average speed of 30m/sec). The predicted values of C_{eq} (Kpa, Kpb) are given in Table 1, followed by linear fits.

Table 13. The convection parameter C_{eq} for changes in Kp

Kp	1	2	3	4	5
$C_{eq}(0, Kp)$	2.74	3.70	5.14	6.47	7.25
$C_{eq}(1, Kp)$	---	0.958	2.40	3.73	4.51
$C_{eq}(2, Kp)$	---	---	1.44	2.77	3.55
$C_{eq}(3, Kp)$	---	---	---	1.33	2.11
$C_{eq}(4, Kp)$	---	---	---	---	0.777

$C_{eq}(0, Kp) = 1.52 + 1.18\ Kp$ $(Kp \geq 1)$
$C_{eq}(1, Kp) = -1.29 + 1.20\ Kp$ $(Kp \geq 2)$
$C_{eq}(2, Kp) = -1.63 + 1.05\ Kp$ $(Kp \geq 3)$
$C_{eq}(3, Kp) = -1.78 + 0.777\ Kp$ $(Kp = 4,5)$

The convection expansion parameter expressed in terms of AE is given in Table 14. The linear fits to the expansion parameter follow the table. The values of AE are determined by the binning process applied to the data.

Table 14. The convection expansion parameter for changes in AE. AE is in nT

AE	100	200	300	450	650
$C_{eq}(50, AE)$	2.46	3.77	5.25	5.91	7.28
$C_{eq}(100, AE)$	---	1.31	2.79	3.46	4.83
$C_{eq}(200, AE)$	---	---	1.48	2.14	3.52
$C_{eq}(300, AE)$	---	---	---	0.663	2.04
$C_{eq}(400, AE)$	---	---	---	---	1.37

$C_{eq}(50, AE) = 2.06 + 0.846 \ (AE/100) \qquad (AE \geq 100)$

$C_{eq}(100, AE) = 0.183 + 0.729 \ (AE/100) \qquad (AE \geq 200)$

$C_{eq}(200, AE) = -0.362 + 0.587 \ (AE/100) \qquad (AE \geq 300)$

$C_{eq}(300, AE) = -2.43 + 0.686 \ (AE/100) \qquad (AE \geq 450)$

Of course, the three parameters introduced (C_{eq}, m, and f) are not independent. Thus, the merging parameter satisfies the equations

$$m = (F_{to}/F_o) \ \Delta \ f$$
$$= (\pi R^2 B / F_o) \ \Delta \ (\cos \Phi)$$

Here $\Delta \ f = f(b) - f(a)$ is the change in the flux parameter from activity level a to activity level b, and $\Delta \ (\cos \Phi) = \cos \Phi b - \cos \Phi a$. The convection parameter enters through equation 24:

$$\Phi_b = \Phi_a + C_{eq}(a,b) \ /1.05$$

Harmonic function representation. Given the angles Φ and θ , the circle fit to the polar cap boundary is calculated from Equation 3. The circle so-obtained is also closely represented by the simple harmonic function

$$\vartheta = \Phi + \theta \cos \left(\phi - \phi_M \right) \tag{4}$$

43

With this representation the harmonic function and the circle match exactly at ϕ_M and $\phi_M + \pi$, and their difference is maximum midway between these meridians. The maximum difference in degrees between the circle and harmonic function for the parameters in Table 9 is 0.5 (Kp0), 0.6 (Kp1), 0.6 (Kp2), 0.4 (Kp3), 0.2 (Kp4), and 0.1 (Kp5).

G. Summary and Conclusions

The polar cap boundary as represented essentially by the high latitude termination of ion precipitation has been determined from DMSP measurements. A data base was assembled consisting of the measured ion boundaries, and a subset formed consisting of boundaries for which IMF data exists. The ion boundary was studied in terms of its empirical location, statistical characteristics, and by mathematical analysis.

The ion data base assembled is characterized by appreciable variation at each MLT although averages are often systematic and show regular trends. In particular, no parameter considered was found to have a strong correlation with the ion boundary location. The best, though only moderate, correlation was found between the ion poleward boundary and AE at most MLTs. Correlation is next best with Kp, then IMF Bz. No tendency for correlation was found with IMF By.

The lack of good correlation with the IMF is disappointing. One hour averaged values of IMF Bz and By were used, and perhaps using averaged values on a different time scale would improve results.

Average characteristics of the ion boundary latitude λ from the complete data base are indicated by the average values at noon and midnight:

$$\overline{\lambda} (12{:}00 \text{ MLT}) = (79 \pm 3)^\circ$$

$$\overline{\lambda} (24{:}00 \text{ MLT}) = (73 \pm 4)^\circ$$

Also, the results about dawn and dusk suggest that the ion boundary is shifted by 1 to 2 degrees towards dusk.

Extensive statistical analysis was performed on the data base. In all considerations, the average dayside boundary extends to higher latitudes than the nightside boundary, the geometrical center of the boundary curve in MLT is offset from the geomagnetic pole, and the average size of the area enclosed by the ion polar cap boundary increases at all MLTs with increased magnetic activity.

Linear regression analyses were made of the boundary location with AE, Kp, IMF Bz, IMF By, and other parameters. The correlation is best with AE (next with Kp and then IMF Bz). Multiple linear regression analysis, or non linear analysis using powers of the variables, did not improve the correlation coefficient $r(\lambda,\hat{\lambda})$ significantly between the predicted $\hat{\lambda}$ and observed λ boundary latitudes. With AE the correlation $r(\lambda,\hat{\lambda})$ was significant at all MLTs except within about 3 hours of midnight. There is essentially zero correlation of the empirical nightside ion boundary location with magnetic activity, no matter which magnetic parameter is used. This is a striking result since the determiniation of the nightside ion boundary location from the particle data is usually very well defined.

Perhaps the most reasonable interpretation of the small correlation is that the nightside ion boundary is frequently in motion, and that motion is about as likely to be poleward as equatorward regardless of the value of, say, AE. In particular the boundary motion is probably more rapid, i.e., takes place on a smaller time scale, than the one-hour averaged AE and IMF parameters used in this study. (One effort made to improve the correlation with the nightside boundary was to sort the data about midnight by the slope of AE. No substantial improvement in correlation with the location of the measured ion boundary resulted.) These conditions would mitigate the small correlation coefficients found at nightside MLTs. At other MLTs, post midnight through noon to pre midnight, the polar cap boundary location anticorrelates to a far greater degree with AE (or Kp or -IMF Bz). At these MLTs the ion boundary tends to expand, i.e., λ decreases, with magnetic activity.

Although the correlation between the measured and predicated ion boundaries, λ and $\hat{\lambda}$, is significant though modest other than in the midnight sector, the correlation between the average ion boundary and the predicted boundary is usually excellent at all MLTs. As a result a functional representation of the average polar cap ion boundary was derived.

A circle fit optimally to the average ion boundary gives an excellent representation at each magnetic activity level. The size of the circle expands significantly in a regular manner with magnetic activity. The center of the circle is always in the pre midnight sector and moves toward earlier MLTs (less regularly in latitude) with increased magnetic activity. Most of the increased area of the polar cap ion boundary with increased activity comes from expansion of the dayside boundary to lower latitudes. The average ion boundary at midnight does not expand significantly with magnetic activity. In the data binned by magnetic activity, the smallest polar cap comes, as expected, with the lowest magnetic activity bin: $Kp = 0$, $AE = 0$, or IMF $Bz > + 4$.

From the functional fits to the average polar cap ion boundary, heuristic parameters may be introduced relating to important physical variables. These include the polar cap magnetic flux through the average ion boundary, the area of the polar cap, and the rate of expansion of the ion boundary with increased magnetic activity. The heuristic parameters are a tail flux parameter, a merging parameter, and a convection parameter. The parameters are expressed in terms of their Kp and AE dependence and would be useful as indicators of average high latitude conditions in the absence of direct measurements.

REFERENCES

Akasofu, S.-I. and B. Tsurutani, Unusual auroral features observed on January 10-11, 1983 and their possible relation to the interplanetary Magnetic field, *Geophys. Res. Lett., 10*, 1086, 1984.

Coley, W. R., Spatial relationship of field-aligned currents, electron precipitation, and plasma convection in the auroral oval, *J. Geophys. Res., 88*, 7131, 1983.

Craven, J. D. and L. A. Frank, The temporal evolution of a small auroral substorm as viewed from high altitudes with Dynamics Explorer 1, *Geophys. Res. Lett., 12*, 465, 1985.

Craven, J. D. and L. A. Frank, Latitudinal Motions of the aurora during substorms, *J. Geophys. Res., 92,* 4565, 1987.

Frank, L. A. and K. L. Ackerson, Local-time survey of plasma at low altitudes over the auroral zones, *J. Geophys. Res., 77,* 4116, 1972.

Gurnett, and L. A. Frank,

Gussenhoven, M. S., Polar rain and the question of direct particle access, in *Electromagnetic Coupling in the Polar Clefts and Caps*, P. E. Sandholt and A. Egeland, eds., Kluwer Academic Publishers, 43, 1989.

Gussenhoven, M. S. and D. Madden, Monitoring the polar rain over a solar cycle: A polar rain index, *J. Geophys. Res., 95,* 10,399, 1990.

Gussenhoven, M. S., D. A. Hardy, N. Heinemann and R. K. Burkhardt, Morphology of the polar rain, *J. Geophys Res., 89*, 9785, 1984.

Gussenhoven, M. S., D. A. Hardy, and N. Heinemann, The equatorward boundary of auroral ion precipitation, *J. Geophys Res., 92*, 3273, 1987.

Hardy, D. A., Intense fluxes of low energy electrons at geomagnetic latitudes above 85°, *J. Geophys Res., 89*, 3833, 1984.

Hardy, D. A., W. J. Burke, M. S. Gussenhoven, N. Heinemann and E. Holeman, DMSP/F2 electron observations of equatorward auroral boundaries and their relationship to the solar wind velocity and the north-south component of the interplanetary magnetic field, *J. Geophys Res., 86*, 9961, 1981.

Hardy, D. A., M. S. Gussenhoven and E. Holeman, A statistical model of auroral ion precipitation, *J. Geophys Res., 94*, 370, 1989.

Hardy, D. A., M. S. Gussenhoven and E. Holeman, A statistical model of auroral electron precipitation, *J. Geophys Res., 90*, 4229, 1985.

Hardy, D. A., L. K. Schmitt, M. S. Gussenhoven, F. J. Marshall, H. C. Yeh, T. L. Schumaker, A. Huber and J. Pantazis, Precipitating electron and ion detectors (SSJ/4) for the block 5D/flights 6-10 DMSP satellites: Calibration and data presentation, *Rep. AFGL-TR-84-0317*, Air Force Geophysics Laboratory, Hanscom AFB, MA, 1984. ADA157080.

Harel, M., R. A. Wolf, P. H. Reiff, R. W. Spiro, W. J. Burke, F. J. Rich and M. Smiddy, Quantitative simulation of a magnetospheric substorm, 1, Model logic and overview, *J. Geophys Res., 86*, 2217, 1982.

Heelis, R. A., J. D. Winningham, W. B. Hanson and J. L. Burch, The relationship between high-latitude convection reversals and the energetic particle morphology observed by atmospheric explorer, *J. Geophys Res., 85*, 3315, 1980.

Hoffman, R. A., and J. L. Burch, Electron precipitation patterns and substorm morphology, *J. Geophys. Res., 78*, 2867, 1973.

Holzer, R. E., R. L. McPherron and D. A.Hardy, A quantitative model of the magnetospheric flux transfer process, *J. Geophys. Res., 91*, 3287, 1986.

Holzer, R. E. and J. A. Slavin, Magnetic flux transfer associated with expansions and contractions of the dayside magnetosphere, *J. Geophys Res., 83*, 3831, 1978.

Holzer, R. E. and J. A. Slavin, A correlative study of magnetic flux transfer in the magnetosphere, *J. Geophys Res., 84*, 2573, 1979.

Holzworth, R. H. and C.-I. Meng, Mathematical representation of the auroral oval, *Geophys. Res. Lett., 2*, 377, 1975.

Holzworth, R. H. and C.-I. Meng, Auroral boundary variations and the interplanetary magnetic field, *Planet. Space Sci., 32,* 25, 1984.

Iijima, T. and T. A. Potemra, Large-scale characteristics of field-aligned currents associated with substorms, *J. Geophys Res., 83,* 599, 1978.

Kamide, Y., J. S. Murphree, C. D. Anger, F. T. Berkey, and T. A. Potemra, Nearly simultaneous observations of field-aligned currents and visible auroras by the triad and ISIS 2 satellites, *J. Geophys Res., 84,* 4425, 1979.

Lassen, K., C. Danielson and C.-I. Meng, Quiet-time average auroral configuration, *Planet. Space Sci., 36,* 791, 1988.

Makita, K. and C.-I. Meng, Average electron precipitation patterns and visual auroral characteristics during geomagnetic quiescence, *J. Geophys Res., 89,* 2861, 1984.

Makita, K., C.-I. Meng and S.-I. Akasofu, Latitudinal electron precipitation patterns during large and small IMF magnitudes for northward IMF conditions, *Geophys Res., 93,* 97, 1988.

Makita, K., C.-I. Meng and S.-I. Akasofu, Temporal and spatial variations of the polar cap dimension inferred from the precipitation boundaries, *J. Geophys Res., 90,* 2744, 1985.

Makita, K., C.-I. Meng and S.-I. Akasofu, The shift of the auroral electron precipitation boundaries in the dawn-dusk sector in association with geomagnetic activity and interplanetary magnetic field, *J. Geophys Res., 88,* 7969, 1983.

McDiarmid, I. B., J. R. Burrows and Margaret D. Wilson, Comparison of magnetic field perturbations at high latitudes with charged particle and IMF measurements, *J. Geophys Res., 83,* 681, 1978.

McDiarmid, I. B., J. R. Burrows and Margaret D. Wilson, Large-scale magnetic field perturbations and particle measurements at 1400 km on the dayside, *J. Geophys Res., 84,* 1431, 1979.

Meng, Ching-I., The auroral electron precipitation during extremely quiet geomagnetic conditions, *J. Geophys Res., 86,* 4607, 1981.

Meng, C.-I. and H. W. Kroehl, Intense uniform precipitation of low energy electrons over the polar cap, *J. Geophys Res., 82,* 2304, 1977.

Meng, Ching-I., and Kazou Makita, Dynamic variations of the polar cap, in *Solar Wind-Magnetosphere Coupling,* Y. Kamide and J. A. Slavin, eds., Tokyo, Terra Scientific Publishing Company, (TERRAPUB), p. 605, 1986.

Meng, C.-I., R. H. Holzworth and S.-I. Akasofu, Auroral circle-delineating the poleward boundary of the quiet auroral belt, *J. Geophys Res., 82,* 164, 1977.

Moses, J. J. and G. L. Siscoe, Open flux merging in an expanding polar cap model, in *Modelling Magnetospheric Plasmas,* T. E. Moore and J. H. Waite, Jr., eds., Geophysical Monograph #44, Washington, D. C., Am. Geophys. Union 247, 1988.

Moses, J. J., G. L. Siscoe, N. U. Crooker and D. J. Gorney, IMF By and day-night conductivity effects in the expanding polar cap convection model, *J. Geophys Res., 92,* 1193, 1987.

Moses, J. J., G. L. Siscoe, R. A. Heelis and D. J. Winningham, Polar cap deflation during magnetospheric substorms, *J. Geophys Res., 94,* 3785, 1989.

Nakai, H. and Y. Kamide, Response of nightside auroral-oval boundaries to the interplanetary magnetic field, Moses, *J. Geophys Res., 88,* 4005, 1983.

Reiff, P. H., R. W. Spiro and T. W. Hill, Dependence of polar cap potential drop on interplanetary parameters, *J. Geophys Res., 86,* 7639, 1981.

Sheehan, R. E. and R. L. Carovillano, Characteristics of the Equatorward auroral boundary near midnight determined from DMSP images, *J. Geophys Res., 83,* 4749, 1978.

Siscoe, George L., Polar cap size and potential: A predicted relationship, *Geophys. Res. Lett., 9,* 672, 1982.

Siscoe, G. L. and T. S. Huang, Polar cap inflation and deflation, *J. Geophys Res., 90,* 543, 1985.

Stern, D. P., The origin of Birkeland currents, *Rev. Geophys., 21,* 125, 1983.

Torbert, R. B., C. A. Cattell, F. S. Mozer and C.-I. Meng, The boundary of the polar cap and its relation to electric fields, field-aligned currents and auroral particle precipitation, in *Physics*

of Auroral Arc Formation, S.-I. Akasofu and J. Kan, eds., Geophysics Monograph no. 25, American Geophysical Union, Washington, DC, p. 143, 1981.

Winningham, J. D., F. Yasuhara, S.-I. Akasofu, and W. J. Heikkila, The latitudinal morphology of 10-eV to 10-keV electron fluxes during magnetically quiet and disturbed times in the 2100-0300 MLT sector, *J. Geophys Res., 80,* 3148, 1975.

Yeager, D, M. and L. A. Frank, Low-energy electron intensities at large distances over the earth's polar cap, *J. Geophys Res., 81,* 3966, 1976.

3. ANALYTICAL STUDY OF IONOSPHERIC CURRENTS

A. Introduction

Plasma convection in the inner magnetosphere, field aligned currents, and particle precipitation result in direct magnetospheric coupling to the ionosphere with associated dynamical effects that occur on a global scale. The global response of the ionosphere in the coupling process has been of widespread interest throughout the modern era of space science, with major early contributions from Fejer (1964) and the benchmark work of Vasyliunas (1970). The current work builds upon the approach and model of Vasyliunas and differs from it primarily in the complexities introduced, some of which had little basis for consideration, say, two decades ago. In our considerations, the ionosphere is a spherical conducting shell with surface currents driven by the magnetospheric coupling processes. The coupling is modelled by impressed voltages or input-output currents of magnetospheric origin. In the model, the magnetic field is radial and uniform Hall and Pedersen conductivities (height integrated) prevail throughout the spherical ionospheric shell. The direction of the magnetic field is inwards in the northern hemisphere. Discontinuities in the conductivities are introduced, but except at discrete boundaries the Hall and Pedersen conductivities are uniform. With these conditions, the model may be developed analytically and yet maintains a suitable degree of realism.

In all cases, the model has an electrical potential across the polar cap corresponding to a uniform, dawn-to-dusk, cross-tail electric field. The polar cap boundary is a circle at the colatitude θ_1 which is taken to be 18° in the numerical calculations. The auroral zone encompasses the latitudinal range from θ_1 to θ_2, where $\theta_2 = 26^o$ is used in the numerical calculations. Thus:

$$\text{Polar Cap:} \qquad \theta \leq \theta_1 \qquad\qquad (1)$$

Auroral Zone: $\theta_1 \leq \theta \leq \theta_2$ (2)

The polar cap boundary is coincident with the poleward boundary of the auroral zone.

The auroral zone coincides with the azimuthally symmetrical ring between θ_1 and θ_2.

The equatorial boundary of the auroral zone is the circle θ_2. Longitudinal variations in

the geometry of the auroral zone are not included in the model.

In the model, the auroral zone is normally a region of enhanced electrical

conductivity. The coupling to the magnetosphere is introduced through imposing

appropriate boundary conditions at θ_1 and θ_2. An equatorial boundary condition may

also be needed. The boundary condition at θ_1 (similarly at θ_2) may be specified in terms

of either the electrical potential or the electrical current. At θ_1, the electrical potential is

always used:

$$V(\theta_1, \phi) = V_1 \sin \phi$$ (3)

The choice (3) corresponds to a uniform cross-tail electric field. At θ_2 the potential may be

phase-shifted and changed in magnitude:

$$V(\theta_2, \phi) = V_2 \sin (\phi + \phi_2)$$ (4)

Here, (θ, ϕ) are the colatitude and longitude (or local time) on the spherical ionosphere,

$V(\theta, \phi)$ is the electrical potential, and ϕ_2 is a constant phase. The corresponding angle

$\phi_1 = 0$ is used in equation (3) because $\phi = 0$ is taken to be the midnight meridian. Looking

down on the ionosphere, ϕ increases in value from the midnight meridian (hence, $\phi = 90°$

at dawn and $270°$ at dusk). The amplitudes V_1 and V_2 in equations (3) and (4) are

constants. The quantity $(2V_1)$ is the cross-cap potential difference.

Field-aligned currents of magnetospheric origin are allowed to enter the ionosphere at θ_1 and θ_2. The so-called Region I currents enter at θ_1 and Region II currents at θ_2. Additional field-aligned input currents will be considered in the polar cap to represent DPZ and DPY effects, as explained below.

B. Basic Equations

Using constant, height-integrated conductivities, neglecting neutral winds, and assuming a radial magnetic field, the steady state ionospheric surface current $\mathbf{J}$ satisfies the field equation:

$$\text{div } \mathbf{J} = - \Sigma p \, \nabla^2 V \tag{5}$$

Here Σp is the height-integrated Pedersen conductivity and V is the electrical potential. The ionospheric currents are distributed on the sphere geomagnetically centered. From equation (5) it follows that field aligned currents (FACs) may exist at points where $\nabla^2 V \neq 0$ and that the coupling between ionospheric and FACs is accomplished primarily through the Pederson conductivity. At θ_1 a FAC density (Region I) is assumed of the form

$$j(I) = (I_1/R^2) \, \delta(\theta - \theta_1) \sin (\phi + \delta_1) \tag{6}$$

Here R is the radius of the ionospheric sphere, I_1 is a positive constant with the dimensions of current, $\delta(\theta - \theta_1)$ is the Dirac delta function, and δ_1 is a constant that accounts for any phase shift between the FAC and polar cap potential. The total current into the ionosphere due to the FAC at θ_1 is $2I_1 \sin \theta_1$ (and an equal current leaves the ionosphere at θ_1). Because I_1 is positive, the Region I FAC enters the ionosphere at the colatitude θ_1 in the azimuthal interval $-\delta_1$ to $-\delta_1 + \pi$.

In the ionosphere, the electric field is given by

$$\mathbf{E} = - \nabla V \tag{7}$$

and the surface current density by

$$J = \Sigma_p \, E - \Sigma_H \, \hat{r} \times E \tag{8}$$

The first term in equation (8) is the Pedersen current and the second is the Hall current.

The ratio of Pedersen to Hall current equals the ratio of Pedersen to Hall conductivity:

$$J_H/J_p = \Sigma_H/\Sigma_p \equiv \Sigma \tag{9}$$

The ratio Σ normally is about 2, though values between 1 and about 3.5 are representative. Thus, in the ionosphere net Hall effects often tend to be larger than Pedersen effects. The angle between the total current and the electric field is arctan Σ, which increases from $45°$ for $\Sigma = 1$ to $74°$ for $\Sigma = 3.5$. The convection velocity is

$$V = (c/B) \, \hat{r} \times E \tag{10}$$

Thus the convection velocity and the Hall current are anti-parallel, and both are coincident with the ionospheric equipotentials. The circulation of the convection is counterclockwise about a potential high and clockwise about a potential low.

The potential in the polar cap $(\theta \le \theta_1)$ is

$$V(\theta, \phi) = V_1 \, (y/y_1) \sin \phi \tag{11}$$

where y is the latitude variable given by

$$y \, (\theta) = \tan \theta/2 \tag{12}$$

$y_1 = y(\theta_1)$, and the boundary condition of equation (4) is satisfied. Other relations in the polar cap are:

$$E = (V_1/R \sin \theta) \, (y/y_1) \tag{13}$$

$$J = \Sigma_p \, \sqrt{1 + \Sigma^2} \, E \tag{14}$$

Here E is the magnitude of the electric field (the direction of which is approximately constant from dawn to dusk across the cap), and J is the magnitude of the total polar cap surface current density.

With equation (5) and the potential boundary conditions of equations (3) and (4) at θ_1 and θ_2, respectively, the solution for the potential is always of the form

$$V(y,\phi) = A(y) \sin \phi + B(y) \cos \phi \tag{15}$$

and the latitude dependent functions A and B may take on different values in different zones of the ionosphere. The zones are enumerated as follows:

Zone I: The polar cap $(\theta < \theta_1)$ (16)

Zone II: The auroral zone $(\theta_1 < \theta < \theta_2)$ (17)

Zone III: Equatorward of the auroral zone $(\theta_2 < \theta)$ (18)

In zone I, comparing equations (7) and (15), the solution is:

Zone I: $A = V_1 (y/y_1), \quad B = 0$ (19)

Our solution in zone II is model dependent, and we shall discuss two basic cases, A and B which differ in the definition of zones II and III. In Case A, only zones I and II exist. Zone II is the auroral zone that extends from the polar cap boundary to the south geomagnetic pole, i.e., $\theta_1 < \theta \le \pi$. In Case B, zone II is the auroral zone and zone III is the remainder of the ionospheric sphere to the south geomagnetic pole. Because our primary interests are high latitude effects, an equatorial boundary condition will not be introduced.

The polar cap is the same for Cases A and B and the solution for the potential is given in equation (19). The solutions in zones I and II for Case A and Case B are as follows:

Case A. Zone I $(\theta < \theta_1)$:

$A = V_1 (y/y_1), \quad B = 0$ (20)

Zone II $(\theta_1 < \theta \le \pi)$

$A = V_1 (y_1/y), \quad B = 0$ (21)

Case B. Zone I $(\theta < \theta_1)$:

$A = V_1(y/y_1), \quad B = 0$ (22)

Zone II $(\theta_1 < \theta < \theta_2)$

Here we write the potential in the form

$V(y, \phi) = A \sin \phi + B \sin (\phi + \phi_2)$ (23)

This form is equivalent to equation 15 and more easily accommodates the boundary condition requirements of equations 3 and 4. Thus, at $y_1 = y(\theta_1)$

$$A(y_1) = V_1 \qquad (24)$$

$$B(y_1) = 0 \qquad (25)$$

whereas at $y_2 = y(\theta_2)$

$$A(y_2) = 0 \qquad (26)$$

$$B(y_2) = V_2 \qquad (27)$$

The solutions for the functions A and B are given below in equations 66 and 67.

In each case, Region I currents couple to the ionosphere at θ_1. In Case A, there are no Region II currents. In Case B, Region II currents couple to the ionosphere at θ_2. The Region I FAC density is specified in equation (6), and the Region II FAC density is defined similarly by:

$$j(II) = -(I_2/R^2)\, \delta(\theta - \theta_2)\, \sin(\phi + \delta_2) \qquad (28)$$

The negative sign in (28) is introduced to suggest that the Region I and Region II currents are out of phase. The actual phase relationship depends on the values of the constants δ_1 and δ_2 which are unconstrained.

Geometrical assumptions made are that the polar cap boundary potential (equation 3) and the Region I FAC (equation 6) occur at the same co-latitude (θ_1); and the Region II FAC occurs at the equatorward boundary of the auroral zone (θ_2). These are rather natural choices for the location of the field aligned currents, but other locations are possible. The choices are "natural" because the field aligned currents are then co-located with the boundaries of the auroral zone at which the ionospheric conductivities are essentially discontinuous.

With uniform ionospheric conductivities in each zone, once the potential distribution is specified at θ_1 and θ_2 (by equations 3 and 4) the global distribution of

ionospheric currents is uniquely determined at least in zones I and II (and if there is no additional equatorial boundary condition, the ionospheric currents are determined globally).

In the polar cap (zone I), the electric field is given by

$$\mathbf{E}\,(\mathrm{I}) = -E(y)\,(\sin\phi\,\hat{\theta} + \cos\phi\,\hat{\phi}) \tag{29}$$

The electric field is directed dawn-to-dusk across the spherical polar cap. The magnitude of the field is

$$E\,(y) = E\,(0)\,(1+y^2) \tag{30}$$

where

$$E\,(0) = V_1/2Ry_1 \tag{31}$$

is the intensity at the geomagnetic pole. The results in equations (29) and (13) are identical. The components of the surface current density in the polar cap are:

$$J_\theta = -\,E(y)\,(\Sigma_p \sin\phi + \Sigma_H \cos\phi) \tag{32}$$

$$J_\phi = -\,E(y)\,(-\Sigma_H \sin\phi + \Sigma_p \cos\phi) \tag{33}$$

The magnitude of the current density in the polar cap is given in equation 14, in terms of which Equations (32) and (33) give

$$J_\theta = -\,J(y)\cos(\phi - \varepsilon) \tag{34}$$

$$J_\phi = J(y)\sin(\phi - \varepsilon) \tag{35}$$

where

$$\tan\varepsilon = \Sigma_p/\Sigma_H = 1/\Sigma \tag{36}$$

The surface current density is tangent to the ionospheric sphere in a fixed direction across the polar cap, inclined at the angle ε with respect to the noon-midnight meridian and pointing from the morning into the afternoon quadrant. The angle between the electric field and the surface current is $(\pi/2 - \varepsilon)$. The Hall and Pedersen components of the surface current are given by

$$J_H = J \cos\varepsilon \tag{37}$$

$$J_p = J \sin\varepsilon \tag{38}$$

At θ_1, the balance of current relates the Region I FAC and the θ-component of the ionospheric current:

$$I_1 \sin (\phi + \delta_1) = R \, (J_\theta^{II} - J_\theta^{I}), \text{ at } \theta = \theta_1 \qquad (39)$$

In terms of the potential, J_θ is given by

$$J_\theta = \frac{-1}{R \sin \theta} \left(\Sigma_p \, y \, \frac{\partial V}{\partial y} + \Sigma_H \frac{\partial V}{\partial \phi} \right) \qquad (40)$$

Equation (39) is valid for all ϕ and determines the amplitude I_1 and phase δ_1 of the Region I FAC required for current continuity. The total Region I FAC that enters the ionosphere (and the total that leaves) is $2I_1 \sin \theta_1$. The FAC enters the ionosphere at θ_1 in the azimuthal, half-circular interval $(- \delta_1, \pi - \delta_1)$ and is distributed between zone I and zone II. The total current in the polar cap I_{pc} is given by the integral

$$I_{pc} = \int J \cdot dA = -R \sin \theta_1 \int d\phi \, J_\theta$$

where the integration is at θ_1 and extends from $\varepsilon - \pi/2$ to $\varepsilon + \pi/2$. With (34) the result is

$$I_{pc} = 2V_1 \, \Sigma_p \, \sqrt{1+\Sigma^2} \qquad (41)$$

The current in the auroral zone depends on the solution in zone II which depends on the boundary condition at θ_2.

As demonstrated in equations 20-27, given the potential boundary conditions and uniform ionospheric conductivity, the potential and the electric field are determined globally from Laplace's equation. Given the ionospheric conductivities, the surface current density is determined by equation 8. The continuity of the ionospheric current prescribes what FAC must be present, as in equation 39.

To develop guidelines and insight, the results of the simplest example of Case A are presented first.

C. The Potential for Region I Currents (Case A)

In Case A there are only two zones, the polar cap $(\theta < \theta_1)$ and the auroral zone $(\theta > \theta_1)$. The solution for the ionospheric potential is given in equations 20 and 21. With equation 40, the meridional component of the surface current in the polar cap satisfies

$$R \sin \theta_1 \, J_\theta^I (\theta_1) = -(I_{pc}/2) \cos (\phi - \varepsilon) \tag{42}$$

where I_{pc} is the total polar cap current given in equation 41. Similarly, the meridional component of the surface current in zone II satisfies

$$R \sin \theta_1 \, J_\theta^{II} (\theta_1) = -(I_{II}/2) \cos (\phi + \varepsilon) \tag{43}$$

where I_{II} is the magnitude of the total auroral zone current (zone II) given by

$$I_{II} = 2 \, V_1 \, \Sigma_p^{II} \sqrt{1+\Sigma^2} \tag{44}$$

Defining

$$q = \Sigma_p^I / \Sigma_p^{II} \tag{45}$$

the total currents in zones I and II are related by

$$I_{pc} = q \, I_{II} \tag{46}$$

The ionospheric zone with the greater Pedersen conductivity (normally, the auroral zone) carries the greater total current.

At the boundary θ_1, current flows into the polar cap in the half-circular arc given by the azimuthal angular range of

$$-\frac{\pi}{2} + \varepsilon \le \phi \le \frac{\pi}{2} + \varepsilon \tag{47}$$

whereas current flows into the auroral zone in the half-circle shifted counterclockwise by the angle $\pi - 2\varepsilon$ given by

$$\frac{\pi}{2} - \varepsilon \le \phi \le \frac{3\pi}{2} - \varepsilon \tag{48}$$

Introducing the dimensionless Region I FAC variable,

$$\kappa = I_1 \sin \theta_1 / V_1 \, \Sigma_p^{II} \tag{49}$$

the continuity of current specifies the magnitude and phase of the Region I FAC in terms of the ionospheric conductivity variables through the relations:

$$\kappa(q, \Sigma) = \sqrt{(1+q)^2 + (1-q)^2 \, \Sigma^2} \tag{50}$$

$$\tan \delta_1(q, \Sigma) = - (1-q) \Sigma/(1+q) \tag{51}$$

For q<1 (i.e., an enhanced auroral zone Pedersen conductivity), the phase δ_1 is negative and the Region I FAC enters the ionosphere in the half circle extending counterclockwise from a postmidnight location (at the MLT corresponding to the phase - δ_1) to a post noon location. The dependence on conductivity of the phase and intensity of the Region I FAC is demonstrated in Figure 12.

In Figure 12, the phase δ_1 and intensity κ are plotted versus q with Σ as a parameter. The phase is always negative and for q=1/2 has the values $-33.7°$ for $\Sigma=2$ and $-49.4°$ for $\Sigma=3.5$, corresponding to MLTs of 02:25 and 03:29, respectively. For given Σ, the FAC intensity parameter κ has an extremum at which:

$$q_0 = (\Sigma^2-1)/(\Sigma^2+1) \tag{52}$$

$$\kappa(q_0, \Sigma) = \sqrt{2 (1+q_0)} \tag{53}$$

$$\delta_1(q_0, \Sigma) = - \varepsilon \tag{54}$$

The Region I FAC enters the ionosphere along the arc from $-\delta_1$ to $-\delta_1+\pi$, and the total entering current is apportioned between the polar cap and zone II. At the minimum, the net FAC into the polar cap is zero and all enters the (more conducting) auroral zone. The ratio of the total Region I FAC into the ionosphere to the total auroral zone current is given by:

$$\left(\kappa/\sqrt{1+\Sigma^2} \right) \leq 1 \tag{55}$$

The inequality in equation 55 applies in the parameter domain q < 1 and $\Sigma > \sqrt{3}$, so that in the parameter range of interest the total auroral current would normally exceed the total Region I FAC into the ionosphere.

For given Σ, as seen in Figure 12, the phase δ_1 becomes more negative as q $\rightarrow$ 0, indicating that the Region I FAC rotates counterclockwise as the auroral Pedersen conductivity is increased. As the FAC rotates, its intensity also changes. The representative changes in phase $\Delta\delta_1$ and relative intensity for q going from 0.5 to 0.1 are listed in Table 15.

R1 - FAC degrees phase

R1 - FAC intensity
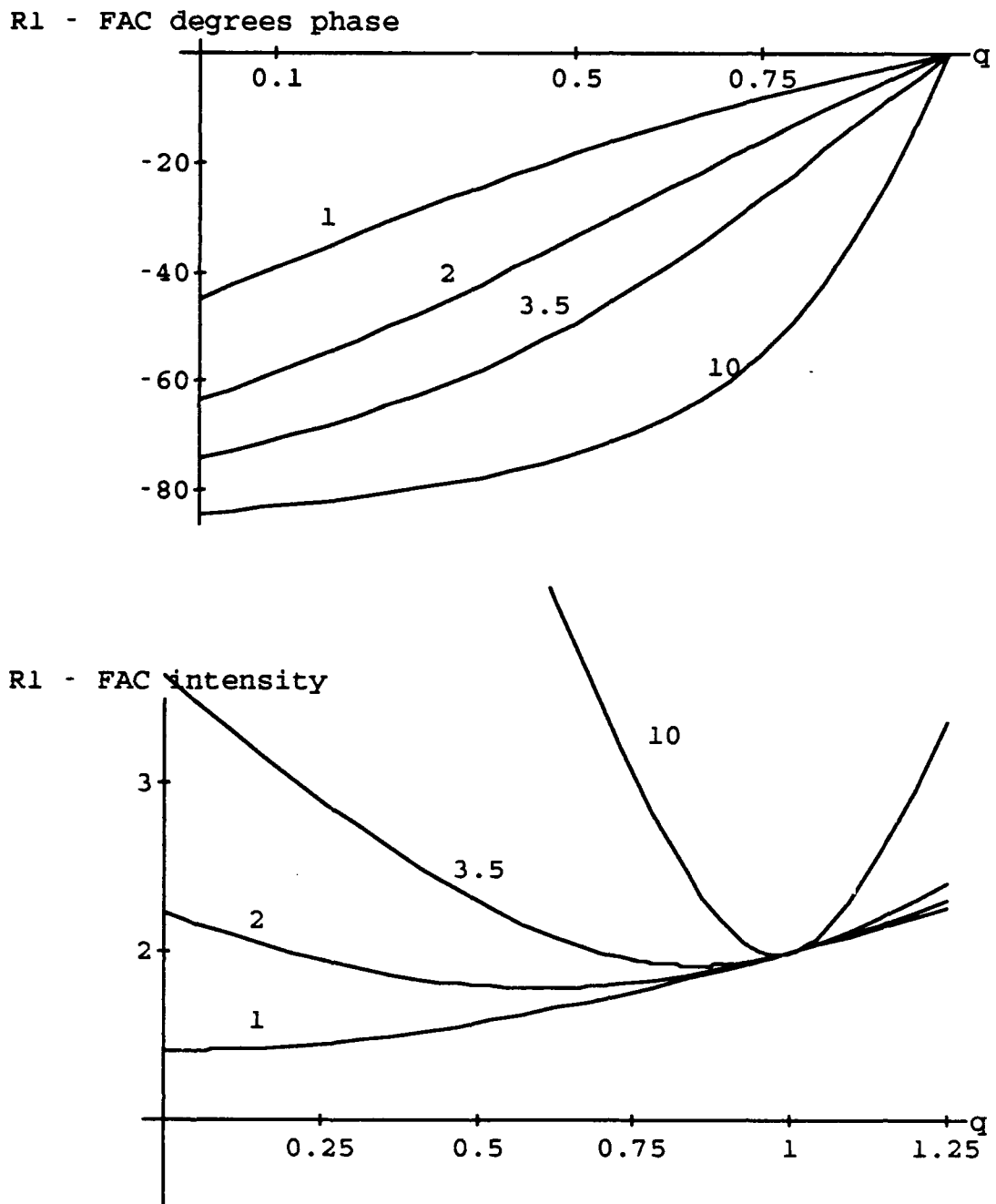
Figure 12. The phase and amplitude of the Region I FAC versus q for given Σ . The curves in the upper figure are of the phase δ_1 for q $\leq$ 1. The value of Σ (1,2,3.5,and 10) labels the curves. In the same format, the amplitude κ is presented in the lower figure.

Table 15. Region 1 FAC phase and intensity changes.

Σ	1	2	3.5	10
ϵ	45	27	16	6
$\Delta\delta_1$	21	25	21	10
r	0.9	1.2	1.4	1.7

The angles ϵ and $\Delta\delta_1$ are in degrees for the value of Σ in each column. The values of $\Delta\delta_1$ and r result from the change in q from 0.5 to 0.1. r is the intensity ratio.

The phase relationships of the many currents at θ_1 are shown schematically in Figure 13. The solid circle in Figure 13 is the polar cap boundary, and the arcs (each a half circle) ar all located at θ_1 though shown slightly displaced from θ_1 for clarity. The outer small-dashed arc is the locus where the Region I field aligned current feeds into the ionosphere. The inner large-dashed arc is the locus where the zone I ionospheric current flows into the polar cap. The outer solid arc is the locus where the zone II ionospheric current flows into the auroral zone. The union of the ionospheric arcs must exceed the full extent of the small-dashed arc to conserve current: along the small-dashed arc the Region I FAC must feed current into either the auroral zone or the polar cap. Where the FAC, polar cap and auroral currents coexist, the field aligned current feeds into both the polar cap and the auroral zone. Where only two arcs coexist, say FAC and auroral, then all of the field aligned current (and in this case some additional polar cap current) feeds directly into the auroral zone. The outermost arcs refer to the azimuthal current and mark where a westward current flows at θ_1 in the polar cap and in the auroral zone.

As the ionospheric conductives are varied, the arc locations rotate subject to constraints. For fixed Σ, the ionospheric currents are fixed in direction, corresponding to fixed locations for the polar cap and auroral arcs, in Figure 13. The value q = 0 corresponds
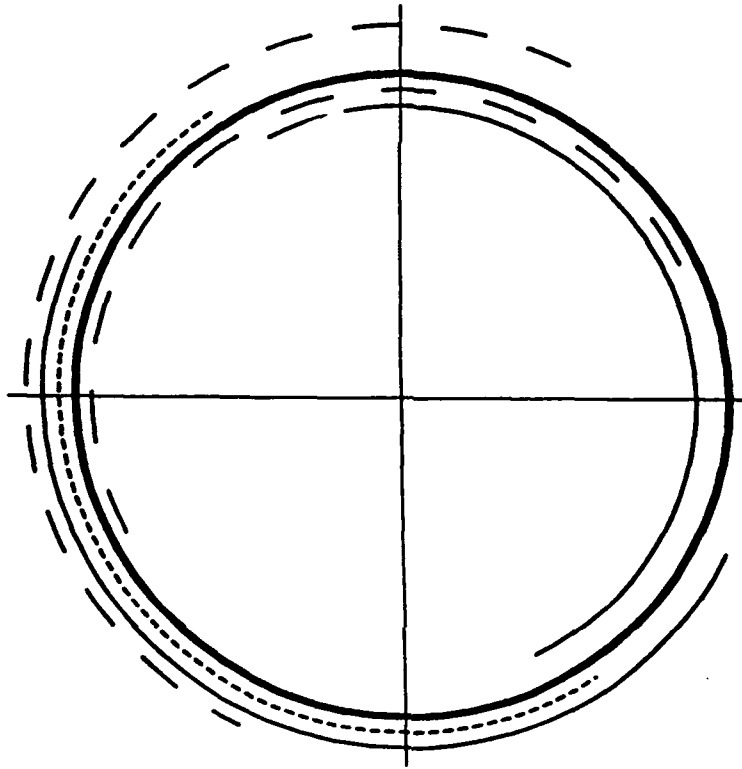
Figure 13. Schematic of boundary currents for Case A. The solid circle is the polar cap boundary at θ_1, with displayed magnetic local time. The five other curves are arcs, actually half circles, that occur at θ_1, but are shown slightly displaced so that they may be distinguished from each other. Counting from within the polar cap, the first (solid curve) and fifth (long dashes) arcs which are the innermost and outermost arcs, are where the polar cap and/or auroral curent, respectively, has a westward component. The second arc (long dashes) is the locus at θ_1, where the ionospheric current flows into the polar cap (zone I). The third arc (short dashes) is the locus at θ_1, where the ionospheric current flows into the auroral zone (zone II). The figure is for q=1/2 and Σ=2 , which gives ε = 27°and δ_1= -34°.

62

to an infinitely conducting auroral zone. For $q = 0$, $\tan \delta_1 = -\Sigma$ and $\delta_1 = -\pi/2 + \varepsilon$. For this value the FAC and auroral arcs coincide; the polar cap current is zero for each ϕ; the ratio (55) is one; and all of the field aligned current feeds directly into the auroral zone. As q increases, the relative conductivity of the polar cap increases and the FAC arc in the figure rotates monotonically clockwise (coinciding with the polar cap arc in the limit of infinite q).

For $q = 1$, the Pedersen conductivity is continuous at θ_1. Here $\delta_1 = 0$ and the FAC has the same phase as the potential; $\kappa = 2$ and the FAC is independent of the Hall conductivity (i.e., Σ); and the total polar cap and auroral currents are equal (equation 46).

In Figure 14, the set of figures is of the intensity and phases of currents at θ_1, the polar cap boundary, as required by the continuity equation. Each column in the figure has a fixed value of q for selected values of Σ. Each row has a fixed value of Σ. All currents are in the same units of the Region I FAC used in equation 49. In each plot, the small-dashed curves are the Region I FAC, the large-dashed curves the polar cap current, and the solid curves the auroral currents. Positive values for each curve are for "currents in", and negative values for "current out" at θ_1. The label of each figure indicates the conductivity values in the form Currents [q, Σ]. The format used in Figures 13 and 14 refer to the currents in the same manner.

For Case A, the magnitude of the ionospheric electric field and the surface current density are independent of azimuth. Across the polar cap boundary the magnitude and ϕ-component of the electric field are continuous, and the θ-component reverses direction. The current changes magnitude at the polar cap boundary if the conductivity (through q and Σ) changes across the boundary. The latitude dependence of the electric field and current intensity are shown in Figure 15.

63
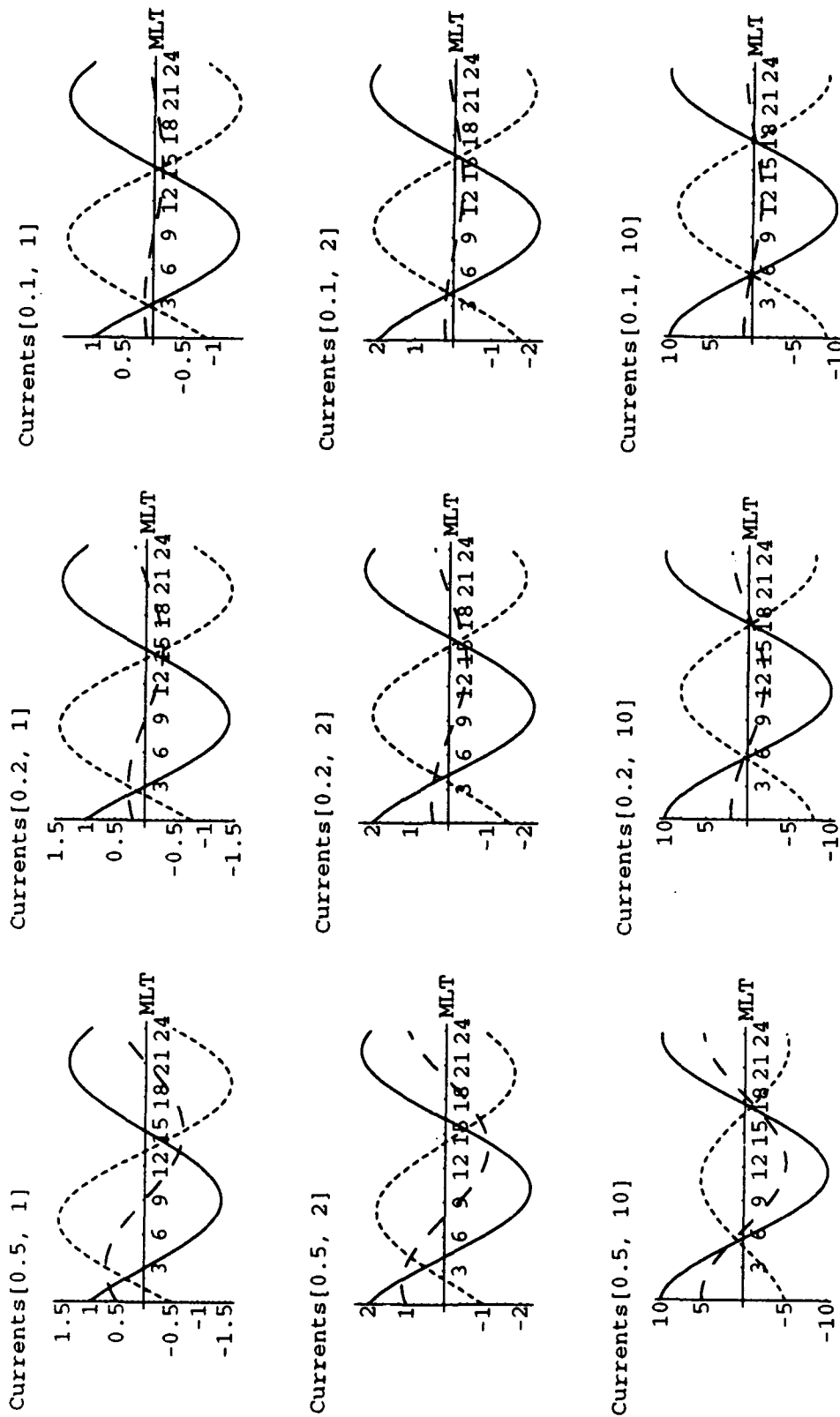
Figure 14.   Ionospheric and Region I FAC at the polar cap boundary.   Each plot gives
current intensity versus MLT for specific values of [q,Σ].   The small-dashed curves are
of the Region I FAC, the long-dashed curves the polar cap current, and the solid curves the
auroral current.   Positive current is for "current in", and negative values for "current out" at
the polar cap boundary.

64

If the field intensity E is given in units of $(V_1 y_1/2R)$ and the current intensity J in units of $(\Sigma_p^{II} V_1 y_1/2R \sqrt{1+\Sigma^2})$, then J = qE in the polar cap and J = E in zone II. In Figure 15, upper diagram, J and E are plotted in these units as a function of latitude. The q=1 curve gives E (which equals J for q=1 in the units chosen). For q<1, J is decreased in the polar cap as shown in Figure 15 for q=0.5 and q=0.1. As q decreases, the auroral zone current density is enhanced at the polar cap boundary to an ever increasing degree. The fraction of the power dissipated in the polar cap and the auroral zone is shown in the lower diagram of Figure 15.

The power density (watts/m^2) at any point in the ionosphere is given by

$$\mathbf{J} \cdot \mathbf{E} = \Sigma_p E^2 \tag{56}$$

which is independent of the Hall conductivity for Case A. Because the power density is everywhere positive, the ionosphere is everywhere dissipative. The energy dissipated in the ionosphere is provided by the FACs which are of magnetospheric origin. The total power P dissipated in the ionosphere is given by

$$P = (1 + q) P_o \tag{57}$$

where

$$P_o = \pi \Sigma_p^{II} V_1^2 \tag{58}$$

P_o is the power dissipated in zone II and qP_o is the power dissipated in the polar cap. Since q<1, more power is dissipated in zone II (the better conductor) than in the polar cap. (The result is characteristic of two resistors connected in parallel in a simple DC-circuit.) The fraction of the total power dissipated in the polar cap is q/(1+q), and the fraction dissipated in zone II is 1/(1+q); the fractions are shown in Figure 15.

For an enhanced conductivity in the auroral zone, the power density is largest in zone II near the polar cap boundary θ_1 where the ionospheric current intensity is largest. For

Case A
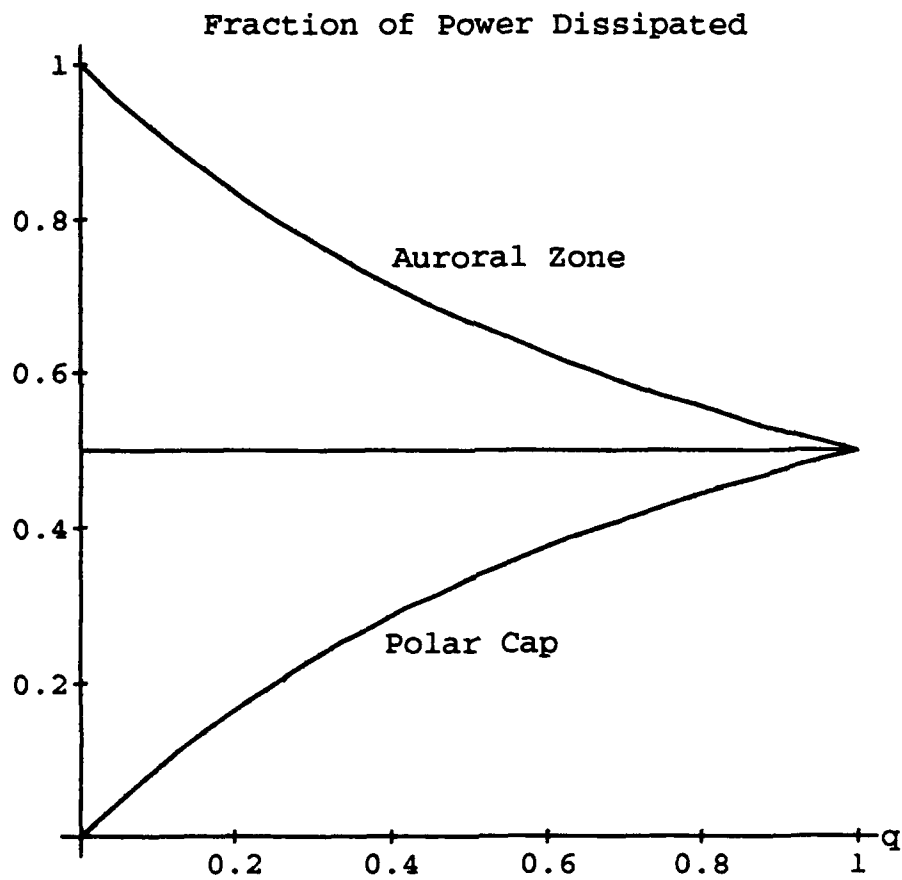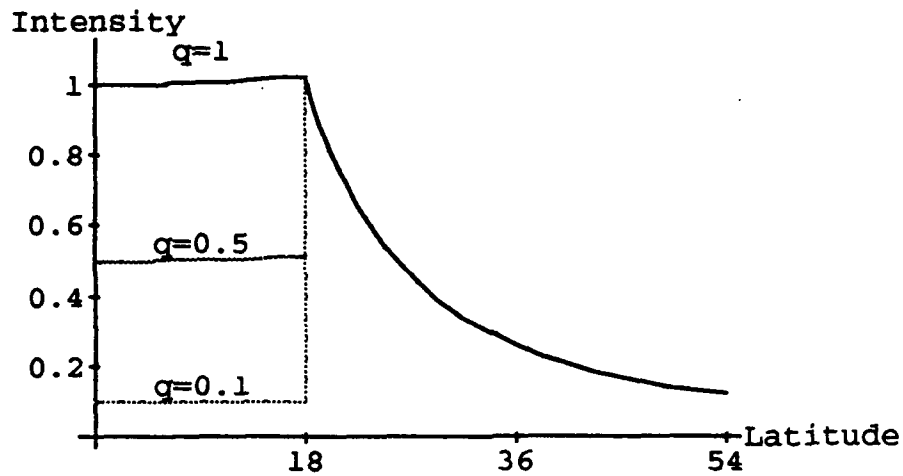
Figure 15. Field intensities and power dissipated. The upper diagram shows the electric field and current density magnitudes as a function of latitude. The units chosen are explained in the text. The lower figure gives the fraction of the power dissipated as a function of q in the auroral zone (upper curve) and the polar cap (lower curve).

example, a power equal to that dissipated in the polar cap is dissipated in the auroral zone

ring of latitudinal size $\Delta\theta$ located at the polar cap boundary, where

$$\Delta\theta = 2 \text{ Arctan } (y_1/\sqrt{1-q}) \tag{59}$$

With $\theta_1=18°$: $\Delta\theta=7°$ for $q=1/2$; and $\Delta\theta=1°$ for $q=1/10$.

The electric field lines satisfy the equation

$$E_\theta/E_\phi = d\theta/\sin\theta \ d\phi = dy/y \ d\phi \tag{60}$$

and the current density field lines satisfy

$$J_\theta/J_\phi = dy/y \ d\phi \tag{61}$$

In the polar cap, the ratios of components are:

$$E_\theta/E_\phi = \tan\phi \qquad\qquad J_\theta/J_\phi = \tan(\phi + \pi/2 - \varepsilon) \tag{62}$$

In zone II, the ratios are:

$$E_\theta/E_\phi = \tan\phi \qquad\qquad J_\theta/J_\phi = -\tan(\phi + \varepsilon - \frac{\pi}{2}) \tag{63}$$

Equation 62 indicates that at each point in the polar cap the ratio of field components is

independent of latitude and the current density is rotated clockwise by the angle $\pi/2 - \varepsilon$

from the electric field. Equation 63 indicates that in zone II the current density is rotated

counterclockwise by the angle $\pi/2 - \varepsilon$ from the electric field. These properties are

demonstrated in Figure 16 where the electric field lines are shown in the upper diagram and

the current density lines in the lower diagram for $\varepsilon = 27°$.

The equipotential lines and the convection pattern for Case A are shown in Figure 17.

The convection velocity is parallel to the equipotential lines, circulating counterclockwise

about the potential high at 06:00 MLT and clockwise about the potential low at 18:00 MLT,

as shown in the lower diagram of Figure 17. The convection pattern for Case A is the classic

two-cell pattern with uniform anti-sunward flow across the cap.

The total current density shown in Figure 16 has Pedersen and Hall components.

Electric Field

Surface Currents
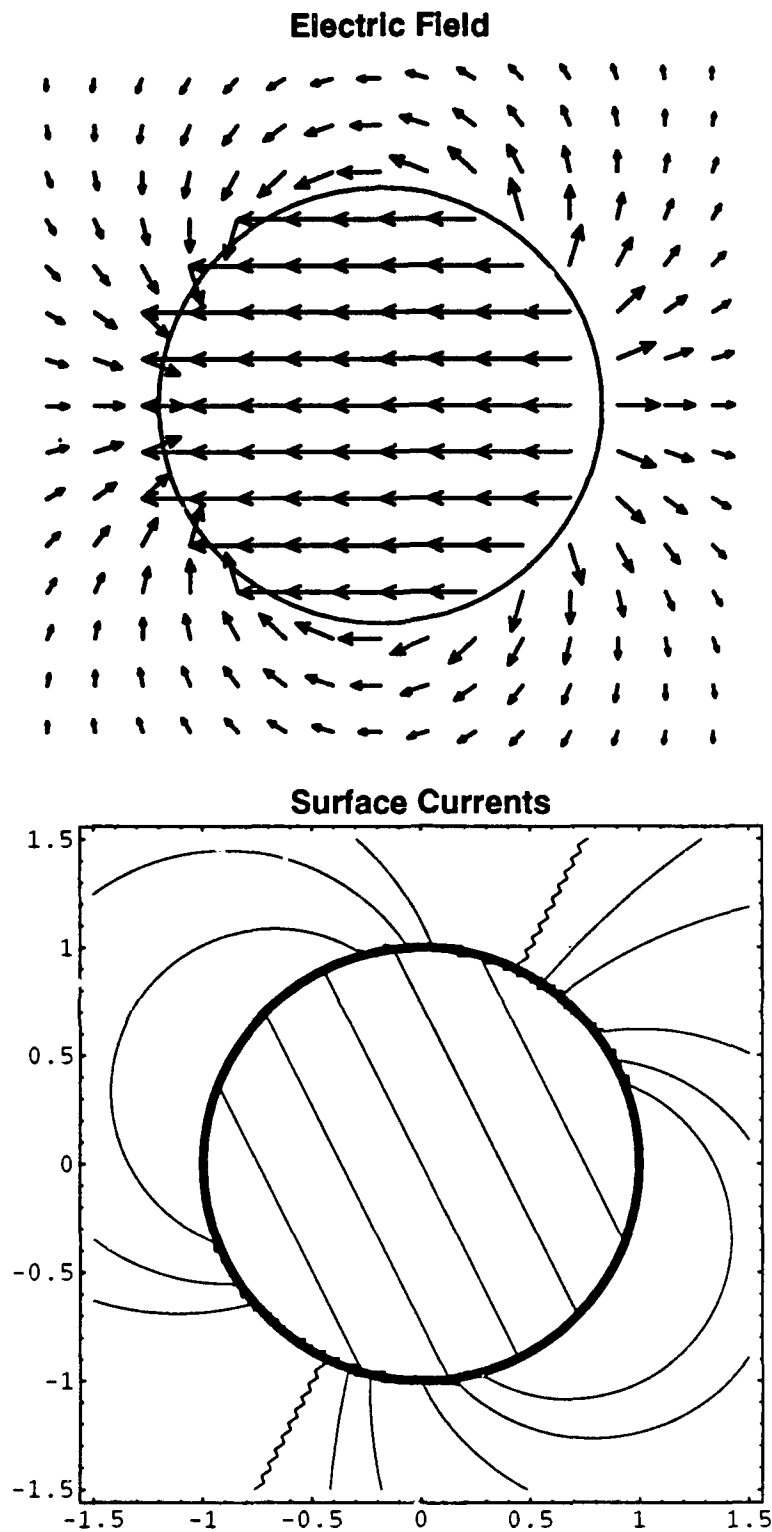
Figure 16. Electric field lines and current density lines for Case A. The diagrams are polar plots in MLT where loc⌐l midnight is at the bottom of the figures. The circle is the polar cap boundary. The dirc⌐tion of the electric field in the upper diagram is shown explicitly. The surface current density is shown in the lower diagram for $\sum=2$, or $\varepsilon = 27°$. The direction of the current is $(\pi/2\text{-}\varepsilon)$ clockwise of the electric field in the polar cap, and $(\pi/2\text{-}\varepsilon)$ counterclockwise in zone II.

Equipotentials

Convection Velocity
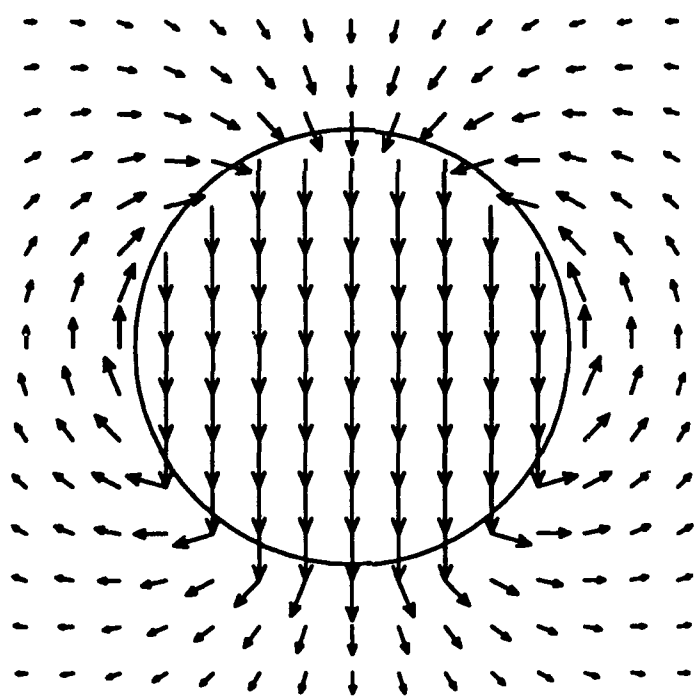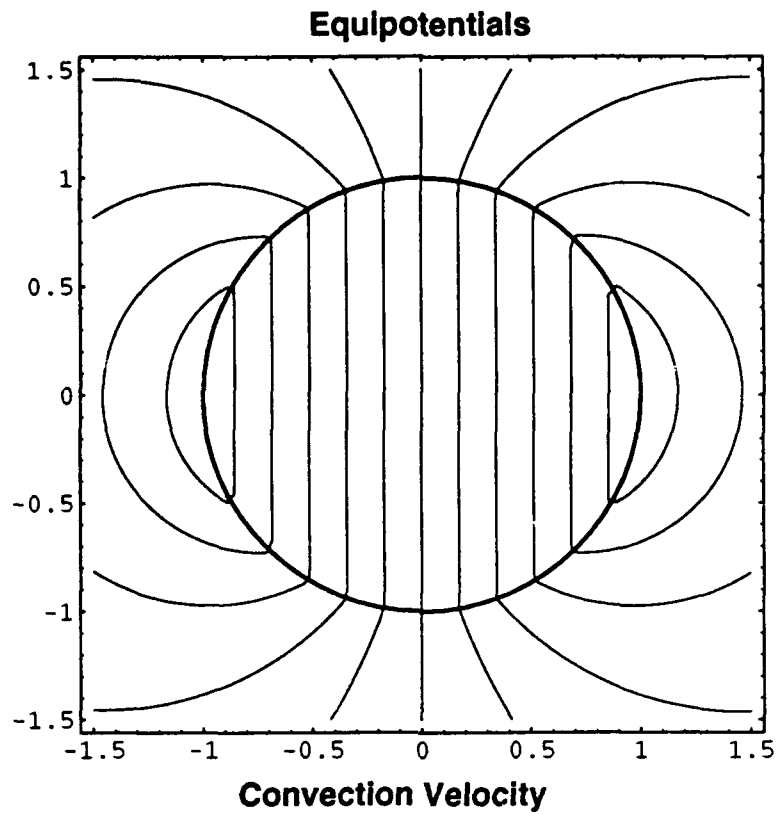
Figure 17. Equipotential lines and the convection pattern for Case A. The diagrams are polar plots of latitude in terms of the variable (y/y_1) versus ϕ(or MLT). The polar cap boundary is the circle of unit radius and midnight is at the bottom of the diagram.

69

The Pedersen currents are parallel to the electric field lines shown in Figure 16, and the Hall currents are antiparallel to the convection pattern shown in Figure 17.

D. The Potential for Region I plus Region II Currents (Case B)

With Region I currents at θ_1 and Region II currents at θ_2 the potential solution at the ionospheric altitude is given by:

Zone I (the polar cap, $\theta \leq \theta_1$):

$$V(\theta, \phi) = V_1 \, (y/y_1)\sin \phi \tag{64}$$

Zone II (the auroral zone, $\theta_1 \leq \theta \leq \theta_2$)

$$V(\theta, \phi) = A(y) \sin \phi + B(y) \sin (\phi + \phi_2) \tag{65}$$

where

$$A(y) = V_1 \left[\frac{y}{y_1} - \left(\frac{y}{y_1} - \frac{y_1}{y} \right) \frac{y_2^2}{y_2^2 - y_1^2} \right] \tag{66}$$

$$B(y) = V_2 \left(\frac{y}{y_1} - \frac{y_1}{y} \right) \frac{y_1 y_2}{y_2^2 - y_1^2} \tag{67}$$

Here $y(\theta) = \tan(\theta/2)$, $y_1 = y(\theta_1)$, and $y_2 = y(\theta_2)$.

Zone III (the subauroral zone, $\theta > \theta_2$)

$$V(\theta, \phi) = V_2(y_2/y) \sin (\phi + \phi_2) \tag{68}$$

The boundary conditions met by the solution are:

$$V = V_1 \sin \phi \text{ at } \theta_1 \tag{69}$$

$$= V_2 \sin (\phi + \phi_2) \text{ at } \theta_2$$

and the potential is continuous at θ_1 and θ_2.

As the equations suggest, the function A in equation (2) couples the zone I and zone II phase shift zero part of the solution, and the function B in (2) couples the zone II and zone III phase shift ϕ_2 part of the solution.

Case B includes a number of new effects not present in Case A. For example, if $V_2 = 0$ then the potential vanishes identically for $\theta \geq \theta_2$; i.e., the region equatorward of the auroral zone has no electric field. This situation highlights the extreme role of the Region II FACs to shield mid latitude regions of electrical effects. As a second example, if $V_2 = V_1 y_2/y_1$ and $\phi_2 = 0$ then Case B reduces to Case A; i.e., the conditions specified require that the Region II FACs vanish and that there is no electrical shielding of low latitudes. The equipotentials for these two examples are shown in Figure 18.

The upper diagram in Figure 18 is the case of complete shielding ($V_2 = 0$). The equipotential lines shown are in units of V_1; in these units the spacing between successive equipotential lines is 0.2. The vertical line across the center of the cap is along the noon-midnight meridian and is at zero potential. The circles are at the polar cap and equatorial auroral boundaries located at θ_1 and θ_2, respectively. The plot is in polar coordinates, where MLT is the azimuth and the radius is (y/y_1). Zero MLT is at the bottom of the figure. (The same format is used in all of the contour plots.)

In the same format, the lower diagram gives the equipotentials for zero shielding and, therefore, no Region II FAC. The equipotentials here are the same as for Case A, shown in Figure 17. In comparing the two cases of complete and zero shielding by the Region II FACs, note the changes in the electric field indicated in the figure by the density of equipotential lines. For complete shielding, the electric field is greatly enhanced about dawn and dusk, and greatly reduced about noon and midnight, compared to the case of zero shielding.

The dramatic affect of the phase ϕ_2 on the equipotentials below the polar cap is shown in Figure 19. In the upper and lower diagrams of Figure 19, the phase ϕ_2 has the values $\pi/3$ and $-\pi/3$, respectively, and $V_2/V_1 = 0.5$. The spacing between the equipotentials is 0.2 in units of V_1. The potential is always positive at θ_1 within the azimuthal interval $[0, \pi]$ and at θ_2 within the azimuthal interval $[-\phi_2, -\phi_2 + \pi]$. The equipotential lines in the polar cap are the same as in Case A, and the equipotentials in zone III are the same as in Case A for $\theta \geq \theta_2$ except for a rigid rotation of the field by the angle ϕ_2; the rotation is clockwise for

Equipotentials, Complete Shielding

Equipotentials, Zero Shielding
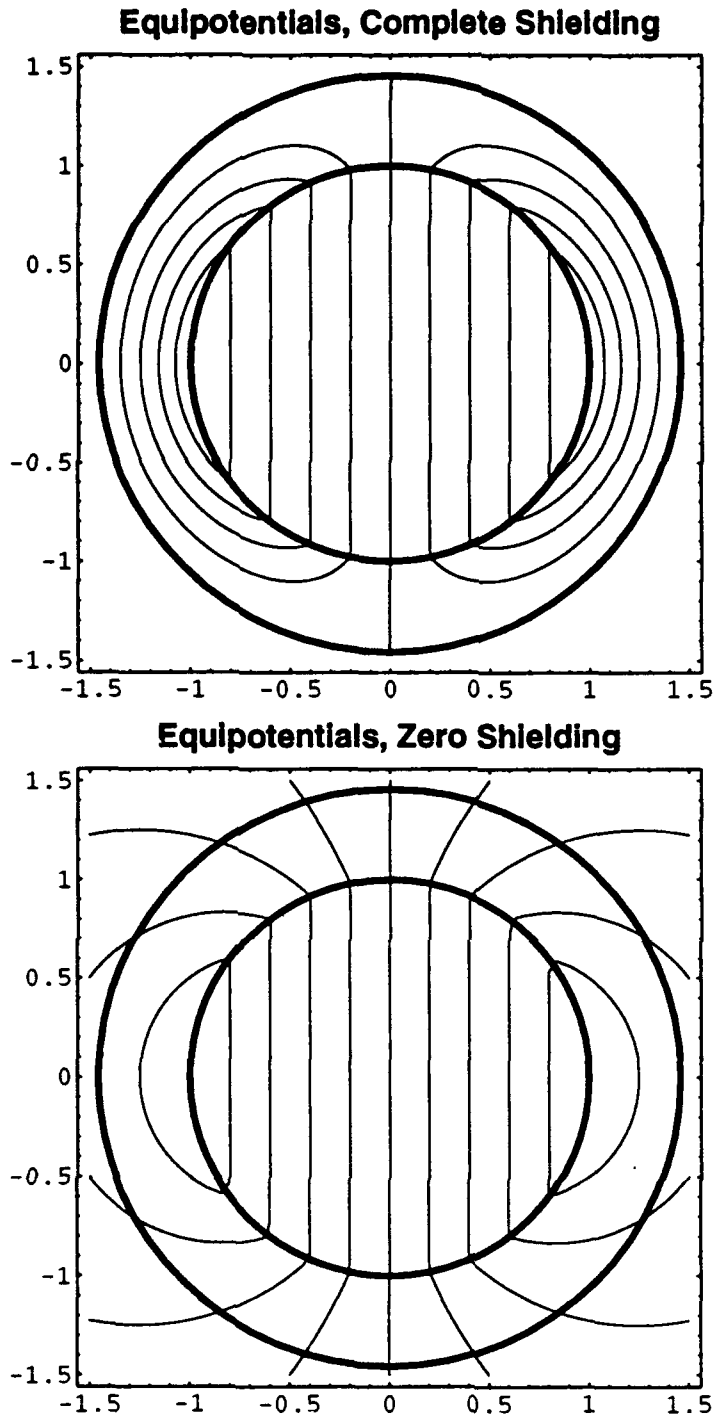
Figure 18. Case B equipotentials. The upper diagram is the case of complete shielding and the lower the case of zero shielding. The inner circle represents the polar cap boundary and the outer the equatorial auroral boundary. In units of V_1, the spacing between equipotential lines is 0.2. The zero potential line crosses the polar cap along the noon-midnight meridian.

72

$\phi_2 > 0$ and counterclockwise for $\phi_2 < 0$. This effect is seen in Figure 19 by comparing the equipotential patterns below the equatorial boundary of the aurora (the outer circle). Because of the rigid rotation of the field below the auroral zone, interesting effects are produced in the auroral zone.

As seen in the upper diagram of Figure 19, equipotential lines that cross the polar cap boundary near the noon-midnight meridian tend to be rotated clockwise by the angle ϕ_2 in progressing from θ_1 to θ_2 across the auroral zone. Equipotential lines at θ_1 for which $V_1 \sin \phi < V_2$ are also rotated in this manner. Convection across the polar cap becomes stretched azimuthally in the auroral zone, with an extended westward flow in the premidnight sector and an extended eastward flow in the prenoon sector. In the region of the stretched flow, the equipotential lines become more dense indicating the presence of an increased electric field (particularly the θ-component) in the auroral zone. This effect is most pronounced in the limit of $V_2 \to 0$, the case of complete shielding shown in Figure 18, and diminishes as V_2 increases. Convection across the flanks of the polar cap exhibit the familiar high latitude, two-cell pattern, with a counterclockwise circulation about the potential high at the polar cap boundary at dawn and a clockwise circulation about the potential low at dusk.

An additional low latitude pair of convection cells forms at the equatorial boundary of the auroral zone at the local potential extrema (a local maximum at $-\phi_2 + \pi/2$, and a local minimum at $-\phi_2 - \pi/2$). The location of the low latitude convection cells depends on the sign of ϕ_2 as seen in Figure 19. As V_2 increases towards V_1, the low latitude pair of convection cells becomes more pronounced and the high latitude pair becomes less pronounced. For $V_2 > V_1$, the high latitude pair essentially dissolves away and only the low latitude pair (now pronounced) remains. This effect is shown in Figure 20 for $\phi_2 = \pi/3$ and $V_2/V_1 = 0.75$ in the upper diagram and $V_2/V_1 = 1.25$ in the lower diagram.

The amplication of the electric field is demonstrated for the case of complete shielding in Figure 21; the plots are of the electric field magnitude in units of $E(0)$ of equation 31. For

73
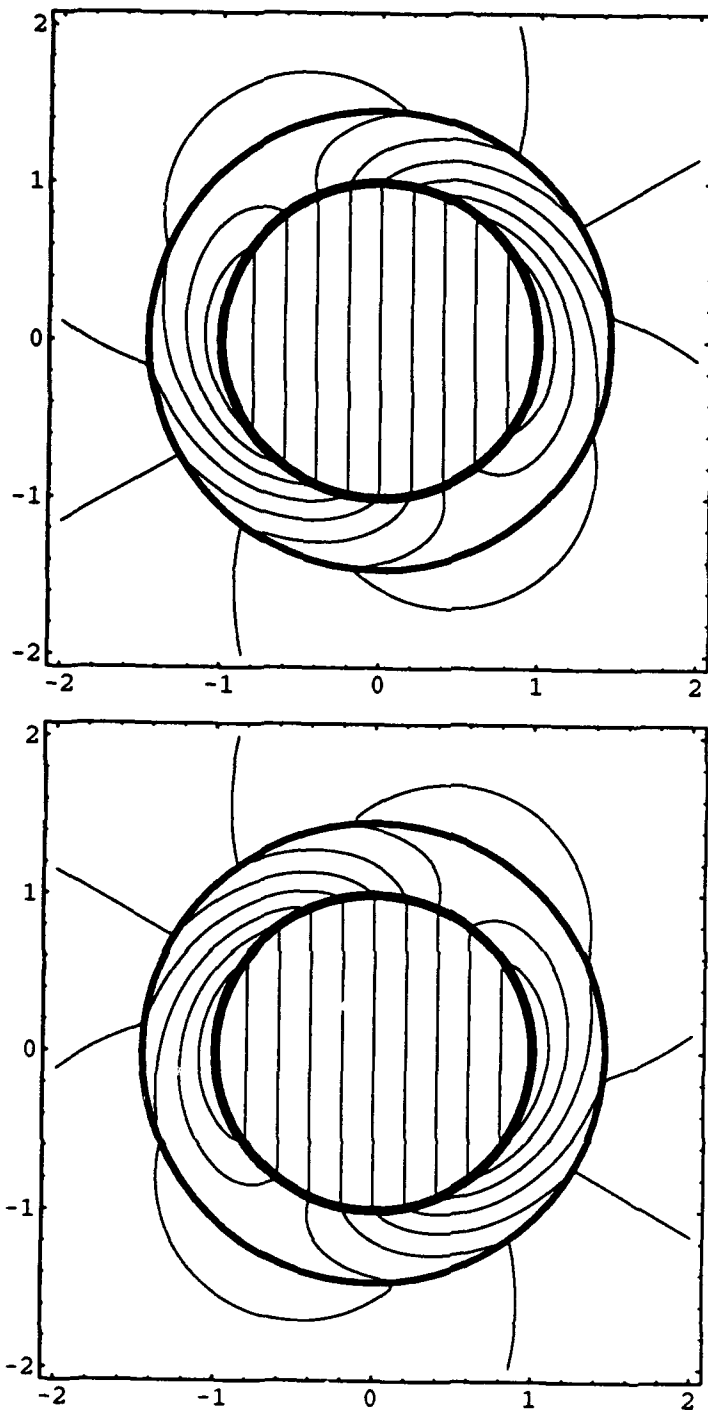
Figure 19. Case B equipotentials for $V_2/V_1 = 0.5$. In the upper diagram, $\varphi_2=\pi/3$ and in the lower diagram $\varphi_2 = -\pi/3$. The same scale, spacing, and format are used as in Figure 18.

74
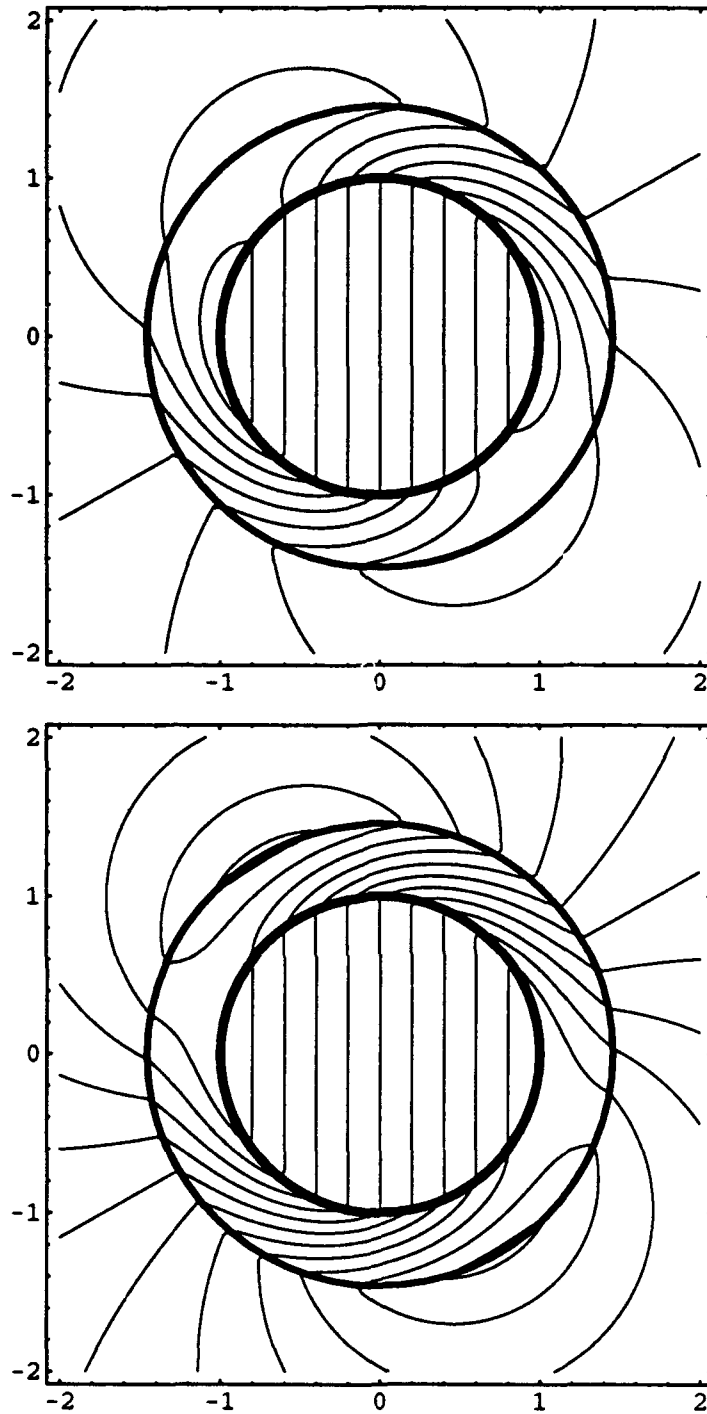
Figure 20. Case B for an enhanced auroral potential. Equipotentials are shown for $\varphi_2 = \pi/3$. In the upper diagram, $V_2/V_1 = 0.75$ and in the lower diagram $V_2/V_1 = 1.25$. The same format and conditions are used as in Figure 18.

complete shielding, $E=0$ for $y \geq y_2$ where y_2 is the equatorial "radius" of the auroral boundary. In the upper diagram of Figure 21, the level (or isointensity) curves of E are shown in the usual polar plot. The electric field is uniform in the polar cap. In the auroral zone, the intensity is largest in the dawn and dusk sectors and weakest in the midnight and noon sectors. The intensity is shown along the noon-midnight meridian in the lower-left line diagram, and along the dawn-dusk meridian in the lower right line diagram. The maximum amplification of the electric field is at 06:00 and 18:00 MLT by a factor of 2.85.

Isointensity plots of the electric field are of special interest because the same curves give lines of constant convection speed, lines of constant total current, and contours of constant Joule heating. These statements follow from equations 14 and 56, and the convection speed v_c given by

$$v_c = c \ E(\theta,\phi)/B \qquad (70)$$

which is gotten directly from equation 10. Thus, in the case of complete shielding, the electric field is largest, the convection is fastest, the Joule heat greatest, and the currents most intense at dawn and dusk in the auroral zone; and the electric field is smallest, the convection is slowest, the Joule heat smallest, and the current weakest at noon and midnight in the auroral zone. The electric field is largest at the poleward boundary of the auroral zone and decreases monotonically towards the equatorial boundary.

With current conservation applying at both θ_1 and θ_2, the impact of the FACs on the auroral dynamics is far more complex than in Case A. At θ_1, current balance requires

$$\kappa_1 \sin \delta_1 = -c - b \ v_2 \sin \phi_2 \qquad (71)$$

$$\kappa_1 \cos \delta_1 = a + b \ v_2 \cos \phi_2 \qquad (72)$$

while at θ_2

$$\kappa_2 \sin \delta_2 = -v_2(c \cos \phi_2 + a \sin \phi_2) \qquad (73)$$

$$\kappa_2 \cos \delta_2 = v_2(c \sin \phi_2 - a \cos \phi_2) + b \qquad (74)$$

E(magnitude), Complete Shielding
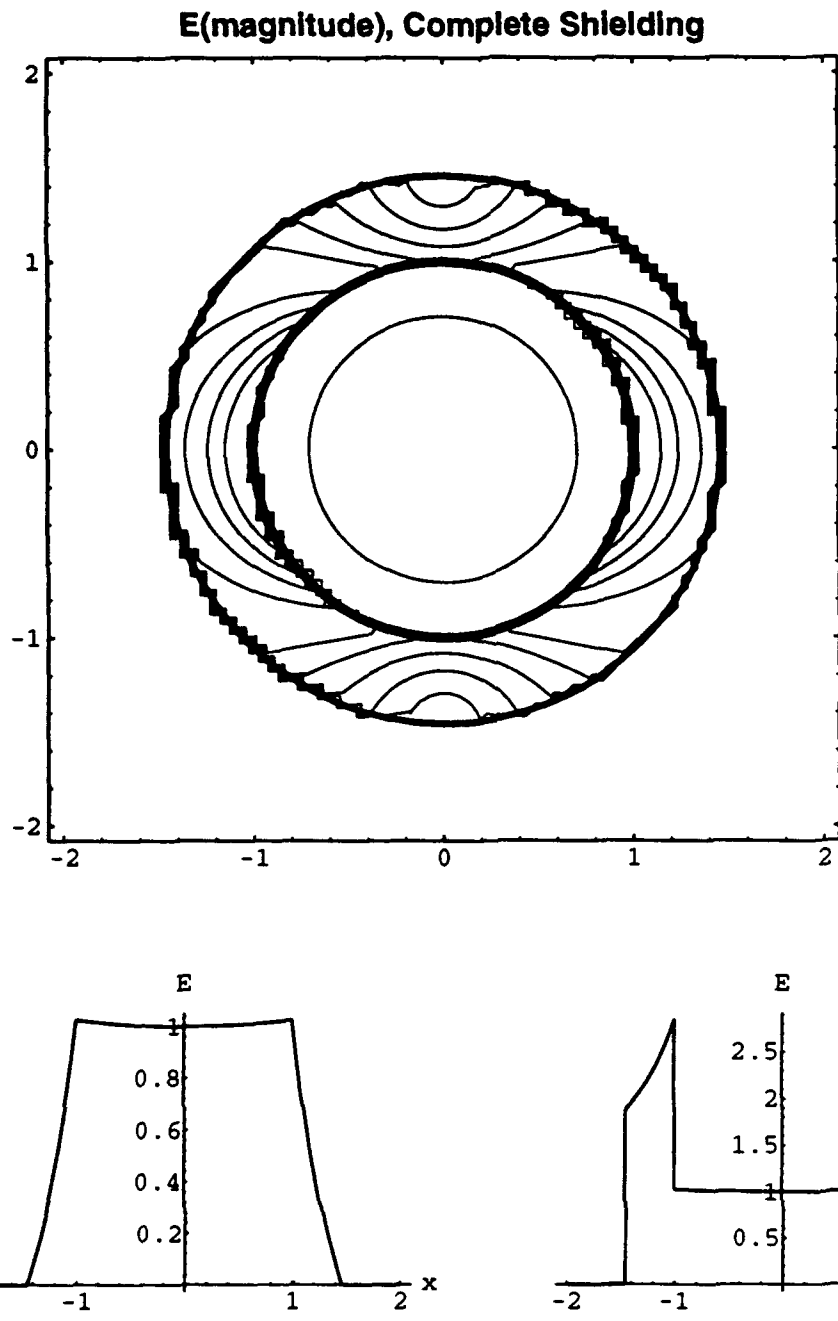
Figure 21. The Case B electric field magnitude for complete shielding. The magnitude of the electric field is shown in units of E (0). The dense circles are at the polar cap boundary θ_1, and the equatorial boundary θ_2. In the isointensity contour plot of the upper diagram, the single contour in the polar cap has the value $(1 + y_1^2/2) = 1.0125$. The other contours, in progressing from the weak field in the auroral zone along the noon-midnight meridian towards the strong dawn-dusk field, have values (0.25, 0.50, 0.75, 1.01, 1.25, 1.75, 2.00, 2.20, 2.40). At the bottom, the value of E is shown along the midnight-noon meridian (the x-axis) and the dawn-dusk meridian (the y-axis). The same format is used as in previous contour plots.

where

$$\kappa_1 = I_1 \sin \theta_1 / \Sigma_p^{II} V_1 \tag{75}$$

$$\kappa_2 = I_2 \sin \theta_2 / \Sigma_p^{II} V_1 \tag{76}$$

$$v_2 = V_2 / V_1 \tag{77}$$

$$a = q + (s^2 - 1)/(s^2 + 1) \tag{78}$$

$$b = 2s/(s^2 + 1) \tag{79}$$

$$c = (1 - q) \Sigma \tag{80}$$

$$s = y_2/y_1 \tag{81}$$

The variables κ_1 and κ_2 refer to the Region 1 and Region 2 FAC intensities, respectively, and v_2 is the potential parameter.

The analysis will proceed using the potential at θ_1 and the Region 2 FAC at θ_2 as given (or independent) variables. The solutions above may then be cast in the form of triangle relationships. Introducing the variables

$$K_1 = \kappa_1 / \kappa_{10} \tag{82}$$

$$K_2 = \kappa_2 / \kappa_{20} \tag{83}$$

$$v = v_2 \, b / \kappa_{10} \equiv v_2 / v_0 \tag{84}$$

where

$$\kappa_{10} = (a^2 + c^2 - b^2)/\sqrt{a^2 + c^2} \tag{85}$$

$$\kappa_{20} = (a^2 + c^2 - b^2)/b \tag{86}$$

and

$$\alpha = \arctan (c/a) \tag{87}$$

$$L = (a^2 + c^2)/(a^2 + c^2 - b^2) \tag{88}$$

equations 71-74 become:

$$K_1 \sin (\delta_1 + \alpha) = K_2 \sin \delta_2 \tag{89}$$

$$K_1 \cos (\delta_1 + \alpha) = 1 + K_2 \cos \delta_2 \tag{90}$$

and

$$v \sin (\phi_2 + \alpha) = - K_2 \sin \delta_2 \qquad (91)$$

$$v \cos (\phi_2 + \alpha) = L\text{-}1\text{-}K_2 \cos \delta_2 \qquad (92)$$

Equations 89-92 are suitable to express the solutions in the functional form

$$K_1(K_2, \delta_2) \, , \, \delta_1(K_2, \delta_2) \qquad (93)$$

$$v(K_2, \delta_2) \, , \, \phi_2(K_2, \delta_2) \qquad (94)$$

In 93, the Region I FACs are given in terms of the Region II FACs. In 94, the potential at θ_2 is given in terms of the Region II FAC. The potential at θ_1, q, Σ, and s also parameterize the solutions.

A symmetry property of the solution is that K_1 and v are independent of the sign of δ_2. In addition, the phases satisfy

$$\delta_1(K_2, \delta_2) + \delta_1(K_2, \text{-}\delta_2) + 2\alpha = 0 \qquad (95)$$

$$\phi_2(K_2, \delta_2) + \phi_2(K_2, \text{-}\delta_2) + 2\alpha = 0 \qquad (96)$$

i.e., $(\delta_1 + \alpha)$ and $(\phi_2 + \alpha)$ are odd functions of δ_2.

The Region I FACs and the potential at θ_2 are shown in Figures 22 and 23 for the parameter choices q = 0.5 and Σ = 2. For these values, the parameters in equations 84 to 88 are given by:

$$\kappa_{10} = 1.47 \, , \, \kappa_{20} = 1.94 \, , \, v_0 = 0.566$$

$$\alpha = 17° \, , \, L = 2.34$$

The Region I FAC is shown in Fiqure 22 as a function of K_2 with δ_2 as the parameter labeling the curves in 30 degree increments from 0° to 180°; the magnitude K_1 is in the upper diagram and the phase δ_1 in degrees in the lower diagram. The phase δ_1 varies from -α (for δ_2 = 0; or for δ_2 = π with $K_2 < 1$) to π - α (for δ_2 = π with $K_2 > 1$). At K_2=0, the Region I FAC has the magnitude K_2=1 and the phase δ_2 = -α = -17°. At fixed K_2, the intensity K_1 decreases monotonically as δ_2 increases through positive values, and the phase δ_1 increases monotonically as δ_2 increases.
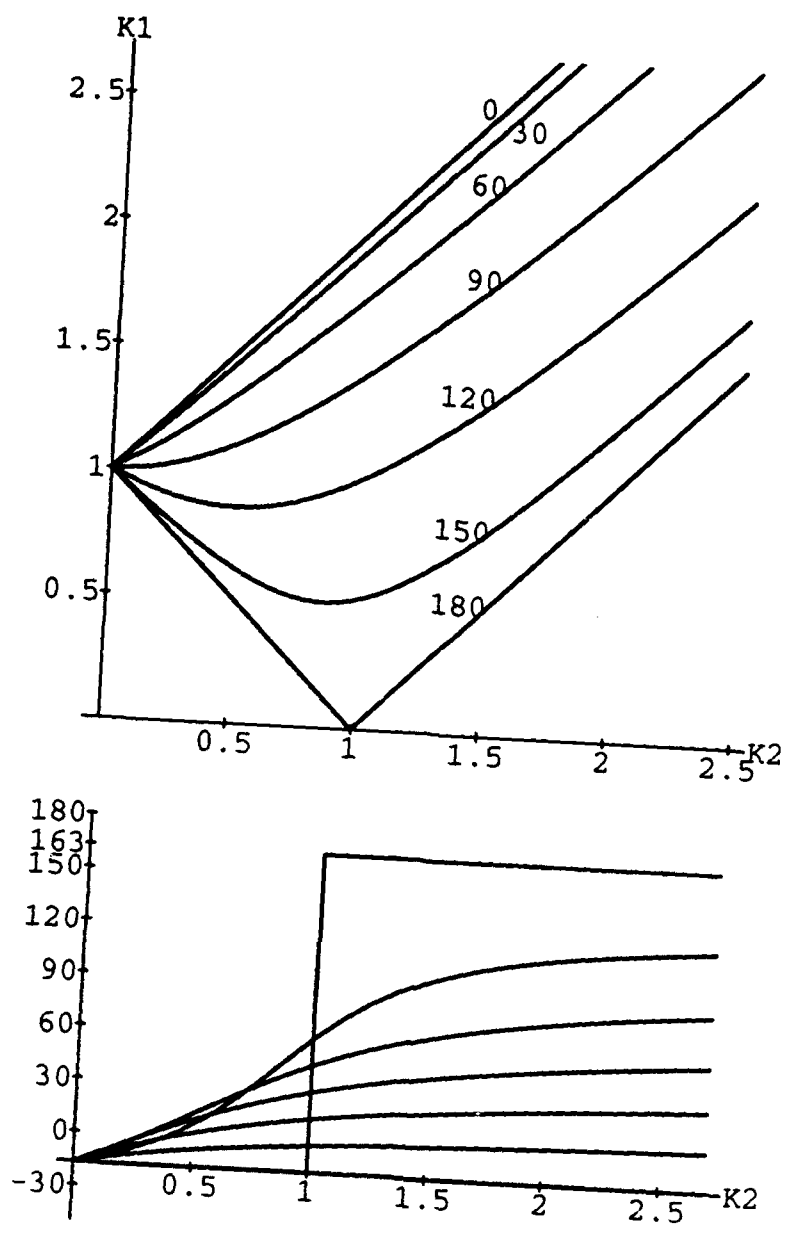
Figure 22. Region I FACs determined from Region II FACs. The upper diagram gives the intensity K_1 and the lower diagram the phase δ_1 as a function of the intensity K_2. The phase δ_2 parameterizes the curves in 30° increments from 0° to 180°. For δ_1 in the lower diagram, the y-intercept occurs at $-\alpha = -17^\circ$ and the maximum value of δ_1 is $180^\circ - \alpha = 163^\circ$.
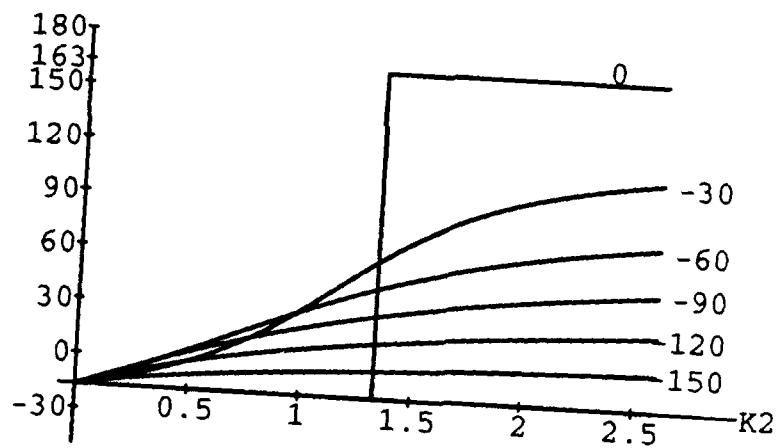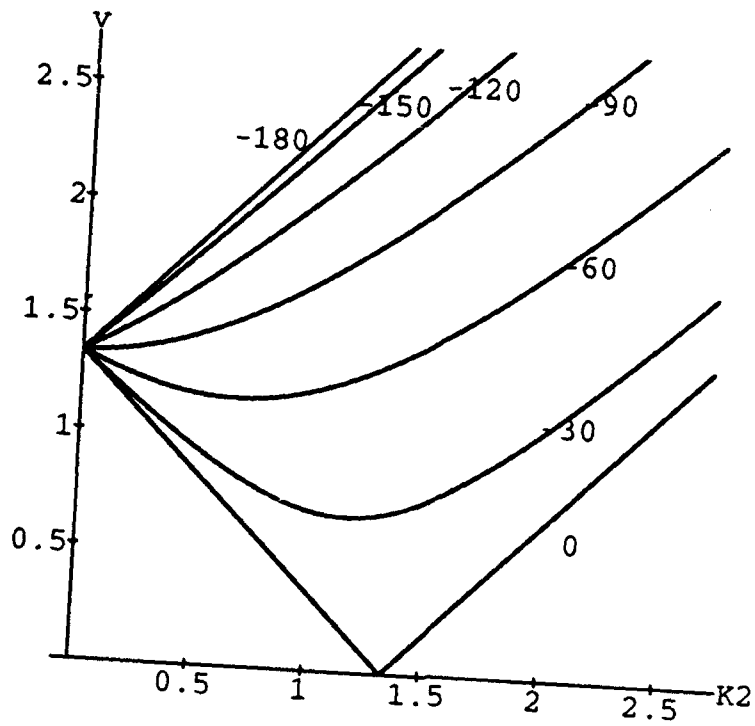
Figure 23. Potential at θ_2 determined from Region II FACs. The upper diagram gives v vs. K_2 and the lower φ_2 vs. K_2. In both diagrams, the value of δ_2 that parameterizes the curves is shown.

81

The potential at θ_2 is shown in Figure 23 in a similar format to that of Figure 22. The potential parameter ν and its phase ϕ_2 are shown for negative values of δ_2. For any δ_2 at $K_2=0$, the potential at θ_2 has the magnitude $\nu=L-1=1.34$ and phase $\phi_2=-\alpha=-17°$. Another extreme condition occurs for $K_2=L-1$ and $\delta_2=0$, which requires the potential at θ_2 to vanish: $\nu=0$. This is the case of complete shielding shown in Figure 18.

The special case of $K_2=0$ is of interest because it corresponds to zero Region II FACs. Yet, $K_2=0$ requires the Region I FAC to have the magnitude and phase given by

$$K_1=1 \text{ and } \delta_1 = -\alpha \qquad (97)$$

and the potential at θ_2 to have magnitude and phase given by

$$\nu=L-1 \text{ and } \phi_2 = -\alpha \qquad (98)$$

Thus, even in the absence of Region II FACs, the Region I FACs and the potential are changed from Case A in the auroral (zone II) and sub auroral (zone III) zones. The changes are induced by the conductivity enhancement of the auroral zone. The changes in the magnitudes and phases between Case A and Case B produced by the conductivity enhancement of the auroral zone are demonstrated in Tables 16 and 17. In Table 16 the parameters $q=1/2$ and $\Sigma=2$ are used, and in Table 17 the conductivities of the auroral zone are enhanced further to the values $q=0.1$ and $\Sigma=3.5$.

Table 16. Region I FAC and Potential at θ_2: $q=1/2$, $\Sigma=2$

	δ_1	κ_1	ϕ_2	V_2/V_1
Case A	-33.7	1.80	0	0.69
Case B	-17	1.47	-17	0.76

The angles δ_1 and ϕ_1 are in degrees. Tabulated values are for the condition of zero Region II FAC, $K_2=0$.

Table 17. Region I FAC and Potential at θ_2: q=0.1, Σ=3.5

	δ_1	κ_1	ϕ_2	V_2/V_1
Case A	-70.8	3.34	0	0.69
Case B	-47.6	2.69	-47.6	0.61

The angles δ_1 and ϕ_2 are in degrees. Tabulated values are for the case K_2=0.

The case of complete shielding (v=0) fixes the values of the Region I and Region II FACs to the values

$$K_2 = L\text{-}1, \ \delta_2 = 0$$

$$K_1 = L \, , \ \delta_1 = \text{-}\alpha$$

The ratio of the total Region I current into the ionosphere to the total Region II current into the ionosphere is given, in general, by:

$$r = \kappa_1/\kappa_2$$

For the case of complete shielding the ratio is

$$r = L/(L\text{-}1) = (a^2 + c^2)/b^2$$

For q=1/2, Σ = 2 the ratio with complete shielding is r = 1.32; for q=0.1, Σ = 3.5, the ratio is 1.65. The role of the Region II currents (the shielding currents) in the case of complete shielding is to insure current continuity by matching the Pederson component of the auroral zone current at θ_2. With complete shielding, the east-west component of the electric field and the Hall current vanish at θ_2. Complete shielding can be accomplished with the total Region II FAC into the ionosphere being about 0.6 to 0.8 of the total Region I input.

Empirically, statistical evidence indicates that the phase δ_2 of the Region II FAC is typically near zero and the total Region II current is usually less than or about the same size as the Region I current. The general solutions obtained above are therefore displayed in an

expanded form about this parameter range of primary interest. In Figure 24, K_1 and δ_1 are shown for δ_2 between $-30°$ and $+30°$ (i.e., from 22:00 MLT to 02:00 MLT); K_2 parameterizes the curves. K_1 is essentially constant, independent of δ_2; since it falls near to the $\delta_2=0$ limit curve of Figure 22 for which $K_1=1+K_2$. δ_1 increases monotonically with δ_2, approximately linearly for $K_2<1$ and with larger slope for larger K_2.

In Figure 25, the potential variables are shown. The amplitude v is essentially independent of δ_2 for $K_2 \leq 1/2$. For larger K_2, v exhibits a minimum at $\delta_2=0$ that deepens with increasing K_2 as v approaches the limit of complete shielding. The phase ϕ_2 decreases monotonically with δ_2. For small K_2, ϕ_2 varies essentially linearly with δ_2 for small K_2 and with a more structured dependence as K_2 increases.

The physical behavior of the solutions is as follows. As δ_2 increases, the Region II current configuration rotates clockwise. Similarly, as δ_1 or ϕ_2 increases, the Region I current configuration rotates clockwise.

For fixed K_2, Figures 24 and 25 show that as δ_2 increases, δ_1 increases and ϕ_2 decreases. Thus, if the Region II current configuration rotates clockwise with fixed intensity, the Region I currents also rotate clockwise and the potential configuration at θ_2 rotates counterclockwise. The intensity of the Region I currents remains essentially constant in the rotation, though the potential v may change.

For fixed δ_2, as the intensity K_2 of the Region II FAC increases, the Region I FAC increases in intensity and rotates clockwise if $\delta_2 > 0$, and counterclockwise if $\delta_2 < 0$; if $\delta_2=0$, there is no rotation and $\delta_1 = -17°$. The potential v decreases as K_2 increases and rotates counterclockwise if $\delta_2 > 0$ and clockwise if $\delta_2 < 0$; if $\delta_2=0$, there is no rotation and $\phi_2 = -17°$.
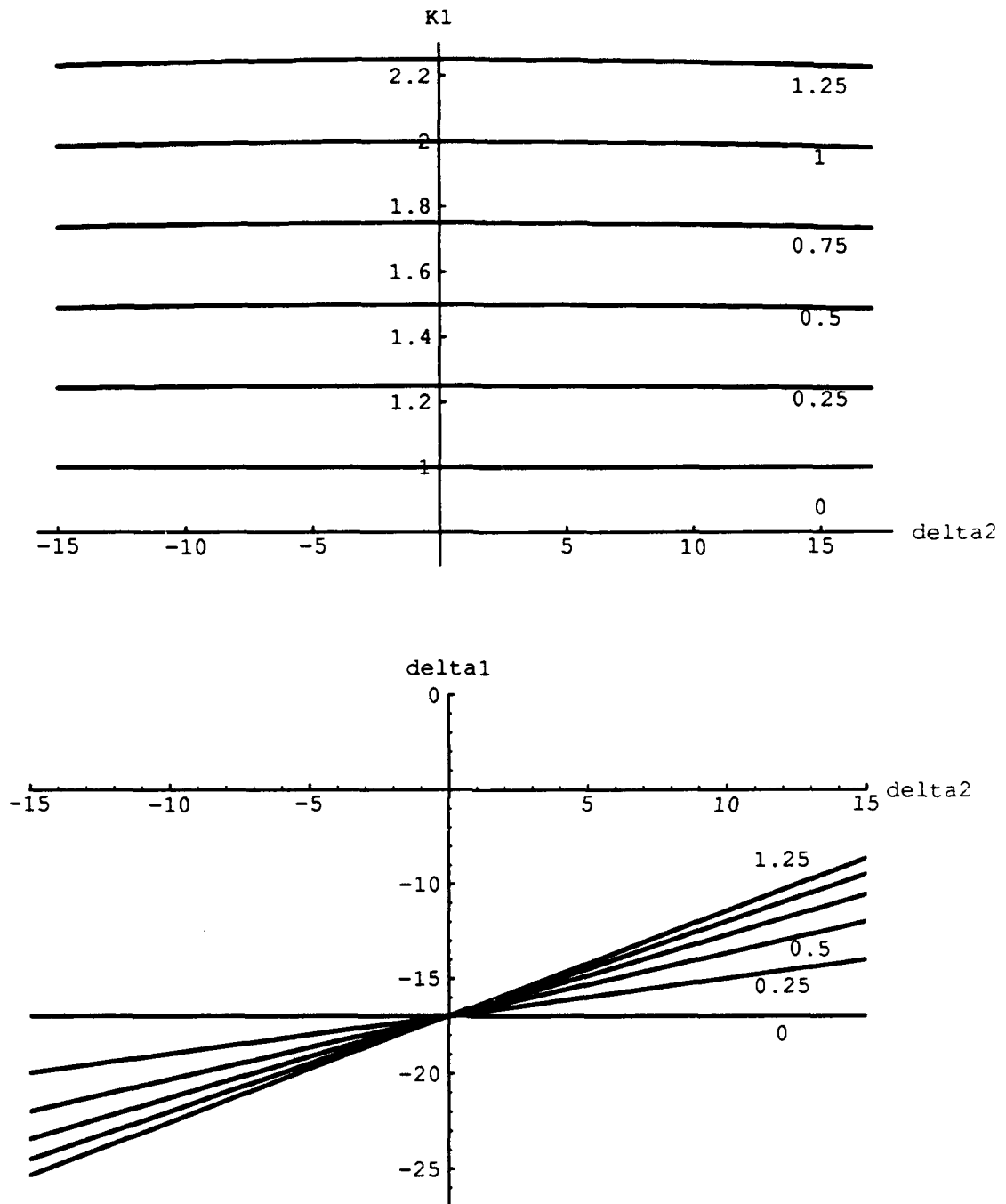
Figure 24. Region I FAC vs. δ_2. The Region I FAC magnitude parameter K_1 is plotted in the upper diagram and the phase δ_1 in the lower diagram. The abscissa is the phase δ_2 of the Region II FAC. The magnitude parameter K_2 of the Region II FAC parameterizes the plots.

85
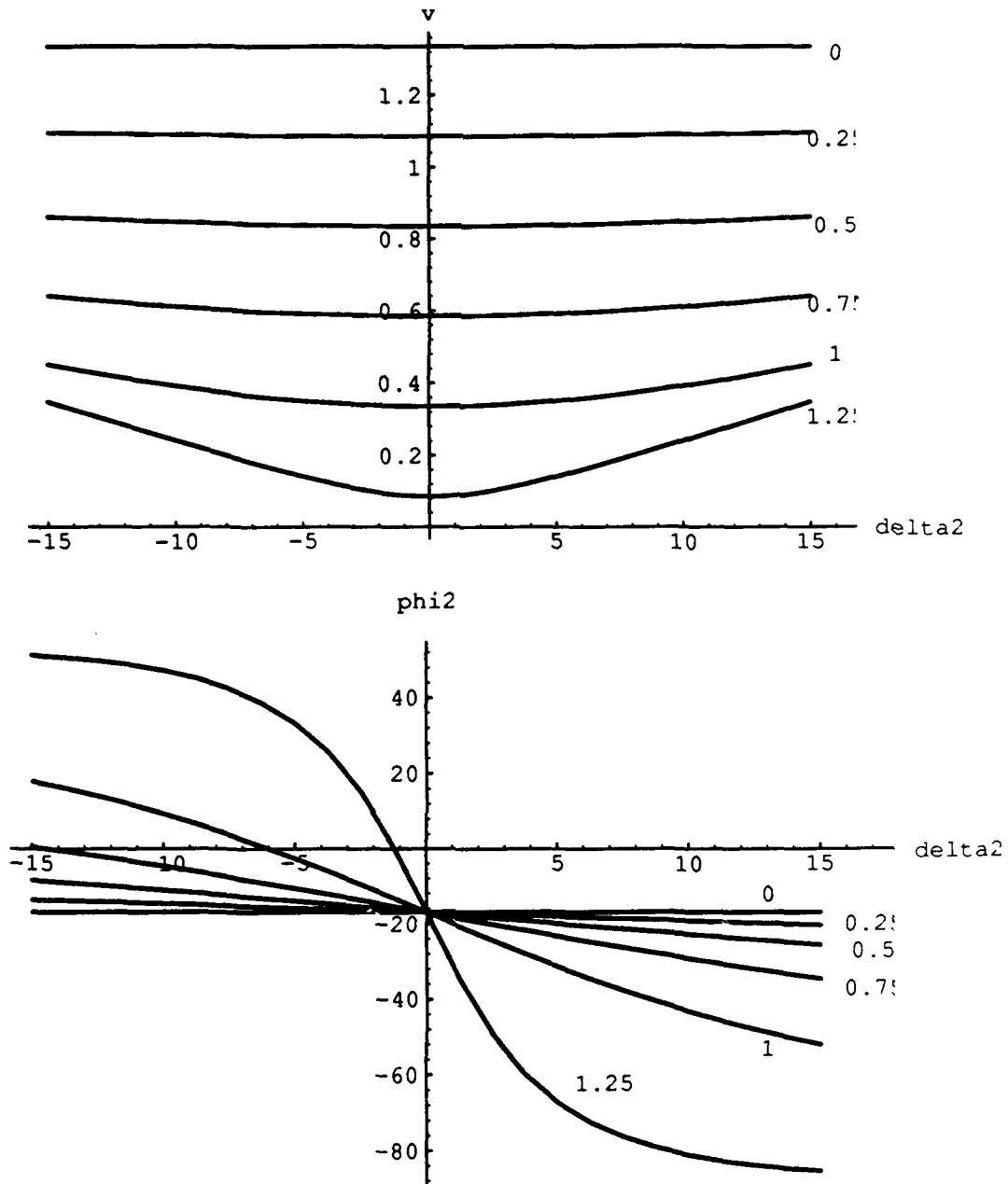
Figure 25. Potential at θ_2 vs. δ_2. The potential magnitude variable ν is plotted in the upper diagram and the phase φ_2 in the lower diagram. The abscissa is the phase δ_2 of the Region II FAC. The magnitude K_2 of the Region II FAC parameterizes the plots.

The ionospheric current density is expressed in dimensionless form by the vector **IK** where

$$\mathbf{IK} = \mathbf{J}/\Sigma_p^{II} \, E(0) \tag{103}$$

Here **J** is the current density in equation 8, Σ_p^{II} is the Pedersen conductivity in the auroral zone, and $E(0)$ is the magnitude of the electric field at the pole given in equation 31.

In the polar cap, the magnitude, θ-component, and ϕ-component of the current density are given by (see also equations 34 to 38)

$$IK_1 = q_1 \sqrt{1+\Sigma^2} \, (1+y^2) \tag{104}$$

$$IK_{1\theta} = - IK_1 \cos(\phi-\varepsilon) \tag{105}$$

$$IK_{1\phi} = IK_1 \sin(\phi-\varepsilon) \tag{106}$$

The variable q_1 (denoted q in Case A) is given by

$$q_1 = \Sigma_p^{I} / \Sigma_p^{II} \tag{107}$$

and ε is given in equation 36. The polar cap current is the same as in Case A. The North-South (N-S) component of the current is $-IK_{1\theta}$, and the East-West (E-W) component is $IK_{1\phi}$. The total current and its N-S, and E-W components at the polar cap boundary $y = y_1$ are shown in Figure 26 as a function of MLT. In Figure 26 the values $q_1 = 0.5$ and $\Sigma = 2$ (so that $\varepsilon = 27°$) are used. The polar cap current at the boundary is shown in the upper diagram of Figure 26. The total polar cap current is seen to be constant in MLT while the N-S and E-W components show the relative phase shift of $90°$. At the polar cap boundary, the current mainly feeds into the polar cap around the post midnight sector and leaves the polar cap in the post noon sector. The extrema of the N-S component of the polar cap current are determined by ε, which corresponds to 1.7 hours (MLT) in Figure 26; the N-S component is maximum at $\phi = \varepsilon$ and minimum at $\phi = \varepsilon + \pi$.

The current in the sub auroral zone (zone III) is given by IK_3, and

$$IK_3 = v_2 q_3 \sqrt{1+\Sigma^2} \, y_1 \, y_2 \, (1+1/y^2) \tag{108}$$

Polar Cap Current at y1

Auroral Current at y1
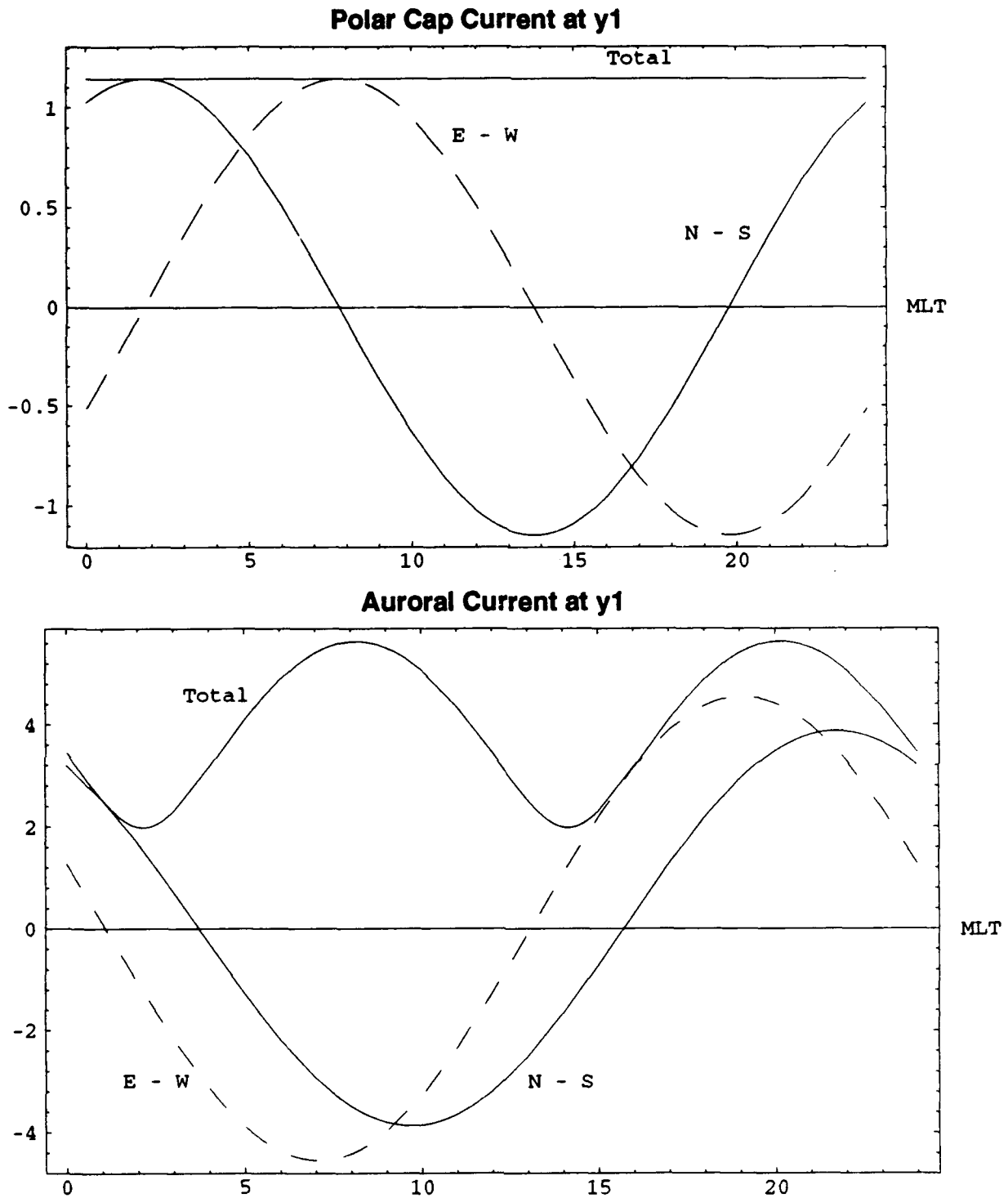
Figure 26. Current at the polar cap boundary θ_1. As labeled, the total, North-South (N-S), and East-West (E-W) components of the polar cap current are shown at the polar cap boundary (y_1 or θ_1). Conductivity values of $q = 0.5$ and $\Sigma=2$ are used in the plots. The E-W component is the dashed curve. The upper diagram gives the currents at θ_1 in the polar cap. The lower diagram gives the auroral currents at the polar cap boundary. Note the ordinate scale change in the two diagrams. The total auroral current is far more intense at the polar cap boundary.

$$IK_{3\theta} = -IK_3 \cos (\phi + \phi_2 + \epsilon) \tag{109}$$

$$IK_{3\phi} = -IK_3 \sin (\phi + \phi_2 + \epsilon) \tag{110}$$

Here

$$q_3 = \Sigma_p^{III}/\Sigma_p^{II} \tag{111}$$

and v_2 and ϕ_2 are the potential parameters at θ_2 given in equations 69 and 77. The current flows in a dipole like pattern in the subauroral zone with the axis of symmetry at the angle $(\phi_2 + 2\epsilon)$ clockwise of the polar cap current direction. It follows from equations 109 and 110 that the θ and ϕ components of the subauroral current are also 90 degrees out of phase. The subauroral boundary current is exactly northward at $\phi = - (\phi_2 + \epsilon)$; exactly westward at $\phi = - (\phi_2 + \epsilon) + \pi/2$; exactly southward at $\phi = - (\phi_2 + \epsilon) + \pi$; and exactly eastward at $\phi = - (\phi_2 + \epsilon + \pi/2)$. The total, N-S, and E-W components of the current at the equatorial auroral boundary are shown in Figure 27. The auroral current is shown in the upper diagram of Figure 27 and the sub auroral current is shown in the lower diagram for the parameter choices $q_3 = 0.5$, $\Sigma = 2$, $v = 0.5$, and $\phi_2 = \pi/3$. The total current at y_2 in the subauroral zone is seen to be constant and distributed between the N-S and E-W components which are 90° out of phase. The current is northwards (i.e., into the auroral zone) in the dusk sector and southwards (i.e., out of the auroral zone) in the dawn sector for the parameters chosen. The phase difference between peak northward directed current at y_2 in the subauroral zone and peak northward directed current at y_1 in the polar cap is $(\phi_2 + 2\epsilon)$; for the parameters used in Figures 26 and 27, this phase difference is $(30° + 52°) = 82°$.

The auroral zone current, calculated in a similar manner, is given by a lengthy expression that is not recorded. The total auroral zone current and its N-S and E-W components are shown in Figure 26 at the polar cap boundary θ_1, and in Figure 27 at the auroral equatorward boundary θ_2, for the same parameter choices $\Sigma = 2$, $v = 1/2$, and $\phi_2 = \pi/3$. The striking results include the significant amplification of the ionospheric current
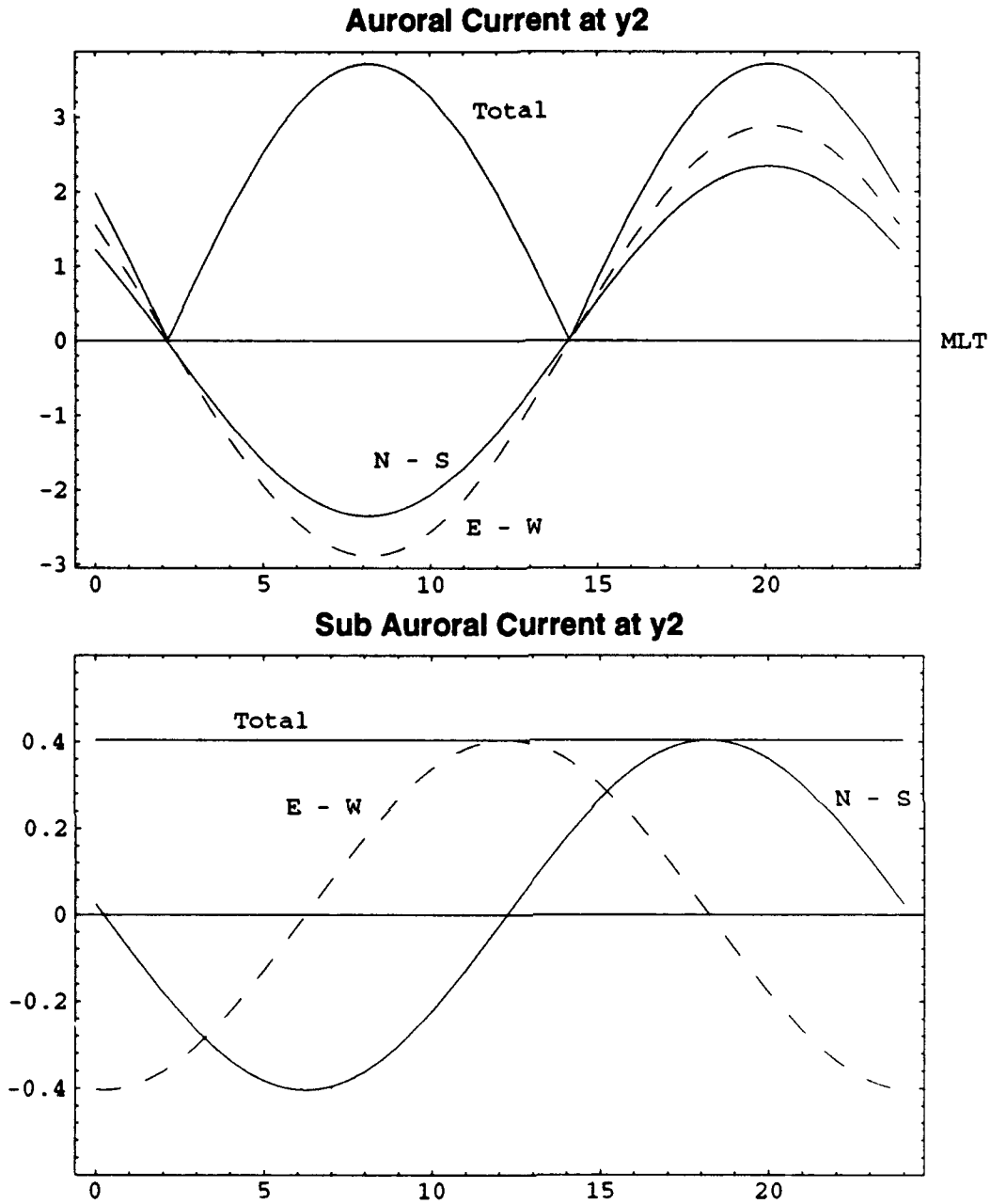
Figure 27. Currents at the auroral equatorial boundary. The same format and parameter values are used as in Figure 15. The upper diagram gives the auroral current at the boundary, y_2 or θ_2, and the lower diagram gives the sub-auroral current at the same boundary.

at the auroral boundaries and the evolutionary phase change in the auroral zone in going from θ_1 to θ_2.

Unlike its counterparts in the polar cap and the sub auroral zone, the total auroral current at the auroral boundaries is not constant in MLT. The total auroral current is enhanced at both auroral boundaries, as shown in Figure 28. The maximum amplification of the total current is about $(5.63/1.15) = 4.9$ at the poleward boundary and $(3.72/0.406) = 9.2$ at the equatorward boundary for the parameters of Figure 28. The amplification is larger at the equatorward boundary, but the currents are larger at the poleward boundary. At each latitude the total auroral current varies sinusoidally with a steep minimum developing in going from the poleward to the equatorward boundary, as well as a monotonic decrease in the current extrema. The total auroral current is shown in two perspectives in Figure 29 which is a three dimensional plot of the amplitude of the total current versus latitude and MLT. The latitude is in terms of the variable $y(\theta)/y(\theta_1)$, with $\theta_1 = 18°$ for the poleward boundary and $\theta_2 = 26°$ for the equatorward boundary. In Figure 30, the northward and eastward components of the auroral current are shown in similar 3-D plots. In progressing towards the equatorward boundary, the phase difference of the components gradually decreases. The deep minimum of the total auroral current occurs in the vicinity of the nearly common node of the eastward and northward components at the equatorward boundary.

Values of the currents at the auroral boundaries are given in Table 4 for the parameter choices of Figures 26-29. Current amplitudes and phases in MLT are given in the table for the eastward current (E), northward current (N), and the total current (T). Whereas the eastward and northward currents are of equal amplitude and 6 hours out of phase (i.e., 90°) both in the polar cap and in the sub auroral zone, this is not the case in the auroral zone. In the auroral zone, the eastward current has a larger amplitude than the northward current. And the phase of the eastward auroral current leads the northward current by 2.6 hours (or 39.0°)

Total Currents at Polar Cap Boundary,y1

Total Currents at Equatorial Auroral Boundary,y2
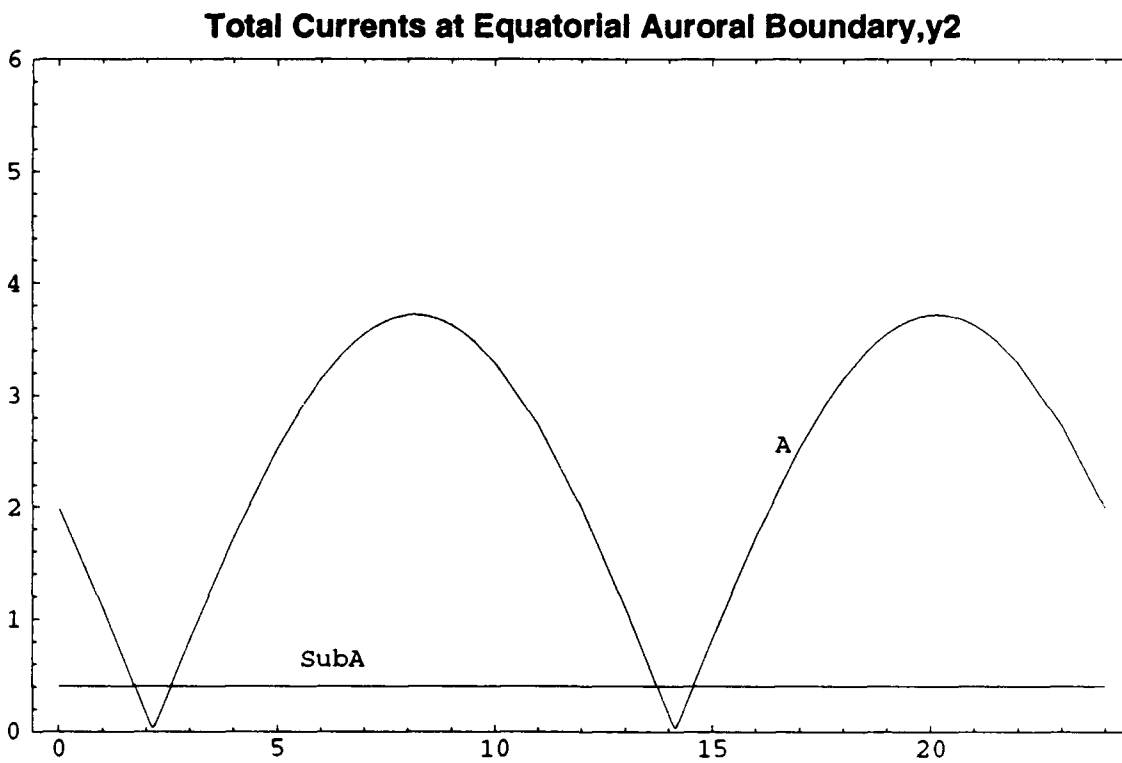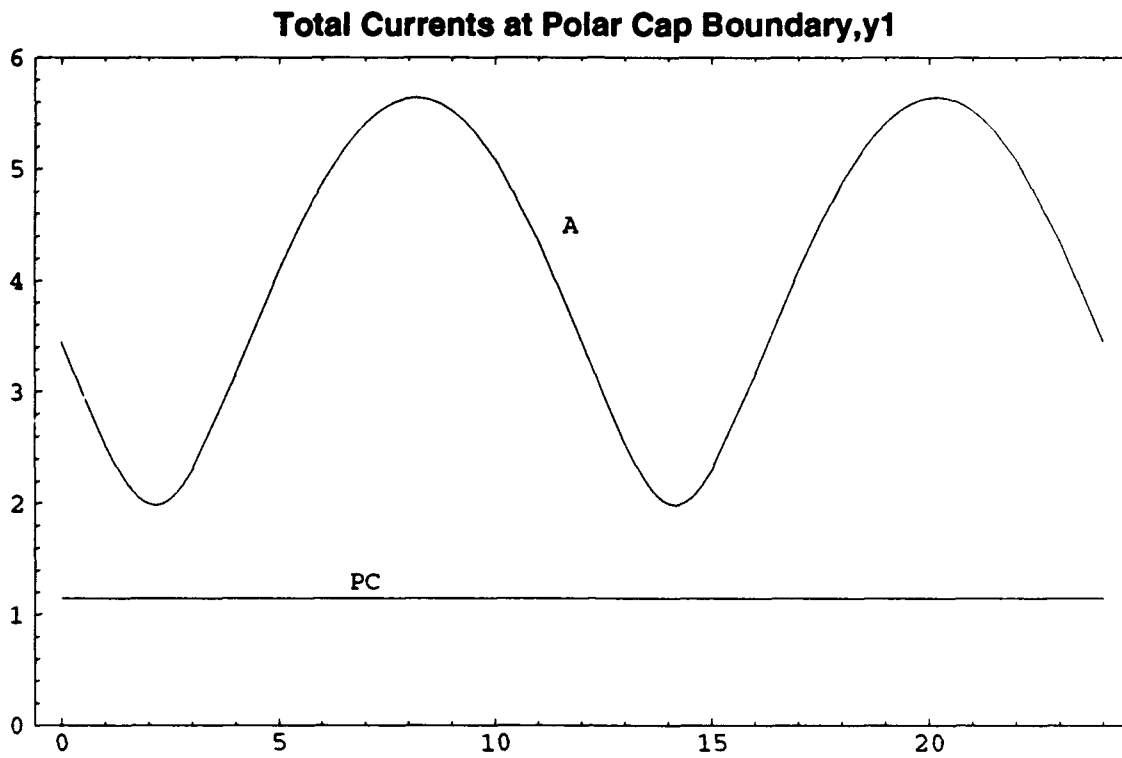
Figure 28. Total currents at the auroral boundaries. In the upper diagram the total currents at the polar cap boundary are given. In the lower diagram, the total curents at the equatorward auroral boundary are given. The same parameters as in Figures 26-27 are used.
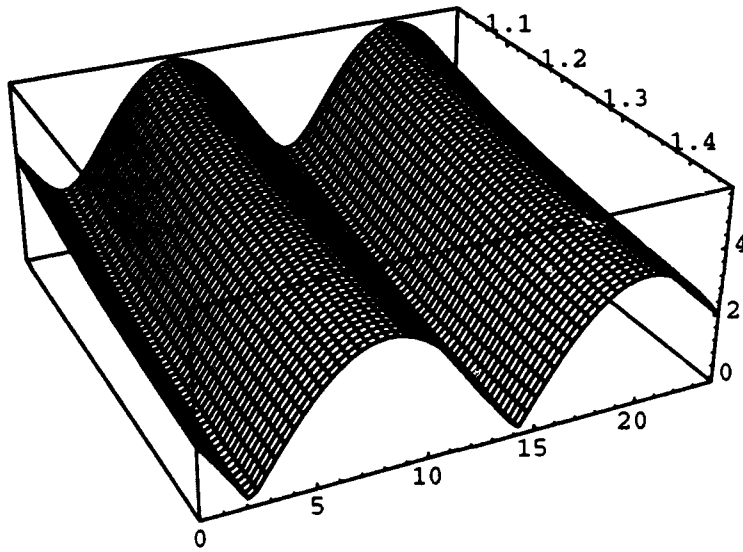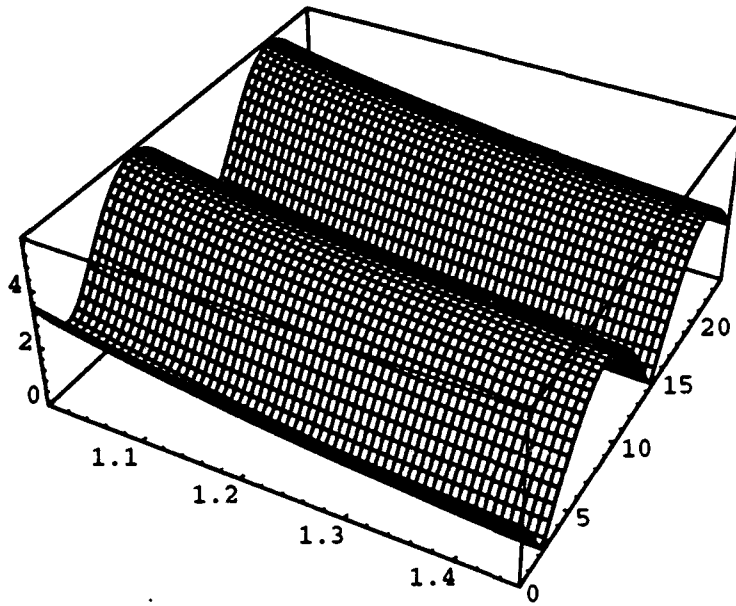
Figure 29. The total auroral current. 3-D plots are of the total current in two perspectives. Latitude is represented by $y(\theta)/y_1$ which extends from 1.00 to 1.46. Azimuth is represented by MLT from 0 to 24. The same parameters as in Figures 26-28 are used.

Northward Component of Auroral Current
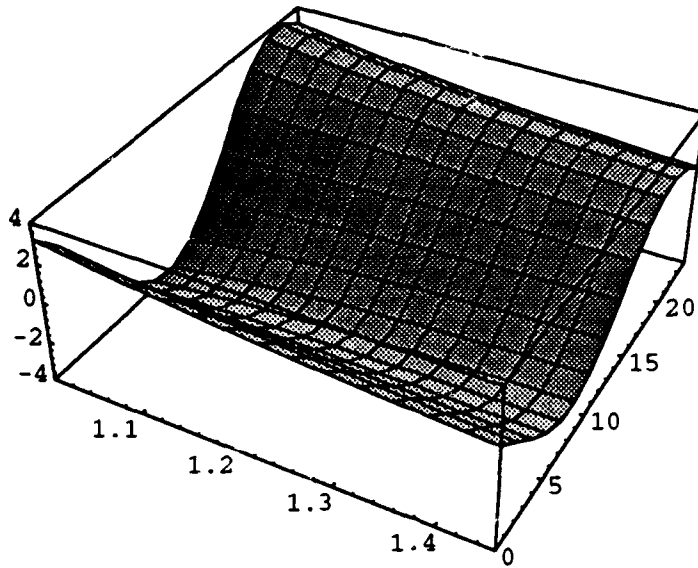
Eastward Component of Auroral Current
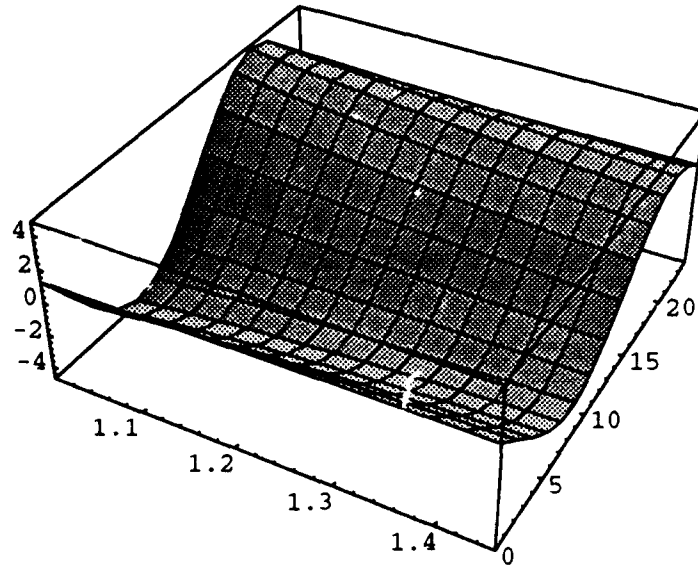
Figure 30. Northward and Eastward components of the auroral current. The 3-D plots are in the same format for the same parameter values as in Figure 29.

94

at the poleward auroral boundary and lags the northward current by 0.07 hours (or 1.05°) at the equatorward boundary. Also apparent in Table 18 is the deep minimum of the total current at θ_2.

Table 18. Auroral Boundary Currents

	E	N	T
At θ_1:			
polar cap	(1.15, 7.8)	(1.15, 1.8)	(1.15, all)
auroral	(4.56, 19.2)	(3.88, 21.8)	max (5.63, 20.2)
			min (1.99, 14.2)
At θ_2			
sub auroral	(.406, 12.2)	(.406, 18.2)	(.406, all)
auroral	(2.89, 20.18)	(2.35, 20.11)	max (3.72, 20.15)
			min (0.326, 14.15)

Current amplitudes and phases are given at the auroral boundaries for the parameter choices used in Figures 26-29. The column E is for the maximum eastward current, N the maximum northward current, and T the total current. The pair of numbers gives the amplitude of the current and its phase in MLT. Values for the maximum and minimum total auroral current are given.

The increased auroral current is produced by two effects: the increased electric field in the auroral zone produced by the shielding effects of the Region II currents, and the enhanced auroral zone conductivity. The ratio of ionospheric currents across an auroral boundary may be written as

$$J_A/J_1 = E_A/q_1 E_1 \tag{112}$$

Here substrict 1 refers to variables outside the auroral zone and subscript A is in the auroral zone. As in the text, Σ is the same across the auroral boundary and q_1 is the ratio of the Pedersen conductivities (1 to A). J is the current density magnitude and E the electric field magnitude. In Figures 25-29, $q_1 = 1/2$ is used so that

$$J_A/J_1 = 2\, E_A/E_1 \tag{113}$$

Thus any difference of the amplification of the current from the value 2 across an auroral boundary is due to the electric field. The maximum amplification at the poleward auroral boundary for Figures 14-19 is $4.9 = 2 \times 2.45$; i.e., a factor or 2 from the conductivity and 2.45 from the enhancement of the electric field. At the equatorward auroral boundary, the maximum amplification is $9.2 = 2 \times 4.6$ so that the electric field enhancement contributes to factor 4.6 to the maximum current enhancement.

E. The Effects of Additional Dayside Currents

Dayside or Cusp Currents. Observations have indicated the presence of additional FACs on the dayside ionosphere in the polar cap. These currents are associated with magnetospheric-ionospheric coupling in the vicinity of the polar cusp. These cusp currents are essentially of two types, pairs of line currents or pairs of sheet currents. The main ionospheric effects of these currents is to alter the convection pattern and fields in the polar cap itself. Ground-based magnetic field signatures are also altered.

The combined presence of line current sources and an ionospheric conductivity that is not uniform gives rise to interesting physical effects and considerations. For example, suppose the only current present is a line current which feeds into the ionosphere at the pole and that only a Pedersen conductivity exists. The current is then radially directed away from the pole in the polar cap. At the polar cap boundary θ_1 current must be conserved. But now the situation is not unique depending upon whether or not FACs exist at θ_1. If there are no such FACs, then the ionospheric current remains radial and proceeds undiminished across θ_1

whether or not the auroral zone has an enhanced conductivity (the electric field may change at θ_1, but the current does not). With the Hall conductivity, however, the situation is more complicated. The same potential that drives the ionospheric current in the presence of only a Pedersen conductivity would, if unaltered, now generate FACs at θ_1 so long as Σ_H changes across θ_1. Thus, if the line current source does not generate FACs at θ_1, the electrical potential (and therefore the ionospheric convection pattern) must be altered. The ionospheric potential and electric field then become *explicitly* dependent upon the ionospheric conductivity.

The approach taken here is that the dayside or cusp currents are of magnetospheric origin and independent of the Region I and Region II currents. Thus, the dayside or cusp currents do not contribute to the FACs at θ_1 or θ_2. Alternative approaches are possible but would be considered only given the motivation of the results of a theory that predicts the proper coupling between or among the possible Birkeland currents entering or leaving the ionosphere.

The additional line and sheet FACs, in proper combination in the dayside polar cap, are referred to as DPZ and DPY currents. The nomenclature relates to the polar distrubances (DP) associated with the Z and Y components of the IMF, respectively.

The DPZ currents may be represented by a pair of line currents of opposite polarity (i.e., into and out of the ionosphere) located symmetrically about 12:00 MLT at high latitudes just poleward of the Region I currents. Essentially the DPZ line currents are located near the flanks of the polar cusp.

The DPY currents have mainly been represented by at least two different current configurations. One is a pair of line currents of opposite polarity both located at local noon

slightly poleward of the Region I currents. The second representation is in terms of current sheets at constant latitude and a few hours extent in MLT, where the polarity of the sheet reverses across noon. In this second configuration, the DPY current sheet extends azimuthally essentially along the polar cleft (the DPZ line currents would then be located at the ends of the DPY sheets near local noon).

Such representations of DPZ and DPY field aligned current configurations are amenable to our analytical approach. With the objective of ultimately treating the full set of FAC variables (Region I, Region II, DPZ and DPY currents) and zonal conductivity changes, and to see the main effects of each, the currents are best treated additively.

Line Current Field Aligned Sources. The solution for the potential for a single line current of intensity I_0 entering the polar cap ionosphere at (θ_b, ϕ_b) is given in units of $(I_o/2\pi\Sigma_p^I)$ in zones I and II by

$$U_I = - \ln R_1 - (1-q) \ln (bR_2)/(1+q) - f \tag{112}$$

$$U_{II} = [2q \ln R_1 + (1-q) \ln r]/(1+q) - g \tag{113}$$

Here $r = y(\theta)/y(\theta_1)$ is the radial variable, q is given in equation 45,

$$R_1(r,b,\phi_b) = \sqrt{r^2 + b^2 + 2rb \cos (\phi + \phi_b)} \tag{113}$$

$$R_2 = R_1(r,1/b,\phi_b) \tag{114}$$

$$b = y(\theta_b)/y(\theta_1) \tag{115}$$

and (θ_b, ϕ_b) locates the point of entry of the line current in the polar cap.

The functions f and g are required to prevent the diversion of the current along the magnetic field at θ_1 and are given by

$$f = \sin \delta_1 \sum_{n=1}^{\infty} (-br/n)^n \sin (n(\phi+\phi_b) + \delta_1) /(1+q) \tag{116}$$

$$g = \sin \delta_1 \sum_{n=1}^{\infty} (-r/bn)^n \sin (n(\phi+\phi_b) + \delta_1)/(1+q) \tag{117}$$

where δ_1 is the same phase given in equation (51).

The potential for any configuration of radial line current sources is gotten from the proper superposition of the single line source solution given in equations 112-117 which is denoted $U(I_o, b, \varphi_b; r)$. Thus, for a pair of line currents symmetrically located from the noon meridian, of equal intensity and opposite direction, the solution is

$$U_{sym} = U(I_o, b, \varphi_b; r) - U(I_o, b, -\varphi_b; r) \tag{118}$$

In equation 118, the line current I_o enters the atmosphere at (b, φ_b) and $-I_o$ departs at $(b, -\varphi_b)$. For an asymmetrical set of line currents of equal intensity (one into and one out of the ionosphere) the solution is

$$U_{asym} = U(I_o, b, \varphi_b; r) - U(I_o, b_1, \varphi_{b_1}; r) \tag{119}$$

In equation 119, the line current I_o enters at (b, φ_b) and the line current $-I_o$ departs at (b_1, φ_{b_1}).

The line current solutions may be superposed directly with the solutions of Case A. The net convection pattern then depends upon the ratio

$$u = (I_o/2\pi\Sigma_p^I)/V_1 \tag{120}$$

where V_1 is the amplitude of the Case A potential at θ_1 as given in equation 3. For $I_o = 10^6$ A, $\Sigma_p^I = 5$ mhos, and $V_1 = 40$ kV, the ratio (120) has the value $u = 0.8$. A representative range of values for u would be

$$0.2 \leq u \leq 1.2 \tag{121}$$

DPZ Effects. The DPZ currents are represented by a pair of high latitude line currents which, for positive IMF Bz, have the polarity of out on the dawn side and in on the dusk side of the ionosphere (which is the opposite sense to the polarity of the Region I currents). For negative IMF Bz, the polarity of the DPZ currents is reversed, thereby matching the polarity of the Region I currents.

In Figure 31 the equipotentials are shown for the DPZ currents with IMF Bz < 0. The line currents are symmetrically located at ±30° from the noon meridian and 10° from the pole. Conductivity parameters are q = 1/2 and Σ = 2. Circles are drawn in the figure to locate the polar cap boundary and the equatorial auroral boundary. Close to the line currents the equipotentials are circles. The distortion in shape from circular is caused by the Hall conductivity in the polar cap and by the conductivity enhancement at y_1, the polar cap boundary. (In Figure 31, as amplified below, the conductivity change is not accounted for at y_2, the auroral equatorial boundary.) Spacing between successive equipotentials is an equal amount (0.2 in units of $I_o/2\pi\Sigma_p^I$) in Figure 31. The zero equipotential runs approximately along the noon-midnight meridian, the slight clockwise twist being caused by the Hall conductivity. The convection is counterclockwise in the morning sector and clockwise in the evening sector.

In the central dayside polar cap, because of the chosen polarity of the DPZ currents, the electric field in Figure 31 is dawn to dusk and the polar cap flow is anti-sunward. In the same region for the reversed line current polarity corresponding to IMF Bz > 0, the electric field and convection velocity are also reversed in direction. In particular, along the noon meridian between the DPZ currents, the convection is anti sunward for IMF Bz < 0 and sunward for IMF Bz > 0. These results are the pure DPZ effects, upon which the effects of Region I and Region II currents are to be superposed.

The line diagrams in Figure 31 compare the DPZ potential to the potential for Region I currents (i.e., Case A) at both y_1 and y_2 for u = 1 (cf., equation 120) which is a rather large value. The DPZ effect is nevertheless seen to be fairly small at both boundaries, y_1 and y_2. For this reason, the small affect of the conductivity discontinuity on the line current solutions in going from zone II to zone III is not included in the analysis.

Symmetrical Line Currents

Potential at y1
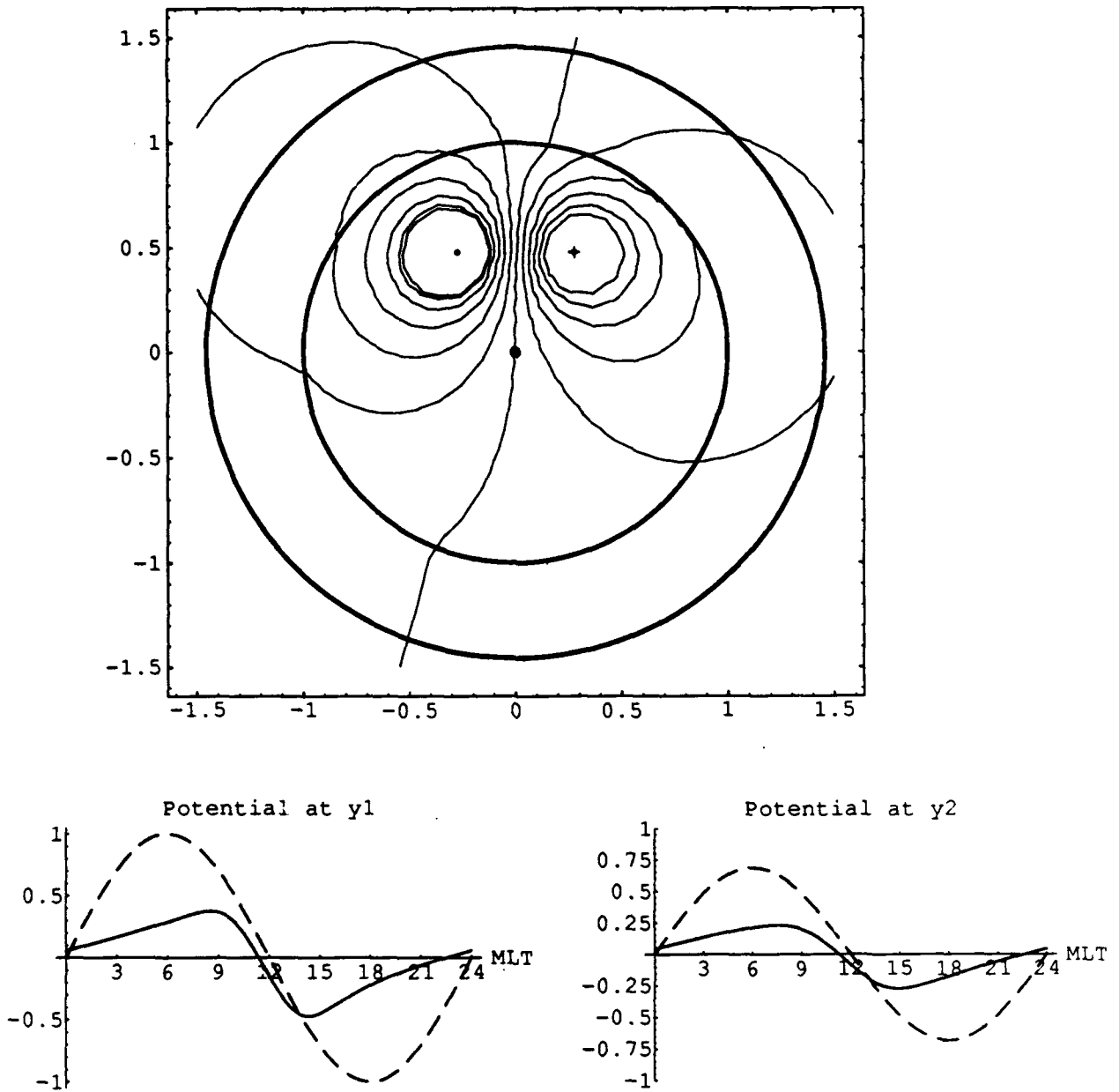
Potential at y2

Figure 31. DPZ equipotentials for IMF Bz negative. Equally spaced equipotentials for the DPZ currents are shown in the contour plot. The radial variable is y/y_1, and $q=1/2, \Sigma=2$. The line current into the ionosphere is at 10:00 MLT and the line current out is at 14:00 MLT; both at 80° latitude: The location of the currents and the magnetic pole are indicated in the diagram. The inner circle is the polar cap boundary and the outer the equatorial auroral boundary. In the line plots, the DPZ potential is compared to the Case A potential (the dashed curve) at the boundaries y_1 and y_2, with $u=1$.

In Figure 32, the combined effects of DPZ currents and Region I currents are shown in equipotential plots for u = 0.4. In the upper diagram, the DPZ polarity is for IMF Bz < 0; in the lower diagram, the DPZ polarity is for IMF Bz > 0. For IMF Bz < 0, the equipotential and convection patterns in the polar cap are similar to that of Case A except in the close proximity of the line currents. In the vicinity of the line currents, the equipotentials are always circular and the convection exhibits a strong vortex, counterclockwise about the line current into the ionosphere and clockwise about the current out of the ionosphere. The cross cap anti sunward flow is fastest in the "neck" region between the line currents, where the electric field is also enhanced and directed dawn-to-dusk. There are two principal effects created by the DPZ IMF Bz > 0 currents: the creation of the neck region of fast, anti sunward flow between the line currents, and the development of two additional convection cells in the polar cap. The convection in the two morning cells (a tight cell due to the line current and the broad Region I current cell) is counter clockwise; and the convection in the two afternoon cells is clockwise.

For IMF Bz > 0, a dramatic difference in the polar cap potential and convection flow takes place. The zero potential is now along the noon-midnight meridian and includes the dayside loop that encompasses the two line currents with the formation of two "eyes" in the diagram. Where equipotentials form a closed loop, a FAC source is enclosed. The "eyes" in the diagram give it a beetle-like appearance, and the eyes of the beetle are convection cells associated with the DPZ effects. The flow between the centers of the DPZ positive cells is sunward, which is opposite to that associated with Region I currents alone.

Because the line currents have opposite polarity to the Region I currents, the zero potential loop about the eyes represents a total blockage of the anti-sunward polar cap flow along the noon-midnight meridian of Case A. Outside the loop, the flow though distorted is similar to Case A. The size of the loop depends on the parameter u. In the morning half of
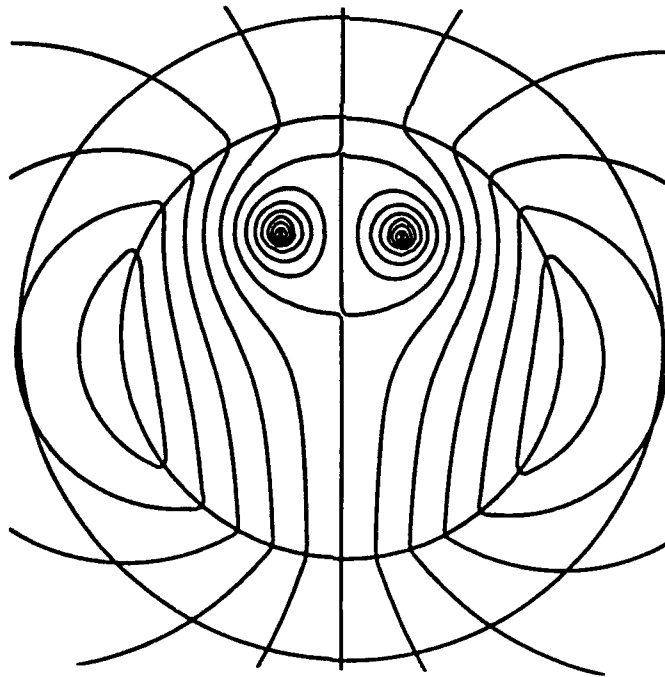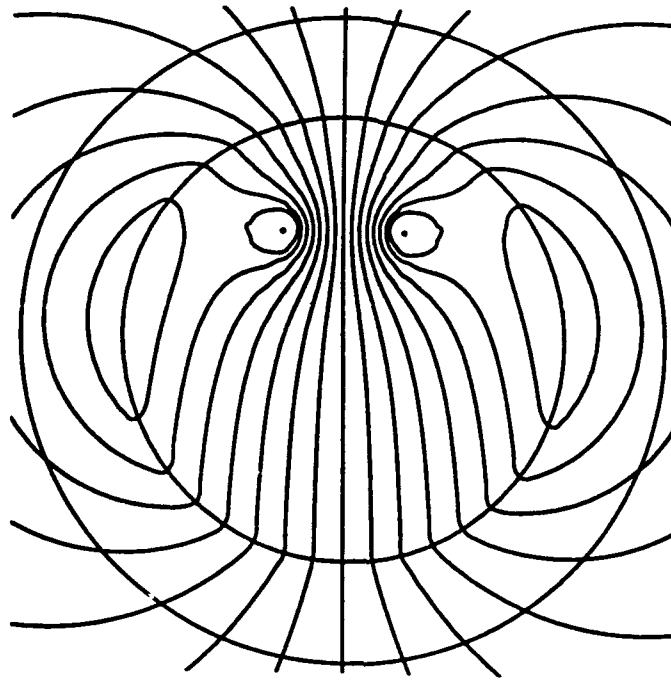
Figure 32. Region I and moderate DPZ currents. The plots are of the total DPZ plus
Case A equipotentials for $u = 0.4$, $q = 1/2$, and $\Sigma = 2$. The upper diagram is for
IMF $B_Z < 0$ and the lower diagram for IMF $B_Z > 0$.

the loop, a clockwise vortex flow takes place; in the evening half, a counterclockwise vortex flow takes place. Across the dayside polar cap, the flow is antisunward at the flanks near the polar cap boundary but the dominant features are the convection vortices.

Figure 33 is in the same format as Figures 31 and 32 and shows the convection pattern for DPZ plus Region I plus Region II currents. The left column in Figure 33 is for IMF Bz < 0 and the right column for IMF Bz > 0. The line plots show the potentials along selected lines parallel to the dawn-dusk meridian. The solid curve is the total potential (DPZ + Region I + Region II) and the dashed curve is for no DPZ currents (i.e., for Case B alone).

Sheet Currents. We may represent DPY dayside current effects as due to line or sheet current sources. In one configuration, the line current sources are located on the noon meridian and the sheet currents are azimuthally extended and essentially located along the polar cleft. The solutions for the line current configurations are constructed from the line current solutions given above.

For the representation of potential effects in terms of sheet currents, we use the following model. Two sheets are used located at the same latitude and carrying current I_{sh} into the ionosphere and current I_{sh} out of it. The input current sheet is located on the dayside, morning sector at the latitude θ_{sh} in the azimuthal range β_1 to β_0 (measured from the noon meridian) so that

$$\beta_0 > \beta_1 \tag{122}$$

The output current sheet is located symmetrically (with respect to the noon meridian) in the afternoon sector. The solution for the current sheets is denoted $V_{sh}(\theta,\varphi)$ and may be defined in terms of an infinite series:

$$V_{sh}(\theta,\varphi) = (I_{sh}/\Sigma_p^I) \sum_{n=1}^{\infty} e_n \left(T_n^{(1)}(\theta) \sin n\phi + T_n^{(2)}(\theta) \cos n\phi \right) \tag{123}$$

Dawn-dusk meridian

Across PC thru LC

Dayside auroral zone

-Graphics-

Dawn-dusk meridian

Across PC thru LC

Dayside auroral zone
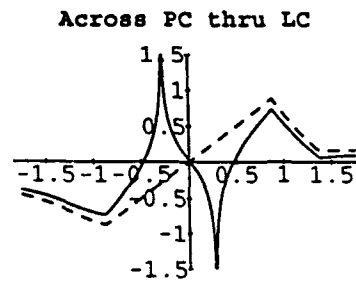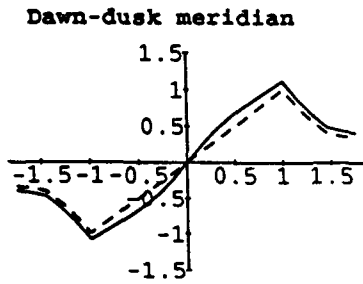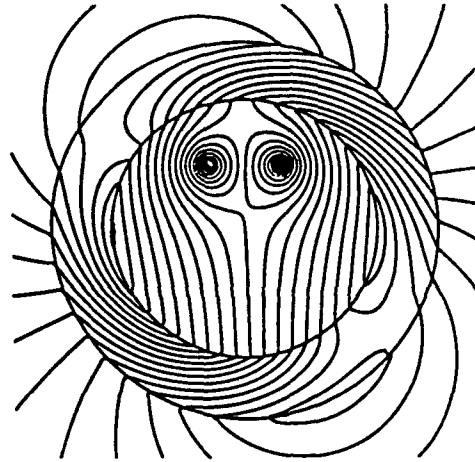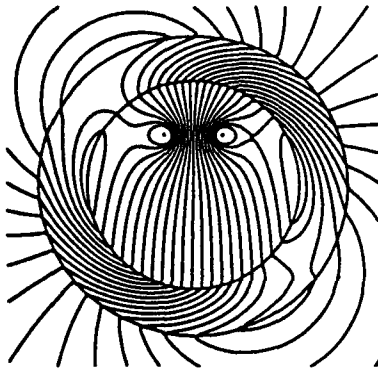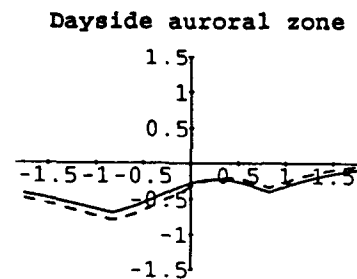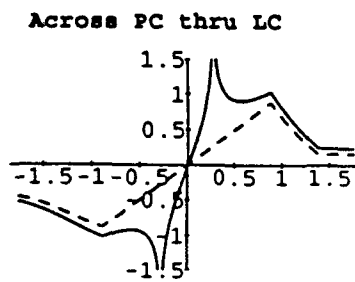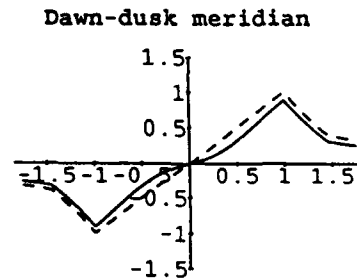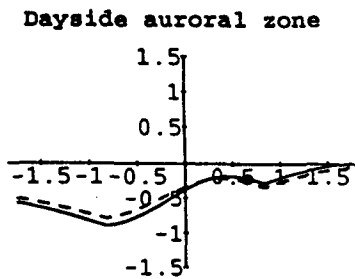
Figure 33. Equipotentials for DPZ, Region I, plus Region II potentials. The contour plots use the same parameters as Figures 32, plus $v_2 = 0.8$, $\varphi_2 = \pi/3$. The line plots apply to the contour plot at the top of the column, IMF B_z negative for the left column and positive for the right column. The line plots give the potential including the DPZ currents (solid curve) and excluding them (dashed curve) along selected cuts across the polar cap parallel to the dawn-dusk meridian.

105

where

$$e_n = \left((-1)^n/\pi \ (\beta_0 - \beta_1)n^2\right) \left(\cos n\beta_1 - \cos n\beta_0\right) \qquad (124)$$

and the latitude dependent functions $T_n^{(1)}$ and $T_n^{(2)}$ are given by:

$\underline{\theta \leq \theta_{sh}}$:
$$T_n^{(1)} = (y/y_{sh})^n + (C-1) \ (y \ y_{sh}/y_1^2)^n \qquad (125)$$

$$T_n^{(2)} = B(y \ y_{sh}/y_1^2)^n \qquad (126)$$

$\underline{\theta_{sh} \leq \theta \leq \theta_1}$:
$$T_n^{(1)} = (y_2/y)^n + (C-1) \ (y \ y_2/y_1^2) \qquad (127)$$

$$T_n^{(2)} = B \ (y \ y_2/y_1^2) \qquad (128)$$

$\underline{\theta_1 \leq \theta}$:
$$T_n^{(1)} = C \ (y_2/y)^n \qquad (129)$$

$$T_n^{(2)} = B \ (y_2/y)^n \qquad (130)$$

Here θ_2 is the latitude of the equatorial boundary, θ_1 is the polar cap boundary,

$$y = y \ (\theta), \ y_2 = y \ (\theta_2), \ y_1 = y \ (\theta_1), \ y_{sh} = y(\theta_{sh}), \qquad (131)$$

$$B = 2q \ (1-q) \ \Sigma/\kappa; \ C = 2q \ (1+q)/\kappa \qquad (132)$$

and κ is given in equation 50. The boundary conditions satisfied by the solution are that the potential $V_{sh}(\theta,\varphi)$ is everywhere continuous and there are no FACs due to the sheet currents at the polar cap boundary θ_1.

A comparison of the potentials for sheet currents and line currents is made in Figure 34. The contour plots are drawn with equipotentials of the same value and with the same increment between successive contours of 0.2. The potential is in units of I/Σ_p^I where I is the current input, taken to be equal for the two configurations. The currents in Figure 34 are located at $12°$ colatitude from the pole. The line currents are located at $\pm 7\pi/32$ (or $39°$) from the noon meridian. The sheet currents are $\pi/16$ (or $11.25°$) in azimuthal extent, and also centered at $\pm 39°$ from the noon meridian. The ionospheric potential distributions for these symmetrically constructed current configurations of equal strength are very similar. The line diagrams in Figure 34 give in radians the MLT dependence of the potentials for selected colatitudes: at $12°$ where the currents are located, and at the polar cap boundary ($18°$). The line current potential is generally fractionally larger than the sheet current potential, with the
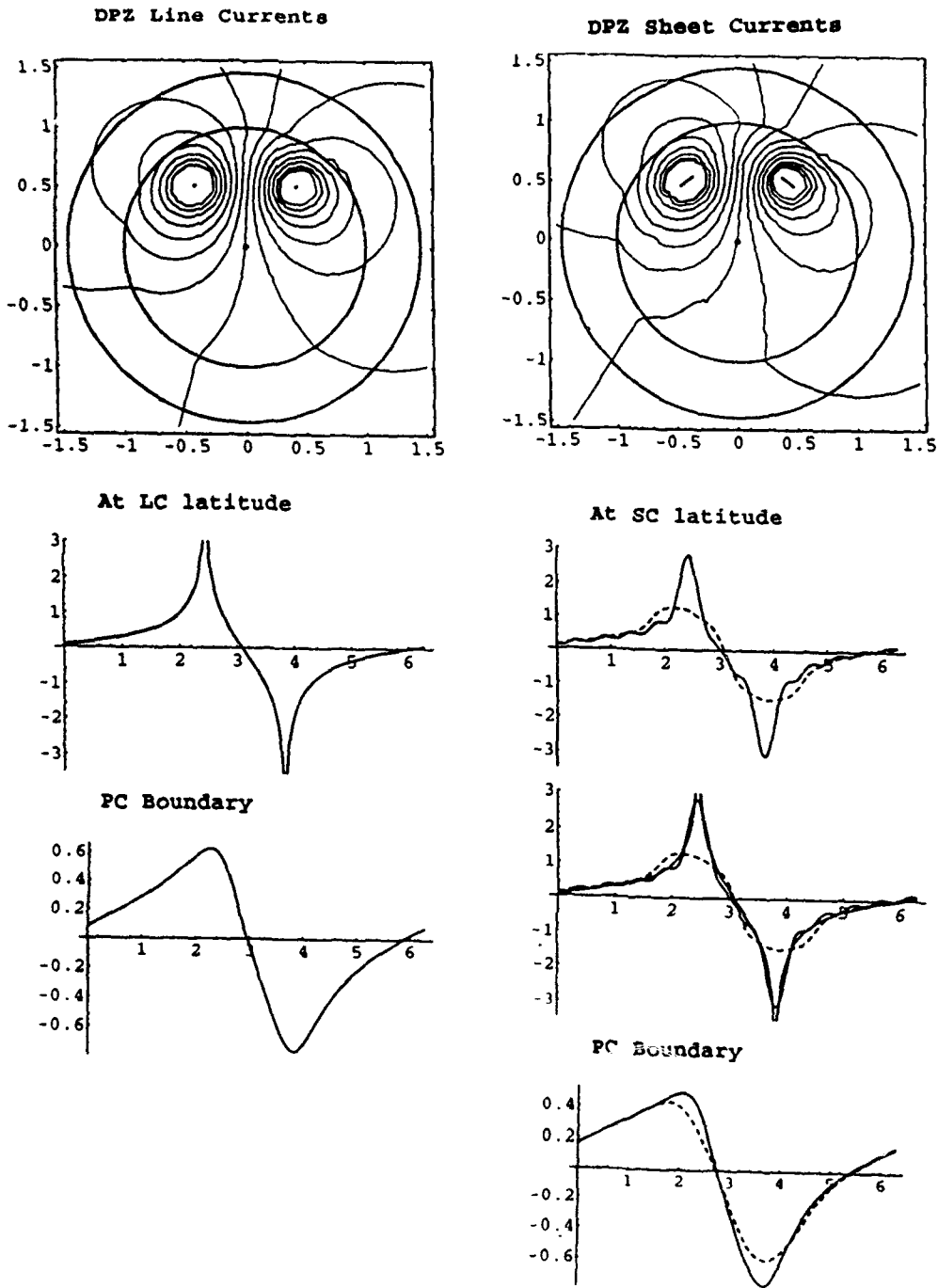
Figure 34. Comparison of line and sheet current potentials. The line currents (LC) and sheet currents (SC) are of equal intensity and the plot is for q=1/2, Σ= 2 . The difference between equipotentials is 0.2 in units of I/Σ_p^1 , where I is the imput current. The colatitude of the currents is 12°. The line plots give the potentials at 12° and at the polar cap (PC) boundary. The dashed curves in the right column give the potential when the sheet current's azimuthal extent is doubled. The second line diagram gives LC,SC, and extended SC potential at 12°. The small wiggles in the sheet current plots, where maifest, are not real and result from truncation of the slowly converging series of equation 123.

107

overall configuration being very similar. The only large difference is within a circle of about 2° at the line current itself wherein the line current potential becomes singular. For most purposes, appropriately chosen sheet and line currents may be used interchangeably.

The effect of spreading out the sheet current is also demonstrated in the right column of Figure 34. For the dashed curves in the line plots, the same sheet current is spread over twice the azimuthal extent (from 11.25° to 22.5°). At the sheet current latitude the effect is to smear out the peak in the potential along the more extended current. Away from the sheets, changes are small and qualitative differences wash out.

In the sheet current contour and line plots, the wiggles apparent in Figure 34 are not real in that they result from truncation of the slowly converging infinite series in equation (123) in the numerical evaluations.

DPY Effects. Convection patterns with modelled DPY effects are shown in Figure 35. On the left, the potential is shown for a pure DPY line current configuration that consists of a pair of currents on the noon meridian, in at 5° colatitude and out at 15° colatitude. The line current polarity is selected to generate a west to east convection across the central dayside polar cap between the line currents. Of course, if the polarity of the line currents is reversed, the convection direction is also everywhere reversed in the diagram. A principal effect of the DPY currents is to generate significant dayside convection orthogonal to the noon-midnight meridian. Sheet currents similarly symmetrically located across the noon meridian and separated by a latitudinal gap would also produce an east-west or west-east convection within the gap.

The right column of Figure 35 shows the effects of adding Region I currents to the pure DPY currents on the left. The ratio of the line current intensity to the total Region I

DPY Line Currents

DPY + RI Currents

Auroral Zone

Auroral Zone

Potential

Polar Cap

Polar Cap

Potential
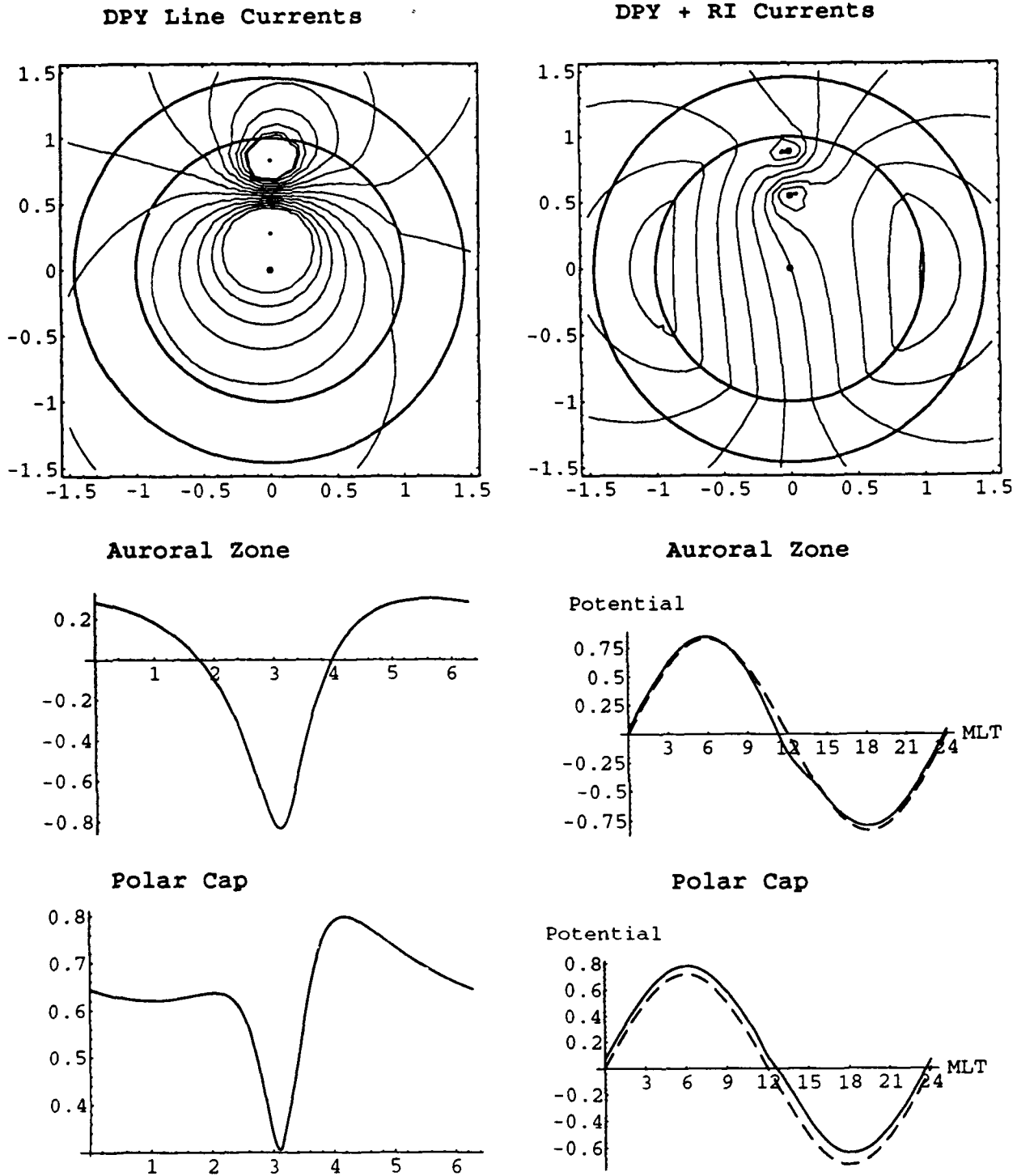
Figure 35. DPY line current effects. The format is the same as for Figures 31-33, and the conductivity parameters are q=1/2, and Σ= 2 . The left column is for a pair of DPY line currents, in on the dayside meridian at 5° colatitude and out at 15° colatitude, and the right column adds Region I currents. In the line plots, the potential is shown in the auroral zone at the colatitude θ = 21.5° and in the polar cap at θ = 10° (which is midway between the two line currents) as a function of azimuth in radians or MLT. Zero azimuth is the same as 00 MLT, and π is the same as 12 MLT. In the plot, the ratio of the line current intensity to the total Region I current is 0.35.

current is 0.35. The net convection pattern is basically antisunward in the polar cap except for the dayside eastward flow at latitudes between the line currents. The line plots give the azimuthal dependence of the potential at fixed colatitudes, at $\theta = 21.5°$ in the auroral zone and $\theta = 10°$ midway between the line currents in the polar cap.

In Figure 36, the combined effects of DPY line currents (LC), Region I (RI), and Region II currents are shown. The ratio of currents LC/RI is 0.35 for the left column and 1.5 for the right column. For the weaker LC on the left, the dayside flow within about 2 hours of local noon is west to east. With a current reversal and intensification, the dayside flow within 4 to 5 hours of local noon is east to west for the right column.

An arrangement of dayside line currents located asymmetrically with respect to the noon meridian gives rise to convection patterns as demonstrated in Figure 37. The dayside line currents in Figure 37 have the same polarity as the Region I currents: the pre noon line current is into the ionosphere and the post noon one is out. The polarity corresponds to IMF $Bz < 0$. The IMF By effect is simulated by the latitudinal placement of the line currents. For IMF $By > 0$, the inward line current is at the larger colatitude ($\theta = 10°$ in Figure 37) and line current out is at the more poleward latitude ($\theta = 5°$). For IMF $By < 0$, the latitudes are reversed. The affect of the asymmetrically located line currents is to produce a flow through the gap between the line currents. The inner circle in Figure 37 is at $12°$, well within the polar cap. The dayside flow through the circle resembles that proposed by Moses *et al.* (1987) in their effort to model certain dynamics of the polar cap. For IMF $By > 0$, the flow through the gap originates at post noon MLTs and proceeds west to east. This is shown in the upper two contour plots, left column of Figure 37. For IMF $Bz < 0$, the flow through the gap originates at pre noon MLTs and proceeds east to west.

DPY + RI + RII Currents   **DPY + RI + RII Currents**

Auroral Zone   **Auroral Zone**

Polar Cap   **Polar Cap**
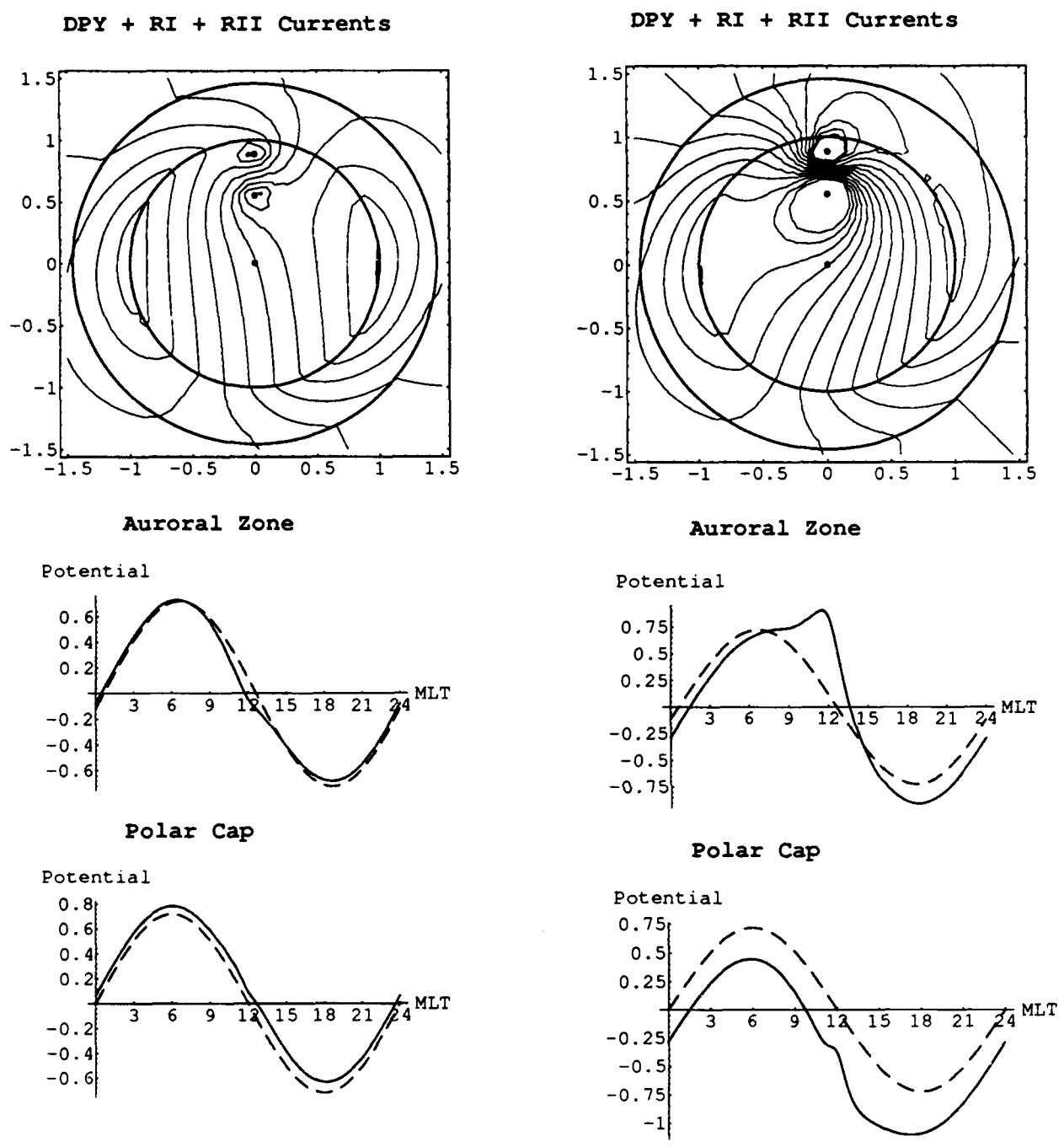
Figure 36. DPY, Region I, and Region II currents. The format and parameters are the same as in Figure 35. For the left column, the ratio of currents LC/RI is 0.35. For the right column, the polarity of the LCs is reversed and the ratio LC/RI is 1.5.

Gap: By>0,Bz<0,LC/RI=0.35
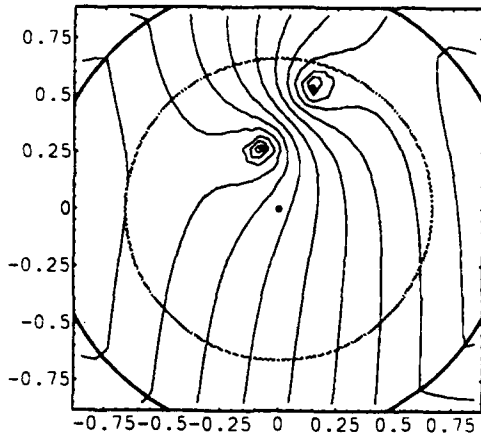
Gap:By<0,Bz<0,LC/RI=0.35
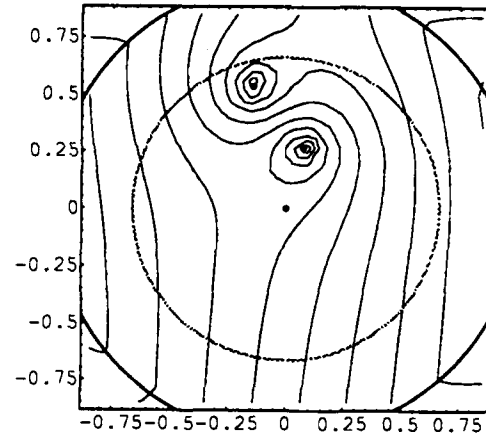
Gap: By>0,Bz<0,LC/RI=1.5
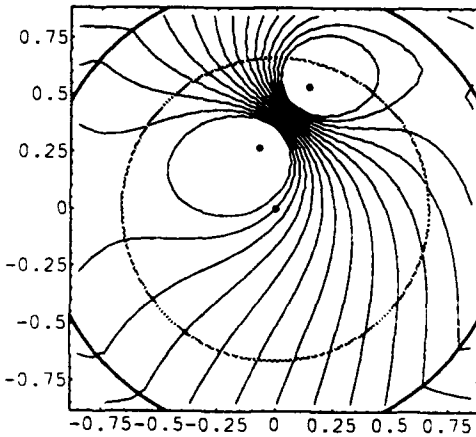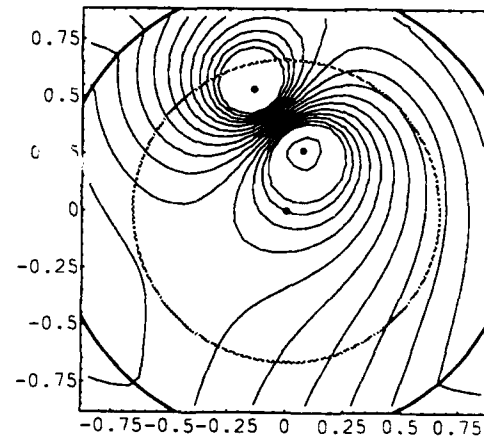
Gap:By<0,Bz<0,LC/RI=1.5
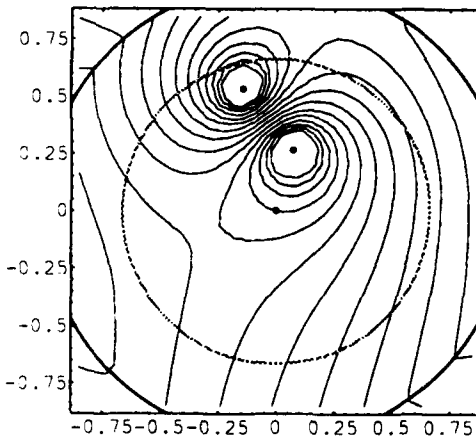
Gap:By<0,Bz<0,LC/RI=1

Gap:By<0,Bz<0,LC/RI=1,V=0
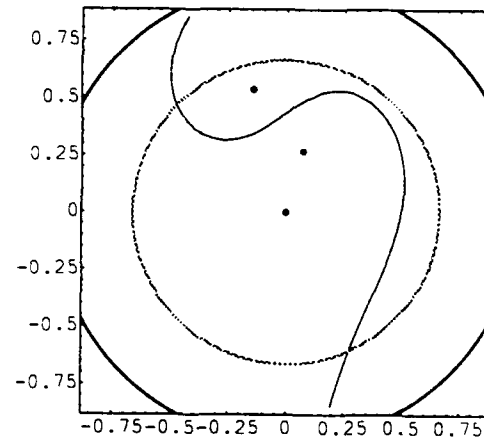
Figure 37. IMF By gap effect. Contour plots are shown to simulate convection in the central dayside polar cap for IMF By < 0 (left column) and IMF By >0 (right column first two rows). The ratio of line current to the total Region I current intensity is 0.35 in the first row, and 1.2 in the second row. The line currents have the polarity of RI currents and are located at colatitudes of 10° and 5°. The inner circle is at colatitude $\theta = 12^o$ and the outer circle is the polar cap boundary at $\theta = 18^o$. The third row is for IMF By<0 and LC/RI=1; the first contour plot is of the potential and the second identifies the V=0 contour.

112

The third row in Figure 37 is for LC/RI = 1 and IMF By < 0 and shows both the convection pattern and the zero-potential line.

Examples of combined sheet and line currents are shown in Figure 38, which also includes Region I and Region II currents. The location of the sheet currents and line currents are apparent in the contour plots. The Region II currents are prescribed by the parameters $v_2 = 0.41$ and $\varphi_2 = 0$, and all potentials are in units of V_1, half the polar cap potential drop. The ratio of LC/RI current intensities is taken to be 0.35. (Figure 38 may best be compared to Figure 33 (also to Figure 34).) The role of the sheet current in Figure 38 is to soften the DPZ effect of the line currents.

In the left column of Figure 38 the polarity of the sheet current, line current, and Region I current is the same, corresponding to IMF Bz < 0. The neck or constriction along the noon meridian, where the convection is rapid, is apparent. The steepness of the potential at the colatitude of the currents ($r_1 = 12°$) results primarily from the singularity of the line current potential. The convection is a two cell pattern controlled on the dayside by the line and sheet currents, rather than by the Region I currents. The flow is antisunward across the central polar cap, and significant east-west flow is generated at the dawn-dusk meridian as the constricted dayside flow expands into the nightside polar cap.

In the right column of Figure 38, the polarity of the line current has been reversed corresponding to IMF Bz > 0. The affect is to produce the two additional convection cells (or "eyes") about the noon meridian. The nightside convection is basically the antisunward convection characteristic of the Region I currents alone. The dayside convection has four cells, alternating in circulation sense in crossing the cap. The convection cells at the flanks of the polar cap are the Region I cells, broadened and distorted by the DPZ currents. The inner
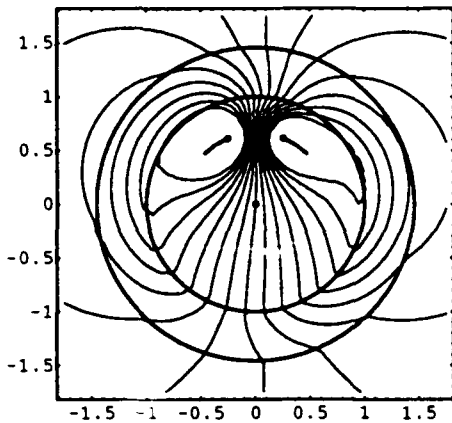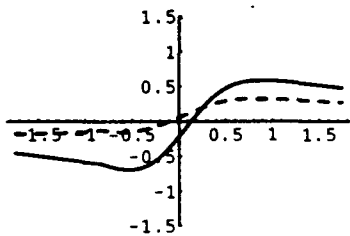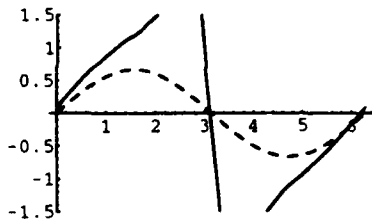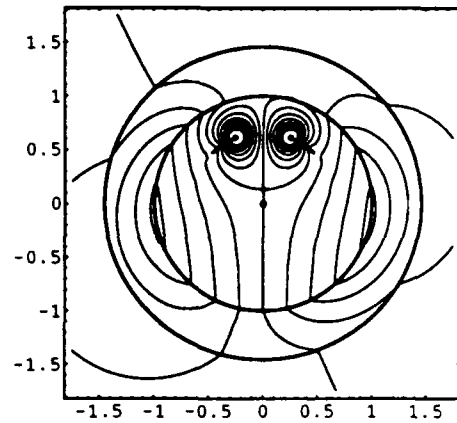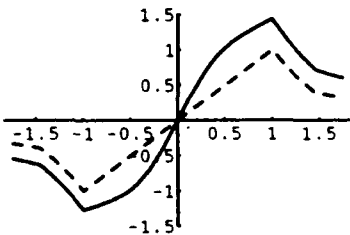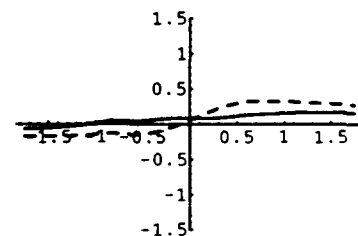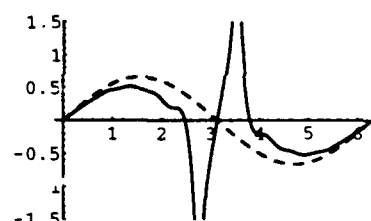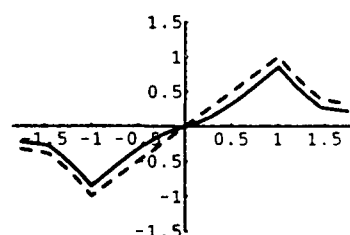
Figure 38. Combined RI, RII, LC, and Sheets. The combined effects are shown for Region I, Region II, line currents, and sheet curents. Parameters used are q=1/2, Σ= 2, v_2=0.41,φ_2=0, LC/RI = 1.04, and SC/RI = 0.35. In the left column the line, sheet, and Region I currents have the same polarity. On the right, the polarity of the line current is reversed. The line plots give the potential at selected colatitudes of 21.5° in the auroral zone and r_1=12°, and along the dawn-dusk meridian. The line and sheet currents are located at r_1. The dashed curves give the Region I + II potential of case B and the solid curves give the total potential.

convection cells on either side of the noon meridian are comparatively smaller and more intense.

F. Summary and Conclusions

Analytical models have been developed to simulate how ionospheric currents relate to a selection of field aligned currents (FACs). The FACs are regarded as input or given currents that produce a global distribution of ionospheric currents and electric fields. In the analysis, the ionosphere is modelled as a conducting, spherical shell, the magnetic field is radial (which is satisfactory at high latitudes), and stationary state is assumed. The auroral zone may have an enhanced electrical conductivity, but other than at the auroral boundaries the conductivity is uniform. Hence day-night conductivity effects are not included.

The FACs considered include Region I, Region II, line currents, and sheet currents. The Region I and II currents are located at the poleward and equatorial auroral boundaries, respectively, and the line currents and sheet currents are placed in the dayside cusp region.

In the presence of only Region I currents, the ionospheric currents and fields are determined from either the potential or the FACs at the auroral boundary. The latter two variables may not be prescribed independently. Given the potential, the intensity and phase of the Region I FACs are determined with the following results:

(1)   The Region I FAC intensity is proportional to the potential V_1 and depends upon the auroral conductivity enhancement through the variables q and Σ.

(2)   The phase of the Region I FAC depends sensitively on the auroral conductivity enhancement and generally differs from the phase of the potential.

(3)   As the auroral Pedersen conductivity is enhanced, the Region I FACs rotate counterclockwise with increased intensity, thereby accommodating more direct entry of the FACs into the auroral zone.

(4) The ionospheric currents, though coupled to, are not determined in a simple way by the Region I FACs. The ionospheric currents depend sensitively directly upon the ionospheric conductivity and indirectly upon boundary conditions.

(5) The power dissipated in the ionosphere is greater in the auroral zone because of its enhanced conductivity.

(6) In the auroral zone, the ionospheric currents are most intense at the polar cap boundary.

In the presence of both Region I and Region II currents, many new properties are introduced. The basic variables are the potential and FAC at each auroral boundary, and only two of the four quantities are independent. A general solution was obtained using the potential at the polar cap boundary and the Region II FAC (intensity and phase) as the independent variables, in terms of which the potential at the auroral boundary and the Region I FACs are predicted. Many unusual situations are permitted by the general solution, and only a few selective cases of physical interest were presented. Important results include the following:

(1) The phase of the potential at the equatorial auroral boundary is the crucial parameter for producing azimuthal convection in the auroral zone.

(2) The primary physical effect of the Region II FACs is to inhibit ionospheric electric fields from penetrating to sub auroral latitudes.

(3) Region II currents may exist without Region I currents, or vice versa.

(4) In the empirical range of values for Region II currents, the predicted Region I currents are phase shifted ($\delta_1 < 0$) counterclockwise such that they enter the ionosphere from post midnight to post noon azimuths, and are of greater intensity than the Region II currents. The predicted potential indicates that the

electrical shielding effect of the Region II current weakens as the Region II current intensity increases.

(5)   The ionospheric current in the auroral zone varies in MLT in the presence of Region II FACs. The auroral current is amplified by the enhanced conductivity and by the enhanced electric field in the auroral zone. The auroral current is largest at the polar cap boundary and amplified more at the equatorial boundary.

Line currents and sheet currents of limited extent were introduced to simulate high latitude FAC effects in the vicinity of the polar cusp. It was shown that for most considerations, such currents (lines and sheets) may be used interchangably. When two line currents are arranged symmetrically with respect to the noon meridian (DPZ effect) the main properties are:

(1)   IMBz < 0, line currents of the same polarity as Region I currents: A narrow channel of rapid antisunward flow is created between the line currents. Two local but intense vortex flows are created around the line currents, counterclockwise at the pre noon location and clockwise at the post noon location. Significant transverse (east-west) convection occurs as the channeled flow expands towards the nightside polar cap.

(2)   IMFBz > 0, line currents of opposite polarity to Region I: Two intense dayside cusp convection cells or vortices are formed that interrupt the antisunward convection across the polar cap. The pre noon vortex is clockwise and the post noon vortex is counterclockwise.

(3)   The effects described become more pronounced on a larger spatial scale as the ratio of current intensities LC/RI increases.

When the line currents are located on the noon meridian (DPY effect) the main properites are:

(1)   A channel of intense flow transverse to the noon meridian is generated between the line currents. The transverse flow is westward if the inward line current is at the lower latitude, and eastward if at the higher latitude.

(2)   If the channelled flow is westward, the dayside flow across the central cap comes from the pre noon sector of the polar cap boundary. If the channelled flow is eastward, the dayside flow across the central cap comes from the post noon sector of the polar cap boundary.

The channelling effect is dramatized by an asymmetric arrangement of the DPY line currents with respect to the noon meridian. This was demonstrated for two line currents of Region I polarity (hence, IMF $Bz < \iota$, located $\pm$ 1 hour from the noon meridian at different colatitudes (say, 5° and 10°). The channelled flow proceeds as before but is now essentially transverse to the line connecting the line currents, which is tilted (about 56°) with respect to the noon meridian. The net effect is to simulate a convection gap that is similar to an IMF By effect on the dayside flow.

The basic tools have been assembled to model many FAC and convection effects of interest. To proceed, empirical guidance would be necessary. A suitable next step would be to model selected case studies of observed or proposed convection patterns from satellite or radar observations.

One consideration not included in the analysis is the day-night conductivity gradient. The equations become more complex with this effect included in the analytical approach. The day-night effect must be included if truly global high latitude effects are modelled. For some considerations, however, such as DPY or DPZ effects where most changes are on the dayside except for very intense FACs, the day-night contributions are small.

REFERENCES

Atkinson, G., and D. Hutchinson, Effect of the day-night ionospheric conductivity gradient on polar cap convective flow, *J. Geophys. Res.*, *83*, 725, 1978.

Axford, W.I., and C.O. Hines, A unifying theory of high-latitude geophysical phenomena and geomagnetic storms, *C. J. Phys.*, *39*, 1433, 1961

Banks, P.M., T. Araki, C.R. Clauer, J.P. St. Maurice, and J.C. Foster, The interplanetary electric field, cleft currents, and plasma convection in the polar caps, *Plant. Space Sci.*, *32*, 1551, 1984.

Blanc, M., Magnetospheric convection effects at mid-latitudes, 3, Theoretical derivation of the distrubance convection pattern in the plasmasphere, *J. Geophys. Res.*, *88*, 235, 1983.

Blanc, M., and G. Caudal, The spatial distribution of magnetospheric convection electric fields at ionospheric altitudes: A review, 2, Theories, *Ann Geophys.*, *3*, 27, 1985.

Caudal, G., and M. Blanc, The spatial distribution of magnetospheric convection electric fields at ionospheric altitudes: A review, 1, Observations, *Ann. Geophys.*, *1*, 519, 1983.

Caudel, G., and M. Blanc, Magnetospheric convection during quiet or moderately disturbed times, *Rev. Geophys.*, *26*, 809-822 (1988).

Clauer, C.R., and P.M. Banks, Relationship of the interplanetary electric field to the high-latitude ionospheric electric field and currents: Observations and model simulation, *J. Geophys. Res.*, *91*, 6959, 1986.

Clauer, C.R., P.M. Banks, A.Q. Smith, T.S. Jorgensen, E. Friis-Chrstensen, S. Vennerstrom, V.B. Wickwar, J. Kelly, and J. Doupnik, Observations of interplanetary magnetic field and of ionospheric plasma convection in the vicinity of the dayside polar cleft, *Geophys. Res. Lett.*, *11*, 891, 1984.

Crooker, N.U., Dayside merging and cusp geometry, *J. Geophys. Res.*, *84*, 951, 1979.

D'Angelo, N., Field-aligned currents and large scale magnetospheric electric fields, *Ann. Geophys.*, *36*, 31, 1980.

Dungey, J.W., Interplanetary magnetic field and the auroral zones, *Phys. Rev. Lett.*, *6*, 47, 1961.

Erickson, G.M., and R.A. Wolf, Is steady convection possible in the Earth's magnetotail?, *Geophys. Res. Lett.*, *7*, 897, 1980.

Fedder, J.A., and J.G. Lyon, The solar wind-magnetosphere-ionosphere current-voltage relationship, *Geophys. Res. Lett.*, *14*, 880, 1987.

Fejer, J.A., *J. Geophys. Res.*, *69*, 123 (1964).

Friis-Christensen, E., Y. Kamide, A.D. Richmond, and S. Matsushita, Interplanetary magnetic field control of high-latitude electric fields and currents determined from Greenland magnetometer data, *J. Geophys. Res., 90,* 1325, 1985.

Fontaine, D., M. Blanc, L. Reinhart, and R. Glowinski, Numerical simulations of the magnetospheric convection including the effects of electron precipitation, *J. Geophys. Res., 90,* 8343, 1985.

Heelis, R.A., The effects of interplanetary magnetic field orientation on dayside high-latitude ionospheric convection, *J. Geophys. Res., 89,* 2873, 1984.

Heppner, J.P., and N.C. Maynard, Empirical high-latitude electric field models, *J. Geophys. Res., 92,* 4467, 1987.

Iijima, T., and T.A. Potemra, The amplitude distribution of field-aligned current at northern high latitudes observed by TRIAD, *J. Geophys. Res., 81,* 2165, 1976a.

Iijima, T., and T.A. Potemra, Field-aligned current in the dayside cusp observed by TRIAD, *J. Geophys. Res., 81,* 5971, 1976b.

Iijima, T., T.A. Potemra, L.J. Zanetti, and P.F. Bythrow, Large-scale Birkeland currents in the dayside polar region during strongly northward IMF: A new Birkeland current system, *J. Geophys. Res., 89,* 7441, 1984.

Iijima, T., and T. Shibaji, Global characteristics of northward IMF-associated (NBZ) field-aligned currents, *J. Geophys. Res., 92,* 2408, 1987.

Meng, C.-I., R.H. Holzworth, and S.-I. Akasofu, Auroral circle delineating the poleward boundary of the quiet auroral belt, *J. Geophys. Res., 82,* 164, 1977.

Moses, J.J., G.L. Siscoe, N.U. Crooker, and D.J. Gorney, IMF By and day-night conductivity effects in the expanding polar cap convection model, *J. Geophys. Res., 92,* 1193, 1987.

Nopper, R.W., Jr., and R.L. Carovillano, Polar-equatorial coupling during magnetically active periods, *Geophys. Res. Lett., 5,* 699-702, 1978.

Nopper, R.W., Jr., and R.L. Carovillano, Ionospheric electric fields driven by field-aligned currents, in *Quantitative Modeling of Magnetospheric Processes, Geophys. Monogr. Ser.,* vol. 21, pp. 557-568, edited by W.P. Olson, AGU, Washington, D.C. 1979.

Nopper, R.W., Jr., and R.L. Carovillano, On the orientation of the polar cap electric field, *J. Geophys. Res., 84,* 6489-6492 (1979).

Ogino, T., R.J. Walker, M. Ashour-Abdalla, and J.M. Dawson, An MHD simulation of the effects of the interplanetary magnetic field By component on the interaction of the solar wind with the Earth's magnetosphere during southward interplanetary magnetic field, *J. Geophys. Res., 91,* 10,029, 1986.

Pellat, R., and G. Laval, Remarks on the steady and time dependent mathematical convection models, in *Critical Problems of Magnetospheric Physics,* edited by E.R. Dyer, Inter-Union Commission on Solar-Terrestrial Physics, Washington, D.C., 1972.

Potemra, T.A., Observation of Birkeland currents with the TRIAD satellite, *Astrophys. Space Sci.*, *58*, 207, 1978.

Reiff, P.H., and J.L. Burch, IMF By-dependent plasma flow and Birkeland currents in the dayside magnetosphere, 2, A global model for northward and southward IMF, J. Geophys. Res., 90, 1595, 1985.

Senior, C., and M. Blanc, On the control of magnetospheric convection by the spatial distribution of ionospheric conductivities, *J. Geophys. Res.*, *89*, 261, 1984.

Siscoe, G.L., and T.S. Huang, Polar cap inflation and deflation, *J. Geophys. Res.*, *90*, 543, 1985.

Southwood, D.J., The role of hot plasma in magnetosphere convection, *J. Geophys. Res.*, *82*, 5512, 1977.

Spiro, R.W., and R.A. Wolf, Electrodynamics of convection in the inner magnetosphere, in *Magnetospheric Currents, Geophys. Monogr. Ser.*, vol. 28, edited by T.A. Potemra, p. 247, AGU, Washington, D.C., 1984.

Stern, D.P., The origins of Birkeland currents, *Rev. Geophys.*, *21*, 125, 1983.

Vasyliunas, V.M., Mathematical models of magnetospheric convection and its coupling to the ionosphere, in *Particles and Fields in the Magnetosphere*, edited by B.M. McCormac, p. 60, D. Reidel, Hingham, Mass., 1970.

Vasyliunas, V.M., The interrelationship of magnetospheric processes, in *Earth's Magnetospheric Processes*, edited by B.M. McCormac, p. 29, D. Reidel, Hingham, Mass., 1972.

Wolf, R.A., Effects of ionospheric conductivity on convective flow of plasma in the magnetosphere, *J. Geophys. Res.*, *75*, 4677, 1970.

Wolf, R.A., The quasi-static (slow-flow) region of the magnetosphere, in *Solar-Terrestrial Physics, Principles and Theoretical Foundations*, edited by R.L. Carovillano and J.M. Forbes, p. 303, D. Reidel, Hingham, Mass., 1983.

Zanetti, L.J., T.A. Potemra, T. Iijima, W. Baumjohann, and P.F. Bythrow, Ionospheric and Birkeland current distributions for northward interplanetary magnetic field: Inferred polar convection, *J. Geophys. Res.*, *89*, 7453, 1984.

4. ENERGY DISPERSION OF PRECIPITATING IONS AT HIGH LATITUDES

A. Introduction

Particle dispersion signatures, usually identified from energy-time spectrograms measured by satellites, have been found at various places of the magnetosphere-ionosphere system. Many researchers have demonstrated that ion dispersion signatures can provide unique insights for inferring the possible remote plasma source and transport mechanism of an observed particle population (Reiff et al., 1977; Quinn and McIlwain, 1979; Quinn and Southwood, 1982; Williams 1981; Klumpar et al., 1983; and Winningham et al., 1984; Greenspan et al., 1985; Bosqued et al., 1986). Because of the growth in high resolution ion observations at both low (ionospheric) altitudes and in the magnetospheric tail, research on the origin and morphology of precipitating auroral ions has been active and productive in recent years (Hardy et al., 1988; and references therein). In this paper, we describe the ion dispersion events found at the nightside, high-latitude boundary of the precipitating ions observed by DMSP satellites. The primary motivation for this work is to investigate the relationship between the ion dispersion found at the DMSP altitude (840 km) and the plasma sheet boundary layer (PSBL) observed by Eastman et al. (1984) in the near magnetotail (15-20 R_E). The PSBL may play an important role in magnetospheric dynamics, particularly in substorm processes (Rostoker and Eastman, 1987; Eastman et al., 1988).

Interpretations of ion dispersion seen in near-earth auroral observations suggest that both ionospheric and magnetospheric ions are important sources in the nightside auroral precipitation. Winningham et al. (1984) and Frahm et al. (1986) have reported banded ion beams in the central plasma sheet (CPS) observed by Dynamics Explorer satellites. The observed ion bands exhibit a characteristic dispersion of a decreasing energy with decreasing magnetic latitude. The authors suggested that upgoing ionospheric ions (primarily O+) from the opposite hemisphere are the source of the ion bands. In their model, outflowing energetic ion beams are injected onto boundary plasma sheet (BPS) field lines by the upward parallel electric field associated with electron inverted-Vs, undergo E x B convection (toward lower latitudes) and contribute to the formation of ion bands with dispersion in the conjugate hemisphere, CPS region.

Another example is the energy-time dispersion of bouncing ion clusters reported by Quinn and McIlwain (1979) from observations made by the geosynchronous ATS satellite. Analysis shows that the observed dispersion of the ion clusters can result from the velocity-dependent, bounce motion of the ions (Quinn and McIlwain, 1979; Quinn and Southwood, 1982). From the energy-time of flight dispersion signature and the changing phase of the bouncing ion cluster, they can determine the species and the injection location of the ion cluster. They concluded that a localized ion injection, set up by accelerations during a transient convection surge at the geosynchronous altitude, can contribute to the precipitating ion population on the night side auroral zone.

The above examples illustrate that in order to establish the reality of dispersion in an observed ion population and, in turn, to use the dispersion structure as a diagnostic tool, it is necessary to consider three critical elements: the properties of the ion source (e.g., steady or transient, spatial location, and energy spectrum); the satellite orbital configuration that both provides and limits the observational capability; and the ion transport processes, such as field-aligned motion or cross-field ion drift, between the observer and source region.

In this paper, we expand upon our earlier report (Yeh et al., 1986) on ion energy dispersion events of nearly field-aligned ions observed in the energy range between 30 eV and 30 keV from the non-spinning, circularly orbiting, low altitude DMSP satellites. The events occur at the high latitude edge of the precipitating ion distribution, often with the characteristic structure that the particle energy decreases with decreasing latitude. Similar observations have been reported by Kovrazhk'n et al. (1987) though their interpretations differ from ours as brought out in the discussions below.

B. DMSP Orbits and Particle Detectors (SSJ/4)

The F6 and F7 DMSP satellites are in sun-synchronous, circular, polar orbits at 840 km. The satellites have an orbital period of approximately 101 minutes and a speed of about 7.5 km/sec. The DMSP F6 orbit is approximately in the dawn-dusk meridian and F7 in the 10:30 -

22:30 MLT meridian plane. Due to the diurnal rotation of the geomagnetic pole about the geographic pole, both satellites obtain wide spatial coverage in magnetic local time (MLT) and geomagnetic latitude (MLAT). The data used in this paper are mainly from the the SSJ/4 particle detectors flown on F6 and F7, that are identical in design. Electron and ion flux are measured in 20 energy channels in the range from 30 eV to 30 keV. Complete 20 point electron and ion spectra are taken once per second. The SSJ/4 sensors are mounted on the non spinning satellites with fixed look directions radially outwards from Earth at all times. At high latitudes, the detectors measure essentially the magnetic field-aligned precipitating electrons and ions.

C. Ion Dispersion Events (12 Day Survey)

We determine ion dispersion events by the following criteria: 1) The dispersion must be seen in at least four consecutive energy channels above 2 keV. 2) The dispersion must persist for at least 10 seconds corresponding to about 75 km in spatial extent along the satellite track. 3) The dispersion is at the most poleward region of the ion precipitation in the auroral zone. 4) The energy of the enhanced ion flux that is the signature of the dispersion event decreases with decreasing latitude (i.e., equatorwards). The first two criteria insure that the dispersion event has substantial structure. The third is a consistency requirement in associating the ion dispersion signature at low altitudes with the poleward boundary of the magnetospheric precipitating particle distribution. The fourth criterion is suggested by the expectation that at the polar cap boundary the low altitude convection generally proceeds from higher to lower latitudes. This criterion is useful and fits all of the observations reported by Kovrazhkin et al (1987), though we have observed that the dispersion signature may also occur in the opposite direction (i.e., increasing energy with decreasing latitude). Many dispersion events occur poleward of distinct electron inverted-V events. The electron spectra indicate that there are no large field-aligned potential drops (> 1-2 keV) in the region of the ion dispersion event itself.

Using these criteria, we examined all auroral transits ($\approx$ 600) of the DMSP F6 and F7 satellites during 12 days in December 1983. The 12 days surveyed included the most quiet and the

most disturbed days of the month with a Kp range of 0 to 6. A total of 80 ion dispersion events were identified from the north and south pole crossings in the MLT range from 18:00 to 03:00 (through midnight). Two events have been chosen to characterize the observed dispersion.

Figure 39 presents the spectrograms of the large-scale particle precipitation patterns during two dusk auroral transits that encompass the two chosen ion dispersion events. The particle directional, differential number fluxes (electron at top; ion at bottom) are color-coded as a function of energy (ordinate) and universal time in hours and minutes (abscissa). Also listed at two minute intervals are the magnetic latitude (MLAT), magnetic longitude (MLON), and the magnetic local time (MLT) of the satellite mapped down the magnetic field line to an altitude of 110 km. The particle spectra at the left were observed during the north polar pass of DMSP F6 on 10 December 1983 between 36000 sec (10:00) and 36480 sec (10:08) UT, and those at the right, the pass on 31 December 1983 between 58020 sec (16:07) and 58500 sec (16:15) UT. From left to right, DMSP F6 exited from the polar cap and encountered the poleward edge of the evening side auroral oval at approximately 75° MLAT and 20.4 MLT for the December 10 pass. The F6 satellite traveled across the poleward boundary of the auroral oval at aproximately the same MLAT but at a later magnetic local time (23.3 MLT) for the pass on 31 December.

In each of the two crossings an inverted-V can be identified in the electron spectrum, which serves to separate the central plasma sheet (CPS) electrons on the equatorward side from the boundary plasma sheet (BPS) electrons on the poleward side. The BPS electrons are of low energy and very intense, as indicated by the pink color, for both passes. The electron inverted-V of the December 10 pass, which occurred between 1003:48 and 1004:13 UT, is narrow (1°) and with peak potential of ~3kV. The inverted-V of the December 31 pass, which occurred between 1610:25 and 1613:20 UT, has a broader extent (6°) and a much larger peak potential of ~30 kV. The magnitude and spatial extent of an inverted-V structure may vary significantly with magnetospheric activity [*Lin and Hoffman*, 1979] and the interplanetary magnetic field (IMF) polarity. The relative spatial scale and intensity level among the BPS, inverted-V and CPS are also controlled by these magnetospheric and IMF conditions. Electron spectra from the December

31 pass are considerably harder than those from the December 10 pass throughout the whole auroral transit.

The available IMF [*Couzens and King*, 1986] and auroral electroject (AE) data show that the two dispersion events occurred under the following geophysical conditions:

	December 10	December 31
Kp	4+	4
AE	412	959
IMF B$_{tot}$	11.2	5.5
IMF Bz	-2.7	-3.9
IMF By	+10.6	-2.5

Of particular interest is the difference in the sign of IMF By for the two cases.

As shown in the bottom panels of Figure 39, the energy spectra of the precipitating ions colocated with the BPS electrons can be described approximately as a region of ion flux enhancement with an energy of a few keV superimposed upon a region of intense low-energy ions (<1 keV). The two-component spectral feature of the ions fades out with increasing UT. Here, we are only interested in the characteristics of the keV precipitating ion group. The origin of the low-energy precipitating ions is outside the scope of this paper. The most distinct feature of the precipitating keV ion energy spectrum colocated with the BPS electrons is the nearly monoenergetic ion flux enhancement centered at a specific energy channel. The spectral feature of the flux enhancement over a narrow energy range is indicative of an ion beam. Thus, in the bottom panels of Figure 39, an intense ion beam of ~4.4 keV is seen at 1003:05 UT on December 10, and an ion beam of ~6.5 keV is seen at 1609:20 UT on December 31. These energies are representative of those found in the tail for the earthward streaming PSBL ion beams [*Eastman et al.*, 1984]. It is the lower bound of the keV ion flux enhancement that shows a dispersive signature in time (decreasing energy with increasing UT) and space (decreasing energy with decreasing MLAT and MLT). The ion dispersion occurs between 1002:45 (36165 sec) and 1003:20 (36200 sec) UT on December 10, and occurs betwen 1608:25 (58105 sec) and 1609:30

Figure 39. Color spectrograms of DMSP F6 precipitating electrons (top) and ions (bottom) on 10 December (left) and on 31 December 1983 (right). The flux levels are given by the color bars in particles per (cm2 s se eV). The flux is shown for given energies as a function of universal time (UT), magnetic latitude (MLAT), magnetic longitude (MLON), and magnetic local time (MLT), mapped to 110 km altitude. Arrows mark the two in energy (> 2 keV) dispersion structures seen at the poleward poriton of the auroral region.
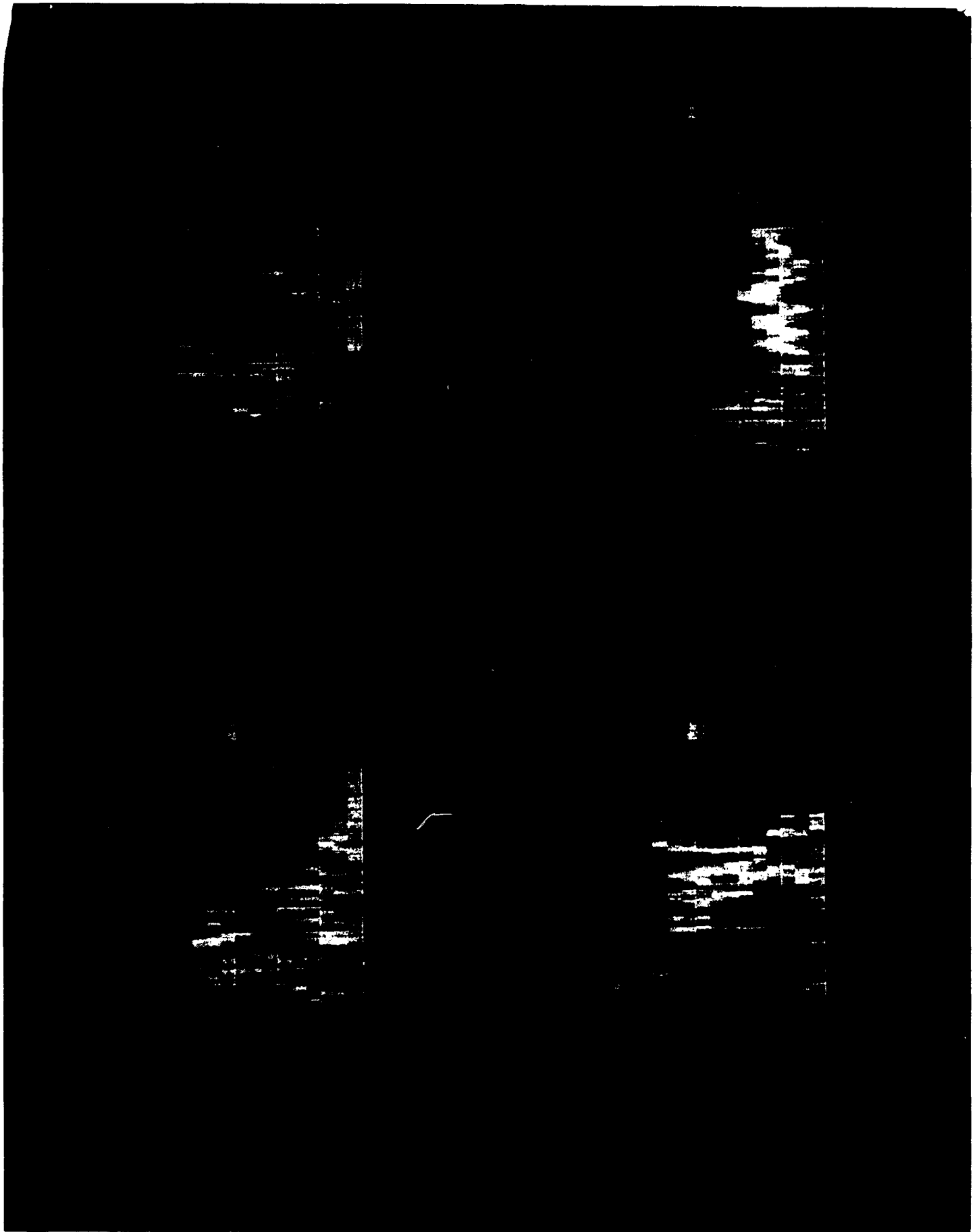
(58170 sec) UT on December 31. A quantitative description of these dispersion events will be presented in Section E.

D. Interpretation of Ion Energy Dispersion Events

In this section we present simple interpretations that may account for the observed ion energy dispersion events. Since DMSP satellites measure principally precipitating ions with small pitch angles and field-aligned ion beams are plentiful in the PSBL (Eastman et al., 1984), in all cases, we interpret the dispersion events to be the low altitude signature of injected, near field-aligned plasma from the tail. Model assumptions are: 1) The source particles have near zero pitch angles (i.e., near or inside the loss cone) with the energy distribution $f(E)$. 2) The time scales for variations in the magnetospheric electric field (E) and magnetic field (B) are greater than the travel time ($\leq 1/4$ of the bounce period) of protons from the source distance to the DMSP altitude (say, about 2 minutes). 3) The $E \times B$ convection is the dominant cross-field proton motion, i.e., curvature and gradient drifts are neglected. 4) There is no parallel electric field ($E \cdot B = 0$) so that magnetic field lines are equipotentials. The conditions 3 and 4 insure that the frozen-in-flux concept is valid.

Figure 40 schematically illustrates the basic conditions that would produce a low altitude dispersion signature. Protons with the energy distribution, $f(E)$, are injected into a magnetic flux tube that extends the distance, d, from the injection point to the DMSP altitude. Particles attached to the flux tube undergo both field-aligned motion and a cross-field drift at the field line convection rate. The dashed curve in Figure 39 delineates the drift path of the convecting ionospheric footprint of the magnetic flux tube that contains the injected particles. A higher energy (E_i in the figure) particle arrives at the low altitude earlier (time T_i) than a lower energy (E_j) particle (time T_j). Particles of different energy (E) are spread in arrival time (T) and corresponding low altitude spatial location ($\underline{X}$) because of the flux tube motion along the ionospheric convection path. The bottom panel of Figure 40 shows the basic energy-time (and energy-position) dispersion expected by the model.

$\{f(E), T_0\}$

DRIFT PATH
(HIGH ALTITUDE)

E_j

E_i

d

E_j

E_i

DRIFT PATH
(LOW ALTITUDE)

E_i

$(T_0, \underline{X}_0)$

$(T_j, \underline{X}_j)$ $(T_i, \underline{X}_i)$

SATELLITE

ENERGY (E)

$\Delta T \propto E^{-1/2}$

E_i

E_j

TIME (T) T_j T_i T_0

POSITION ($\underline{X}$) $\underline{X}_j$ $\underline{X}_i$ $\underline{X}_0$
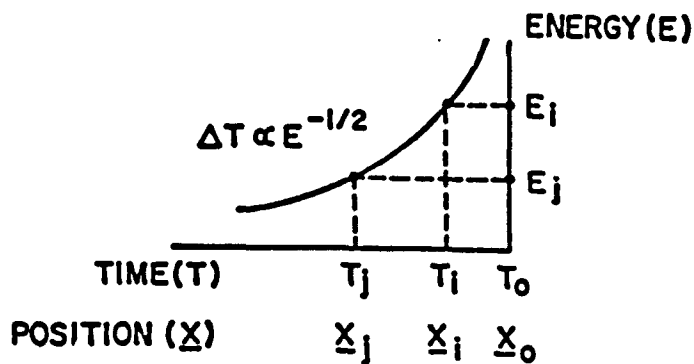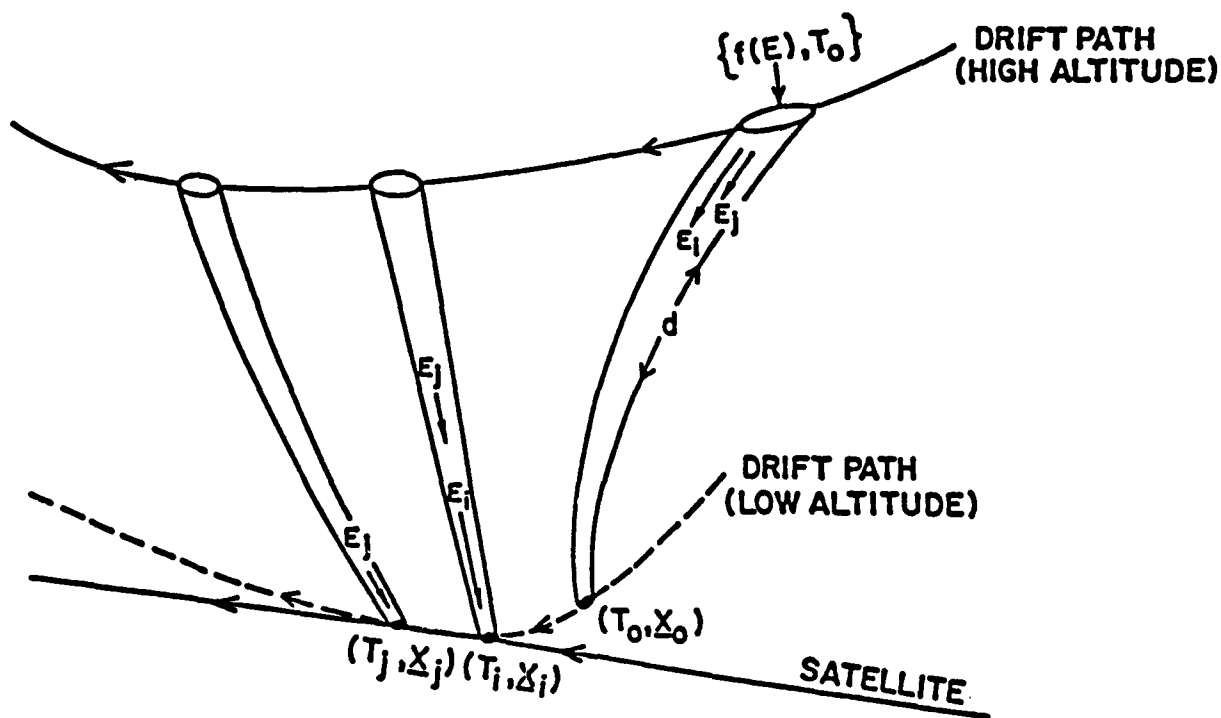
Figure 40. Model illustration of ion energy dispersion (top panel) resulting from the magnetic-field-aligned velocity filtering and cross-field $\mathbf{E} \times \mathbf{B}$ drifting. $\{f(E), T_0\}$ denotes the particle energy distribution function and onset time of an injection event at a source region which is located at a magnetic-field-aligned distance (d) from the DMSP satellite. (T_i, X_i) denotes the arrival time and the position of a particle (with energy E_i) at low altitude along a convection stream line (dashed curve). The satellite (with velocity, V_{sat}) track overlaps a portion of the particle low altitude drift path. The arrival time of a particle at low altiude is inversely proportional to the square root of the particle energy (bottom panel).

130

In addition to the extent ΔX along the low altitude drift path, the dispersion zone will also extend a distance ΔY in the orthogonal direction. ΔY would be the low altitude mapping of the thickness of the PSBL. A reasonable estimate is

$$\Delta Y \leq 125\ km \tag{1}$$

The upper limit in (1) corresponds to the generous choice of parameter values of a PSBL thickness of 1 R_E, cross tail dimension 30 R_E, and magnetic intensity 30 nT mapped into a ring of 4p/3 radians at 840 km, and may exceed the actual extent ΔY by about a factor of 2.

The interpretation of the actual low altitude dispersion signature depends upon the nature of the PSBL ion injection in space and time. Three illustrative cases are discussed.

(i) <u>Impulsive injection at a point ($\Delta t \cancel{E}\ 0$).</u> If the PSBL injection of particles with the distribution function $f(E)$ is local and abrupt ($\Delta t\cancel{E}0$), the dispersion is restricted to a single flux tube. In order to observe the event at low altitudes, the satellite must encounter the flux tube at exactly the right time and move exactly with the flux tube drift rate. From the observed low altitude dispersion curve, the onset time (T_0) and distance (d) to the location of the PSBL injection event are given by

$$d = (T_j - T_i)\ /\ (V_j^{-1} - V_i^{-1}) \tag{2}$$
$$T_0 = T_i - d/V_i \tag{3}$$

where V_i and V_j are the speeds along the field line. If V_c is the local convection velocity, the dispersion occurs approximately over the distance $V_c\ (T_j - T_i)$ along the low altitude drift path of the flux tube.

The conditions needed to observe the low altitude dispersion for such impulsive PSBL injection are severe and probably unrealistic. Even if the satellite should fortuitously arrive at the flux tube at the proper time, the condition of equal satellite and convection velocity (about 7.5 km/s) would require an anomalously large electric field (about 300 mV/m).

(ii) <u>Sustained injection at a fixed position.</u> If the injection of the PSBL particles $f(E)$ is sustained in time (Δt large) at a fixed position, the energy dispersion appears as a fixed spatial structure at low altitudes, extending in longitude and latitude along the local convection drift path.

131

Particles with energy E_i will always arrive at the ionosphere at position X_i, for the duration Δt. As long as the satellite and convection velocity are not orthogonal, the energy dispersion will be observed if the satellite encounters the proper convection path. The likelihood of observing the low altitude dispersion would be larger when the satellite and convection tracks are closely parallel. Since the satellite passes through a fixed spatial structure, the source distance (d) could be estimated from the local convection velocity but not from the relative satellite encounter times (T_i and T_j) of the observed energy dispersion event. The requirements and conditions for case (ii) are similar to those used by Reiff et al. (1977) to produce the convection driven ion dispersion signature poleward of the last closed field line in the polar cusp.

(iii) Impulsive injection along a magnetic shell. If the injection of particles $f(E)$ is abrupt ($\Delta t \neq 0$) but along an injection curve (such as an extended portion of the PSBL that defines a sheet of magnetic field lines or a magnetic shell) then the low altitude dispersion signature will differ significantly from cases (i) and (ii). Here the dispersion will develop in *time* along the convection drift path of the low altitude mapping of the injection curve. If the latter mapped injection curve falls along a single low altitude streamline, the dispersion will develop in time along the local convection path. In order to observe the energy dispersion in time, $E(T)$, the satellite must move along or across the proper drift path at the proper time. An observed dispersion event would begin as the satellite encounters the proper convection path at time T_i with particle energy E_i and terminate at the later time T_j at the lower particle energy E_j. For practical purposes, the end of the event occurs when the satellite moves out of the drift path or when criterion 1) of section 3 is exercised. Source parameters d and T_0 are determined by equations (2) and (3) as in case (i), assuming that these parameters are unique along the injection curve. As in case (i), T_i is the arrival time of source particles of speed V_i at position X_i along the low altitude dispersion path.

Case (iii) is similar in concept to the impulsive injection boundary model used by Strangeway and Johnson (1983) to explain an ion energy dispersion event observed by the SCATHA satellite in near geosynchronous orbit. In their work, particles with essentially a 90° pitch angle originating at the Mauk and McIlwain (1974) injection boundary produced the desired

modelled dispersion. In case (iii) the particles with essentially zero pitch angle injected at the PSBL would be responsible for the modelled dispersion. Case (iii) may also be involved during magnetospheric substorm activity (Rostoker and Eastman, 1987).

In each of the three models, the low altitude observations may be used to estimate the source distribution. If the observed dispersion event extends over the energy range ΔE_{disp} and E_i is an observed energy in this range, then by Liouville's theorem the observed and source distribution functions are equal:

$$f_{source}(E_i) = f_{obs}(E_i) \qquad (4)$$

Of course, only the near-zero pitch angle portion of the source distribution would contribute to the observed distribution at the 840 km DMSP altitude (about $1.5°$ for a tail field of 25 nT, and in the absence of loss cone filling interactions along the flux tube).

E. Quantitative Analysis of Two Characteristic Events

In this section, we investigate quantitative aspects of the two "typical" ion dispersion events described in Section 3. Displayed in the top panels of Figures 41 and 43 are three-dimenstional stack plots for the events, illustrating variations of the differential energy flux (z-axis) of the precipitating ions as a funciton of energy (x-axis) and universal time with the corresponding magnetic latitude and local time (y-axis). For measurements made by an electrostatic analyzer, the differential energy flux $[E j(E)\Delta E]$ (in eV/cm^2s sr)is proportional to the particle count rate. We chose the differential energy flux for illustration to emphasize the high energy (keV) ion precipitation.

The top panel of Figure 41 shows that the DMSP F6 satellite traveled from north to south at nearly a constant magnetic longitude (~20.25 MLT) from 36150 sec (1002:30) to 36225 sec (1003:45) UT on December 10. Flux enhancement within a finite energy range is seen at various energy channels (E_i) between 36168 sec and 36196 sec UT. In all energy channels above 1.4 keV, the arrival of the maximum flux can be identified, which shows the dispersion feature with the higher energy particles arriving earlier (and at higher MLAT) than the lower energy particles.
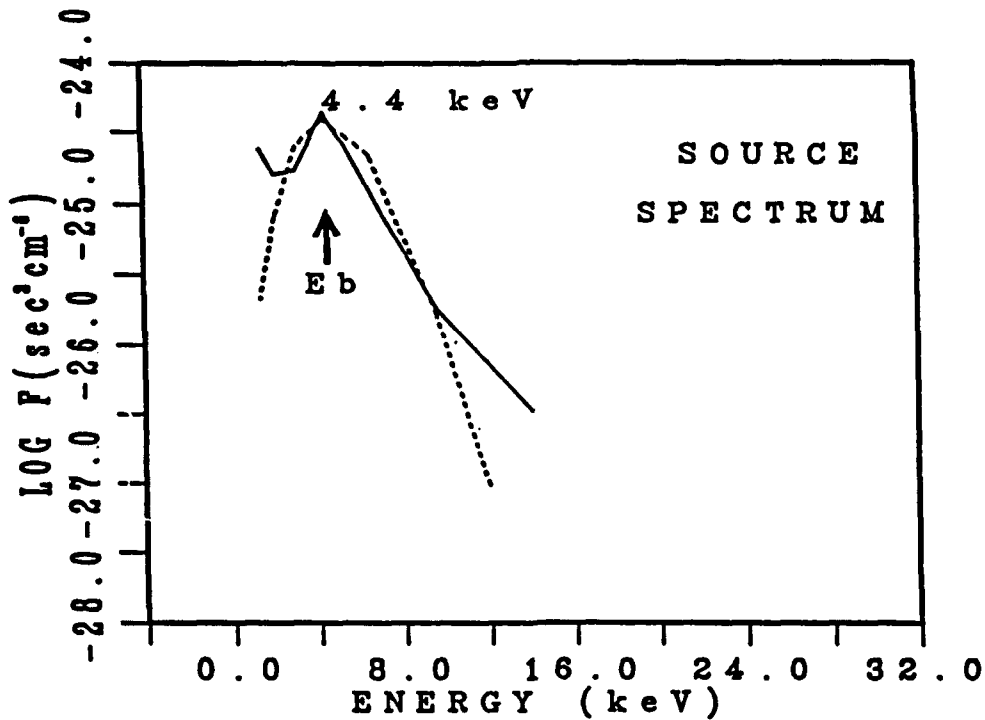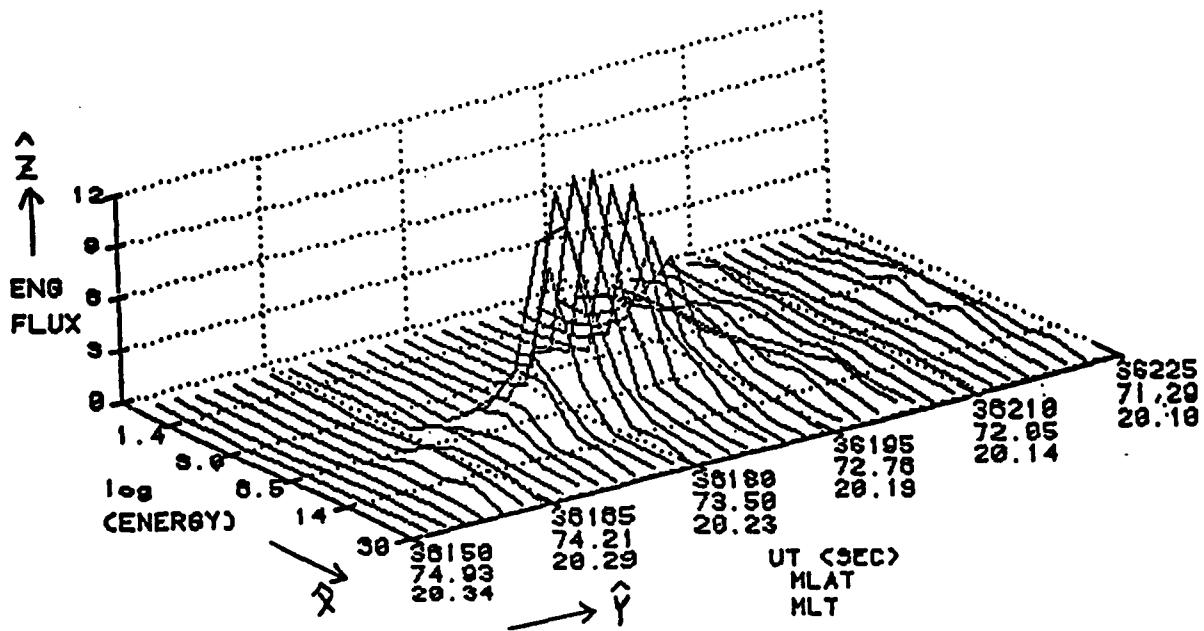
Figure 41. Top panel: An expanded plot to illustrate the energy flux (in eV/cm^2 s sr) variations with ion energy (in keV), time (in s UT), magnetic latitude (MLAT) and magnetic local time (MLT) for the ion dispersion event on 10 December, 1983. The dispersive locations and arrival times of the energy flux enhancement centered at E_i (E_i=14 to 2 keV from high to low) are seen between 36170 s UT and 36195 s UT. Bottom panel: The inferred source distribution function f(E) (solid curve). f(E) is beam-like, and can be approximated by a drifting Maxwellian distribution function with a beam energy (E_b) of 4.4 keV (dashed curve).

The set of observed values $(E_i; T_i; MLAT(i); MLON(i))$ obtained from the top panel of Figure 41 and the corresponding values of $f_{obs}(E_i)$ are listed in Table 19.

Table 19. December 10 despersion parameters.

E (keV)	Time (s UT)	MLAT (deg.)	MLON (deg.)	fobs (ions/cm^{6}sec^{-3})
14.04	36168	74.08	216.8	3.33×10^{-27}
9.58	36175	73.74	216.4	1.83×10^{-26}
6.50	36181	73.45	216.0	1.22×10^{-25}
4.42	36185	73.26	215.8	4.39×10^{-25}
3.05	36193	72.87	215.4	1.70×10^{-25}
2.06	36196	72.73	215.4	1.58×10^{-25}

Using equation (4) and Table 19, the source distribution function f(E) is calculated and shown (solid line) the bottom panel of Figure 41. If approximated by a streaming Maxwellian (dashed line), the source spectrum is beam-like with a peak or beam energy of about 4.5 keV, or a proton speed of 928 km/s, with a low temperature and density of 300 eV and 0.03 cm^{-3}, respectively. These spectral values are similar to those of PSBL ions observed at about 15-20 R_E (*Eastman et al.*, 1984).

If case (iii) - impulsive injection along a magnetic shell at high altitudes - is responsible for producing the low altitude dispersion, using equations (2) and (3) and the observed values $(E_i; T_i)$, the onset time is found to be about 36151 s UT and the distance to the source only about 5 R_E which may be a distance too small to identify with PSBL injection.

However, if the dispersion is a spatial structure as in case (ii) resulting from the steady injection of particles at a fixed position (i.e., the poleward edge of the PSBL), we can estimate the source distance by

$$d = [MLAT(j)-MLAT(i)] / [V_c cos\beta (V_j^{-1} - V_i^{-1})] \tag{5}$$

where [MLAT(j)-MLAT(i)] is the length along the dispersion track between latitudes j and i, and the contribution from MLON is ngelected. V_i and V_j are again the particle speeds along the field lines, β is the angle between the low altitude convection velocity and the satellite track, and V_c is the low altitude convection speed between positions MLAT(i) and MLAT(j). For $d \approx (15 - 20) R_E$ and small β ($\approx 0°$), equation (5) requires $V_c \approx (1.5 -2)$ km/s. A low altitude convection speed of this magnitude is large, but such magnitudes have been observed at/near the poleward boundary of the auroral oval [Yeh et al., 1988; Foster et al, 1989]. As wil be discussed below, the assumption of small β is reasonable.

For positive IMF By, the statistical convection pattern on the nightside has a distinct westward flow region poleward of the Harang discontinuity [Heppner and Maynard, 1987]. The dawn to dusk DMSP F6 satellite velocity could become closely parallel (i.e, small β) to the convection flow velocity in this region. In fact, we were able to identify a dispersion region with each of the DMSP satellite northern hemispheric crossings from 10 UT to 16 UT on 10 December, when IMF By was stably positive and strong. The DMSP orbital coverage and the locations of these dispersion events (5 from DMSP F6 and 2 from DMSP F7) are shown in the bottom panel of Figure 42. The pass marked by the arrow is the event presented in Figure 41. The Heppner-Maynard (HM) nightside convection model (in terms of 2 kV equipotential contours) at ionospheric altitudes, under positive IMF By and $3^+ \leq Kp \leq 4^-$ conditions is shown in the top panel of Figure 42 [taken from Heppner and Maynard, 1987]. If we rotated the HM pattern clockwise (toward dusk) by 1.5 hours in MLT and expanded it toward lower latitudes by 1.5 degrees, the distribution of the ion dispersion events matches well with the region of westward ion drift stream lines. It is clear from a comparison between the convection stream lines and the ion dispersion paths that the condition for small β occurs in the region of interest when the IMF By is strongly positive. Thus, the dispersion event in Figure 41 is more easily interpreted in terms of case (ii) - steady localized PSBL injection at a fixed position - than by case (iii). The distinct beam feature seen in the source spectrum (cf., Figure 41) is also consistent with the localized source assumption for case (ii).
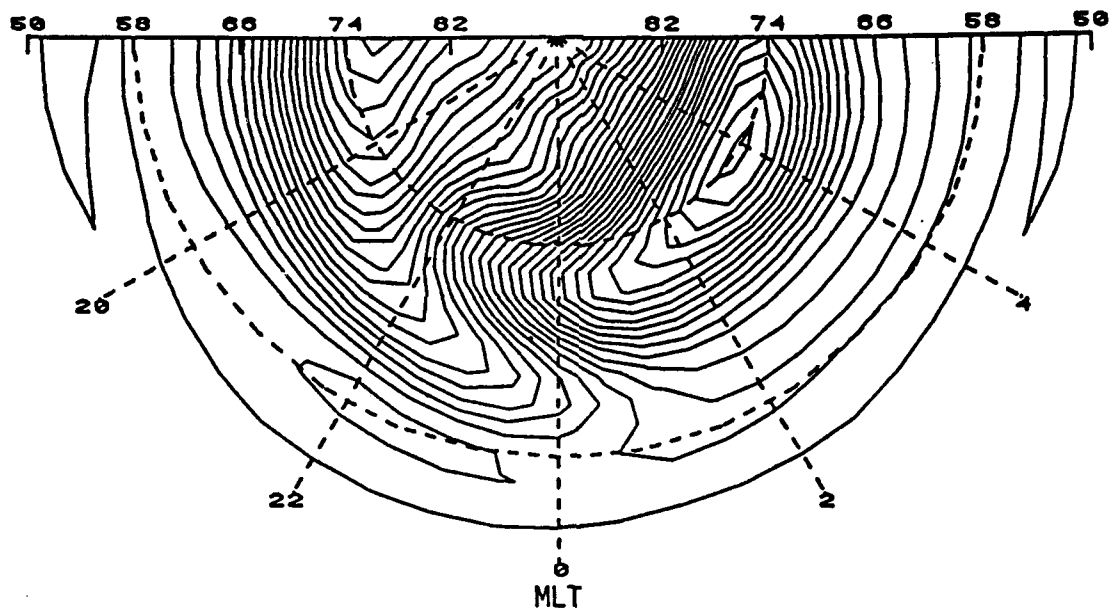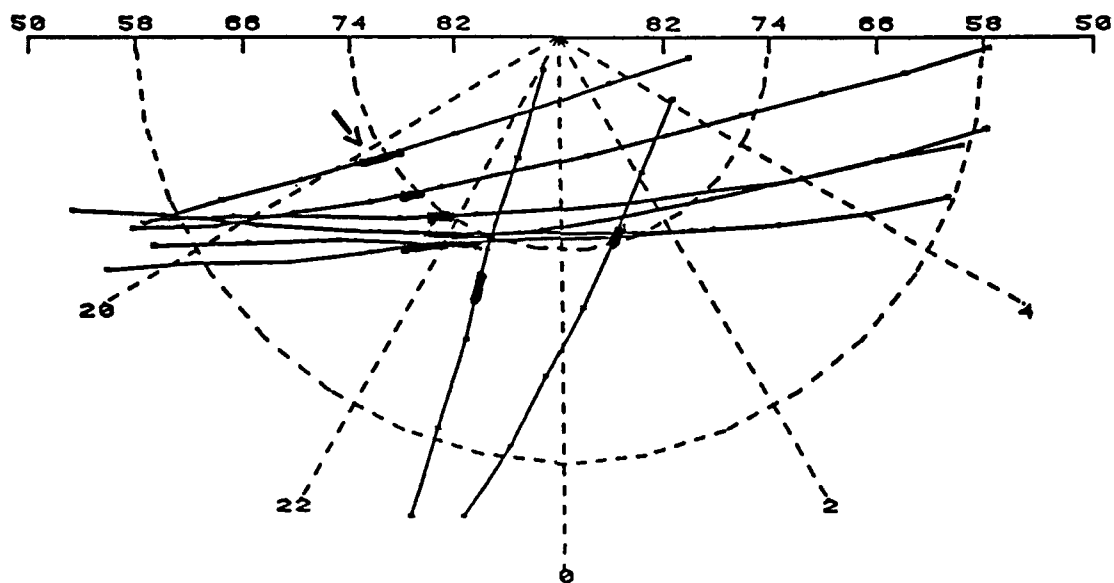
Figure 42. Top panel: Statistical ionospheric convection pattern on the nightside northern hemisphere for positive IMF By conditions [taken from *Heppner and Maynard*, 1987]. A westward flow region is noticeable in the 20-24 MLT sector and at ~74° MLAT. Bottom panel: Ion dispersion events observed by the DMSP F6 (dawn to dusk) and DMSP F7 (prenoon to premidnight) satellites in the northern hemisphere during 10 UT to 16 UT on December 10, 1983, a period of strongly positive (9-11 nT) IMF By conditions. The ion dispersion paths are approximately parallel to the ion convection velocities. An arrow denotes the event presented in Figure 41.

The characteristic features of the dispersion event on 31 December are displayed in Figure 43. Again the energy flux as a function of energy and UT (and corresponding MLAT and MLT) is shown in the top panel. The arrival of the maximum flux in all energy channels above 3 keV shows dispersion with the higher energy particles arriving earlier (and at higher MLAT and later MLT) than the lower energy particles. The dispersion feature is seen for the much longer duration between 58100 UT and 58170 UT, in the larger MLT range (22.3 - 23.3 MLT), and is associated with more energetic ions (3 - 30 keV) than those of the dispersion event on 10 December. Again, with the observed values from Figure 43 and the measured flux for the 31 December event, using equation (4) the source distribution function $f(E)$ is derived and shown (solid line) in the bottom of Figure 43. The source spectrum can still be approximated by a streaming Maxwellian (dashed line) with a bulk energy of 6.5 keV (or a proton speed of 1120 km/s), with a temperature and density of about 1 keV and 0.03 cm^{-3}, respectively. These spectral values are also representative of PSBL ions at 15 - 20 R_E. The beam feature of the source spectrum is less pronounced, as reflected in the higher temperature, than that of the 10 December event.

Using equations (2) and (3) and the observed values of $\{T_i; E_i\}$ we find that the onset time of the injection T_0 is about 58060 s UT and the average source distance $<d>$ is about 17.5 R_E, which is a reasonable distance for a source associated with the ion beams in the PSBL. Thus, the characteristics of the 31 December event may be explained in terms of the energy-time of flight dispersion of case (iii) - impulsive PSBL ion injection along an extended spatial region.

F. Summary and Discussion

Precipitating ions (2 keV - 30 keV) at DMSP altitudes on the poleward edge of the nightside auroral oval exhibit a dispersion in energy that we interpret to be the low altitude signature of ion beams originating in the PSBL at about 15 - 20 R_E. The PSBL ion motion is assumed to consist simply of streaming along the magnetic flux tube along with an E X B drift.

Two events were chosen from a survey of 80 ion dispersion events to characterize the observed dispersion. We analyzed the two events and estimated the distance and energy spectrum
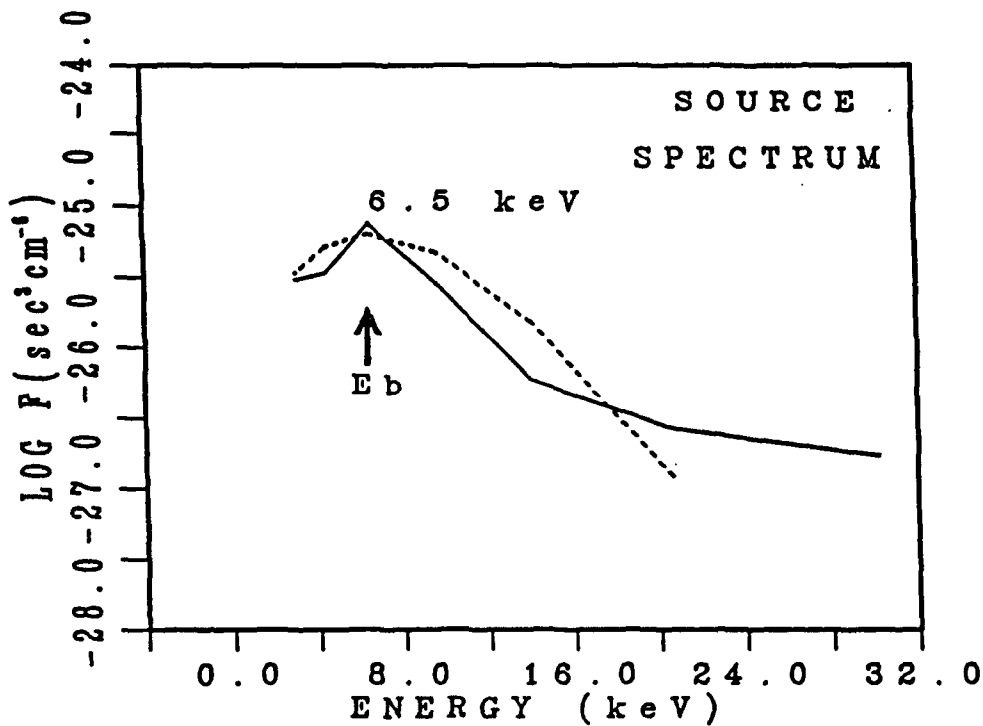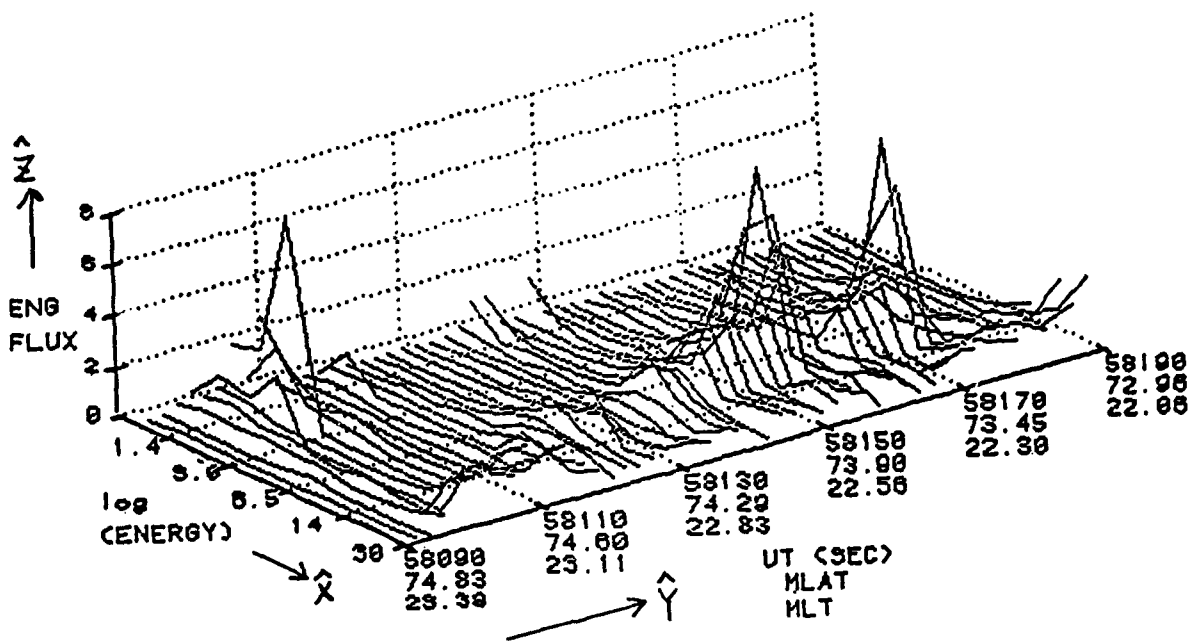
Figure 43. Same as for Figure 41, but for the ion dispersion event on 31 December 1983. Top panel: The dispersive arrivals of the maximum flux in all energy channels above 3 keV are apparent during 58100s UT to 58160 s UT. Dispersion features are seen for a longer duration and over a wider MLT range than those in Figure 41. Bottom panel: The source spectrum is approximated by a drifting Maxwellian with a beam energy (E_b) of 6.5 keV.

of the source particles from the observed ion dispersion arrival times and spatial locations. Findings were consistent with the simultaneous IMF and geophysical conditions that relate to the convection electric field pattern.

Simple interpretations were suggested, though no comprehensive model developed, to demonstrate how characteristics of the observed low altitude dispersion might depend upon conditions at the PSBL (cases i to iii, Section D). Two events (on 10 December and 31 December 1983) were presented as characteristic of the low altitude observations of the ion dispersion in energy. The interpretations of the events required different PSBL conditions. The first (10 December) suggested the observed dispersion resulted from ion injection at a fixed position of the PSBL. The second (31 December) suggested impulsive PSBL ion injection along a magnetic shell. *A model that uniquely or unambiguously relates the observed low altitude dispersion to the PSBL is not in hand.* The definitive finding in this paper is observational: precipitating ions at the poleward edge of the auroral oval at DMSP altitudes often exhibit a characteristic dispersion in energy. These dispersion features relate to the dynamics and distribution of the ion beams uniquely situated in the plasma sheet boundary layer.

REFERENCES

Bosqued, J.M., J.A. Sauvaud, D. Delacourt, and R.A. Kovrazhkin, Precipitation of suprathermal ionospheric ions accelerated in the conjugate hemisphere, *J. Geophys. Res., 91,* 7006, 1986.

Couzens, D.A. and J.H. King, Interplanetary medium data book-Supplement 3A, 1977-1985, *Rep. NSSDC/WDC-A-R&S 86-04a, Natl. Space Sci. Data Cent,* NASA Goddard Space Flight Center, Greenbelt, MD., 1986.

Eastman, T.E., L.A.. Frank, W.K. Peterson and W. Lennartsson, The plasma sheet boundary layers, *J. Geophys. Res., 89,* 1553, 1984.

Eastman, T.E., G. Rostoker, L.A. Frank, C.Y. Huang, and D.G. Mitchell, Boundary layer dynamics in the description of magnetospheric substorms, *J. Geophys. Res.,* 93, 14, 411, 1988.

Foster, J.C., H.-C. Yeh, R.A. Eastes, and F.J.Rich, Radar/satellite observations of nightside auroral boundaries, *EOS Tran. AGU, 70,* 1239, 1989.

Frahm, R.A., P.H. Reiff, Winningham, J.D., and J. L. Burch, Banded ion morphology: Main and recovery storm phases, in *"Ion Acceleration in the magnetosphere and Ionosphere",* edited by Tom Chang, AGU series, *Geophys. Monograph 38,* 98-107, 1986.

Greenspan, M.E., D.J. Williams, B.H. Mauk, and C.-I. Meng, Ion and electron energy dispersion features detected by ISEE 1, *J. Geophys. Res., 90,* 4079, 1985.

Hardy, D.A., M.S. Gussenhoven, and D. Brautigam, A statistical model of auroral ion precipitation, *J. Geophys. Res.,* 94, 370, 1989.

Heppner, J.P. and N.C. Maynard, Empirical high-latitude electric field models, *J. Geophys. Res., 92,* 4467, 1987.

Klumpar, D.M., W.K. Peterson, E.G. Shelley and J. M. Quinn, Localized ion injection outside the cusp, *EOS, Trans. Am. Geophys. Union, 64,* 297, 1983.

Kovrazhkin, R.A. Zh. M. Boske, L.M. Zelenyi and N.V. Georgio, Observation of evidence of reconnection and plasma acceleration at a distance of about 5 x 10^5 km in the tail of the earth's magnetosphere, *JETP Lett., 45,* 479, 1987.

Lin, C.S., and R.A. Hoffman, Characteristics of the inverted-V event, *J. Geophys. Res., 84,* 1514, 1979.

Mauk, B.H. and C.E. McIlwain, Correlation of Kp with the substorm-injected plasma boundary, *J. Geophys. Res., 79,* 3193, 1974.

Quinn, J.M. and C.E. McIlwain, Bouncing ion clusters in the Earth's magnetosphere, *J. Geophys. Res., 84,* 7365, 1979.

Quinn, J.M. and D.J. Southwood, Observations of parallel ion energization in the equatorial region, *J. Geophys. Res., 87,* 10,536, 1982.

Reiff, P.H., T.W. Hill and J.L. Burch, Solar wind plasma injection at the dayside magnetospheric cusp, *J. Geophys. Res., 82,* 479, 1977.

Rostoker, Gordon and Tim Eastman, A boundary layer model for magnetospheric substorms, J. Geophys. Res., 92, 12,187, 1987.

Strangeway, R.J. and R.G. Johnson, Mass composition of substorm-related energetic ion disperison events, *J.Geophys. Res., 88,* 2057, 1983.

Williams, D.J., Energetic ion beams at the edge of the plasma sheet: ISEE 1 observations plus a simple explanatory model, *J. Geophys. Res., 86,* 5507, 1981.

Winningham, J.D., J.L. Burch and R.A. Frahm, Bands of ions and angular V's: A conjugate manifestation of ionospheric acceleration, *J. Geophys. Res., 89,* 1749, 1984.

Yeh, H.-C., N.C. Heinemann, R.L.Carovillano, M.S. Gussenhoven and D.A. Hardy, Energy dispersion of precipitating auroral ions, EOS. Trans. AGU, 67, 1159, 1986.

5. COMPUTER BASED DATA ANALYSIS AND PROJECTS

A. Introduction

An important contract task was to provide computer support for scientists utilizing Air Force particle data to address topics such as auroral activity, radiation belt modelling, the effects of solar events, and other considerations relating to sun-earth interactions. Projects undertaken are detailed below by satellite and project.

B. DMSP Projects

The DMSP data base that is widely and routinely used has been assembled from seven satellites. The data set spans the time from September 1977 until the present, with a data gap from March 1980 to October 1982. Table 20 lists the satellites, instruments, and time of operation in the DMSP series.

Table 20. DMSP satellites.

SATELLITE	INSTRUMENT	START	END
F2	J3	SEP 77	FEB 80
F4	J3	JUN 79	FEB 80
F6	J4	NOV 82	JUL 87
F7	J4, J*	NOV 83	JAN 88
F8	J4	JUL 87	PRESENT
F9	J4	JAN 88	PRESENT
F10	J4	DEC 90	PRESENT

Each DMSP satellite is approximately in a circular orbit at 840 km altitude. The local time coverage varies among the satellites. The satellite detectors look radially outward and at high latitudes measure predominately precipitating particles. Characteristics of the three principal detectors are:

J3 - low energy electrons, in 16 channels ranging from 48eV to 20keV.

J4 - low energy electrons and ions, each in 20 channels ranging from 32eV to 30keV.

J* - Dosimeter, electron and proton doses and fluxes in the range 1-100 MeV.

The DMSP particle data are stored on 9-track tapes that are written in blocks of binary code that are most compatible with the CDC-CYBER NOS operating system (60 bit words). Each tape usually has five files, each file being a half-month of data for J4, and a full month for J3 and J*. Listings of the tape numbers and the files contained are available on-line in a public account. Software exists that will read the tapes to disk without unpacking the data. The NOS operating system has unlimited file size for temporary storage but a limit of approximately 5 mega-bytes for permanent files, along with a practical limit of total disk space. As an example, a day of J4 data is approximately 2 mega-bytes. While it is convenient to have the data on permanent disk storage allowing for more dynamic interactive processing of certain data, it is not always practical. The next section provides an example of the software and procedures used for an event study.

The February 1986 Storm. A request for February 7, 8, 9, 10 J4 and J* data was down-loaded from tape, using separate batch jobs that request a tape, extract a given day from the tape, and then write the exerpt into permanent disk space. The J4 data was a special request for 'low latitudes' (normally the data base is cut off at 45 degress magnetic latitude). This means that each day of data was approximately 4 mega-bytes. For the F6 and F7 J4 data there were 8 files totaling 32 mega bytes, and about 5 more mega-bytes for the four days of J* data. This is about as large a data set that should be dealt with on an interactive level on NOS.

With the data in place, software can be tailored to the user's needs with existing software that unpacks and displays various parts of the data file. Some common software in current use includes:

Color Spectragram	Graphically displays a pass of J4 data in 3 second average differential flux on an energy vs time scale.
Counts Listing	Lists counts for given channels over a given time interval.
Average Values	Lists average counts, fluxes, etc., given a time frame and a delta time for averaging over a given energy range, preferably into a file for future use.
Plotting Routines	Line, stack plots of any of the previous data, Flux vs time, flux vs energy, etc. Polar coordinates, orbital fluxes.

| Interpolation | J4 data has one-minute ephemerides although the counts have one second resolution. Interpolation routines can append ephemerides to any of the previous listings at the proper resolution. |
| P.C. Downloading | There is a set format that can be down-loaded to work on a PC graphics package that is popular with non mainframe users. Files are also ported over to the VAX and then sent to other sites over the SPAN network. |

These routines and others were used interactively to study the February 1986 magnetic storm. Similar event studies were made for March 1989 and for March 1991, along with many other less known events.

Long Term Studies. There are currently two projects in progress that use the complete J3 and J4 data base from September 1977 until present. One is the AURORAL BOUNDARY INDEX project and the other the POLAR RAIN INDEX project. A brief description of these projects and their status follows.

Auroral Boundary Index. The auroral boundary index effort started with an algorithm for determining the auroral boundary with the F2 satellite's J3 detector and then an updated version for the J4 detectors. Since 1985, minor adjustments have been made to the algorithm for the different DMSP satellites (F6 to F10). The recent work by Madden and Gussenhoven (1990) presents the auroral boundary index from 1983 to 1990. In the work, the equivalent midnight evening boundary is explained and presented on solar rotation plots for the designated time period. The data presented is also available on a month by month basis in a public account on the VAX for users throughout the SPAN network. The steps from algorithm to public data access are: (1) A batch job is run for each data tape (2.5 months) that as output will have five half-month listings of potential boundary ephemerides. (2) These files are merged to form one file that is processed through another program that discards certain flagged data, calculates the equivalent midnight boundary, and reformats into a simpler format. (3) Assuming that there are two satellites to be processed at any time, the previously created files are then merged by time

into another file that can then be appended to a permanent file by year. The current list of files is DAT77, DAT78, DAT79, DAT80, DAT83, DAT84, DAT85, DAT86, DAT87, DAT88, DAT89, DAT90 and DAT91. These are ASCII files and are stored on a PC hard drive and on permanent disk on NOS. Each day has on average about 50 boundaries per satellite. Each boundary includes the information: YEAR, DAY, SECONDS, POLE (N or S), SATELLITE, MLAT, MLT, and EQMLAT. Here EQMLAT stands for the equivalent midnight boundary. (4) The last step in the process is to run the previous file through a program that chooses only select evening boundaries depending on the satellite and pole and based on statistics, then recalculates the equivalent boundary with the latest set of regression values. This results in an average of about 20 boundaries per day per satellite. It is this new file that is used for the solar rotation plots and public access.

Polar Rain Index. The polar rain index consists of a number of data files created from an algorithm designed to automatically pick intervals of polar rain. Like the equatorward boundary algorithm, the data from the J3 and J4 detectors are used. The algoithm and its usage are explained by Gussenhoven and Madden (1990). The steps from algorithm to index are as follows.

1) Batch job algorithm. Batch jobs are run the same way as the equatorward boundaries. One tape may process up to five half-months of data per satellite. The output from the algorithm consists of two files: a listing of the time intervals of selected polar rain, and the 'Polar Rain Data Base'. The listing is used mainly for reference and as a type of job processing log that is eventually discarded.

2) Polar Rain Data Base. The data base consists of 25 files, each with one year of data for a particular satellite. The J3 data files are about 2 megabytes in size, and the J4 about 5 megabytes. The files are presently stored in both NOS and NOS/VE permanent disk space as direct access files, and a copy of the NOS/VE files are also stored on the MASSTOR systems that will be discussed later. The files and their notation are as follows:

YEAR	F2	F6	F7	F8	F9	F10
77	PR77F2P	-	-	-	-	-
78	PR78F2P	-	-	-	-	-
79	PR79F2P	-	-	-	-	-
80	PR80F2P	-	-	-	-	-
81	-	-	-	-	-	-
82	-	-	-	-	-	-
83	-	PR83F6P	-	-	-	-
84	-	PR84F6P	PR84F7P	-	-	-
85	-	PR85F6P	PR85F7P	-	-	-
86	-	PR86F6P	PR86F7P	-	-	-
87	-	PR87F6P	PR87F7P	PR87F8P	-	-
88	-	-	PR88F79	PR88F8P	PR88F9P	-
89	-	-	-	PR89F8P	PR89F9P	-
90	-	-	-	PR90F8P	PR90F9P	-
91	-	-	-	PR91F8P	PR91F9P	PR91F10

Each file consists of 366 records (daily averages). Each record contains the information: YEAR, DAY, DAT (2,4,5,41). The DAT arguments 2, 4 and 5 describe the location (POLE, MLAT by MLT); and 41 stands for the daily average counts found in that location for electrons (1 to 20) and ions (21-40). The 41 is the total number of observations in the given location.

3) Polar Rain Interface. The Polar Rain Interface is the software that was developed while deriving the polar rain index. The polar rain count levels from different satellites contain instrumental subtleties, and the ion data has not been fully studied. In order to get meaningful flux counts and/or spectra for a given day, the data has to undergo further massaging. Each satellite has its own high energy background removal that is done at the count level, then the data is merged, bin by bin to normalized F7 counts. A different seasonal baseline removal for each pole may be applied as well. An interactive routine is available for the procedure. The standard output from this routine is in three files. The format of the three files is as follows:

(a) Flux File - YEAR, DAY,SECOND, NJTOT, NJTOTB, SJTOT, SJTOTB, RAT

YEAR	= year (88, 89, 90,....)
DAY	= julian day (1-366)
SECOND	= U.T. seconds, always 43200 (middle of day)
NJTOT	= North pole number flux
NJTOTB	= North pole number flux with seasonal baseline removal

```
SJTOT        = South pole number flux
SJTOTB       = South pole number flux with seasonal baseline removal
RAT          = The ratio NJTOTB/SJTOTB used for determining toward
               and away sector
```

(b) Ave Counts North pole - YEAR, DAY, SECOND, (DAT(J), J=1, 20)

```
YEAR, DAY, SECOND  =  Same as above
DAT(1) to DAT (20)     =  Average counts normalized to F7 with proper
                          background and merging routines applied.  No seasonal
                          baseline correction is made.
```

(c) Same as (b) but for the south pole

Files (b) and (c) are both used to compute spectra and derive temperatures and densities for

three separate energy ranges.

4)   Polar Rain Index Generator.   This is a data structure that stores 36 daily

averages in a random access file. The user may add data to the database interactively (e.g.,

add values from parts 3a, b, c above) or extract only the data needed. The data base starts

at day 252 1977 and continues to the present. The following is a list of the data available:

```
(1)  NJTOT        - Polar rain number flux - north pole
(2)  NJTOTB       - 1) with seasonal baseline removed
(3)  NDEN (H)     - High energy density fit - north pole
(4)  NDEN (M)     - Medium energy density fit - north pole
(5)  NDEN (L)     - Low energy density fit - north pole
(6)  NTEMP (H)    - High energy temperature fit - north pole
(7)  NTEMP (M)    - Medium energy temperature fit - north pole
(8)  NTEMP (L)    - Low energy temperature fit - north pole
(9)  NCORR (H)    - High energy fit correlation - north pole
(10) NCORR (M)    - Medium energy fit correlation - north pole
(11) NCORR (L)    - Low energy fit correlation - north pole
(12) NP/SP        - (2)/(14) north/south ratio
(13) SJTOT        - (1) for south pole
(14) SJTOT-B      - (2) for south pole
(15) SDEN (H)     - (3) for south pole
(16) SDEN (M)     - (4) for south pole
(17) SDEN (L)     - (5) for south pole
(18) STEMP (H)    - (6) for south pole
(19) STEMP (M)    - (7) for south pole
(20) STEMP (L)    - (8) for south pole
(21) SCORR (H)    - (9) for south pole
(22) SCORR (M)    - (10) for south pole
(23) SCORR (L)    - (11) for south pole
(24) SOLAR-B      - Stanford Mean magnetic field
(25) IBI          - Absolute B value (IMF)
```

```
(26) BX          - X component  (IMF)
(27) BY          - Y component  (IMF)
(28) BZ          - Z component  (IMF)
(29) TEMP (SW)   - Solar wind temperature
(30) DEN (SW)    - Solar wind density
(31) VEL (SW)    - Solar wind velocity
(32) ALF-M-V     - Alfv'enic Mach Velocity
(33) AT (BX/BY)  - ATAN (BX/BY)
(34) DST         - DST
(35) KP          - Kp
(36) EQMLAT      - Equivalent Midnight Boundary
```

A typical user interaction with the polar rain index generator would be to get the list of times (year, day) with Kp greater than 5+, IMF Bz positive, and the ratio of north pole to south pole flux greater than 1. A list of all responses with the 36 values could be written as an output file for further analysis.

Outer Zone Electrons, J* Dosimeter Data Base. The J* data base also are on 9 track tapes, each tape having one file of a whole month of data. Like J3 and J4 data, it is packed and most compatible with the NOS operating system (60 bit words). The data base is limited to the F7 satellite, which was active for four years. An algorithm was developed to choose the 1 Mev peak counts of outer zone electrons. The algorithm was applied to the whole data base resulting in a data base of the selected peaks. A description of the algorithm and resulting data base is provided below.

Another task with the whole data set was to bin the various energy channels by MLAT and MLON per day and to display the results graphically to show effects before and after the magnetic storm of February 1986. Both the peak picking and binning of data were instrumental in various studies by E.G. Mullen on the radiation belts.

NASA requested a copy of the J* data set which required new software to convert the data to a more compatible format. To this end, each month of data was unpacked and

converted to 32 bit integer words and blocked appropriately for copying to a tape that could be read from most non- CYBER mainframes, particularly the VAX.

Future use of DMSP Data. With the F8, F9 and F10 satellites continuing to add to the existing data base, there is good reason to continue the routine determination of the equatorward boundary and the polar rain index. There is concern about the upcoming loss of the CYBER in September 92. Perhaps the software and file maintenance could be transferred to one of the newer machines using UNIX.

C. CRRES Projects

The CRRES satellite was launched in July, 1990 and ceased operations in October, 1991. A total of 1069 orbits of data were completed, each orbit approximately 10 hours in length. Over 20 instruments were on board, 7 of which were used by us to construct a radiation belt model. The following is a list of the instruments used:

```
701-02       SPACE RADIATION DOSIMETER (DOSIMETER)
701-04       HIGH ENERGY ELECTRON FLUX-METER (HEEF)
701-5A       MEDIUM ENERGY ANALYZER (MEA)
701-5B       ELECTRON-PROTON ANGLE SPECTROMETER (EPAS)
701-08,9     PROTON TELESCOPE (PROTEL)
701-13-1     FLUX-GATE MAGNETOMETER (MAG DATA)
ONR-307-1,2,3  SPECTROMETER FOR ELECTRONS AND PROTONS (SEP)
```

Every orbit has an ephemeris file that contains 57 values, many of which are magnetic field model values. Records are 1 minute values inside an L-SHELL of 3, otherwise they are 5 minute values.

The Time History Data Base (THDB). The THDB is provided for each instrument on a storage system called 'MASSTOR'. MASSTOR has 100 giga-bytes of memory that can be accessed by the CYBER (NOS and NOS/VE systems) and the VAX (VMS system). Access is much quicker than by the mounting of tapes. All files contain one orbit of data. Each instrument file ranges in size; the MAG data is about 2.5 mega bytes, and the

PROTEL data is about 8 mega-bytes (the SEP data can have as many as 29 mega-bytes but the files are limited and the final format may be different). The time resolution also varies by instrument. Th' DOSIMETER has a 4.096 second resolution, while the MAG data resolution is 0.128 seconds. All data records consist of 32 bit integer words with record lengths evenly divisible by 8. This makes the data quite compatible with NOS/VE, VAX and PCs. The data is usually at least partially packed and needs specific algorithms to provide real counts or values.

Software Development. Originally, all software development was done on the NOS/VE operating system, because it was most compatible with the THDB file structure and tends to have more available disk space to work with. Once debugged, the software migrates to ι VAX. The advantages of working on the VAX are that NOS/VE will not be around much longer and that VAX files are easily transported to PC hard drives. Eventually the VAX software migrates to the PC level. Since the beginning of CRRES, the programming emphasis has been moving away from mainframes and 9-track tape storage to PCs and the storage devices that come with them. Now that there is access to PCs with 300 mega-byte hard drives and devices such as WORM drives that hold 540 mega-bytes per disk and a PCSA system that uses the VAX mainframes as a PC file server, a large percentage of the work can be accomplished at the PC level. The following is a brief outline of the key software used in the processing of CRRES data:

1) File Fetching. For any given orbit there are a number of files that may be accessed. A function is in place that, given a name, will parse the name for an orbit number and instrument ID if necessary, and then search to find the file. The file might be accessed from MASSTOR with a system dependant call or just located on some other user's catalog

or directory. In this way the interactive user need only know the orbit number and an instrument ID at most when accessing the data base.

2) Ephemeris interpolation. It is convenient to be able to append an ephemeris value to any time taken from the THDB. Since the ephemeris file exists in 1 to 5 minute records, an interpolation routine exists that, given a time in UT seconds and a value of 1 to 57 that corresponds to the desired ephemeris, will return the ephemeris. For every new orbit, a new ephemeris file is fetched and loaded into an interpolation function. Two versions are available, a third degree spline (cubic) or a faster first degree spline (linear).

3) Pitch Angle Calculation. As with the ephemeris, it is convenient to be able to assign a pitch angle to a desired UT for a given instrument. Two versions are available, MODEL and REAL.

a) MODEL. The program uses the model field data from the ephemeris routine and must also fetch an attitude file for the given orbit. Once the orbit is initialized, the function will accept a UT and instrument number and return a pitch angle in degrees.

b) REAL. The program uses the magnetometer data from mass storage. Upon initialization of a new orbit, the magnetometer data is fetched along with a calibration file. The function will then accept a UT and instrument number and return a pitch angle in degrees.

4) Average Spectra. With the same software, an interactive routine is available on all systems (NOS/VE, VAX, PCs) that will ask for an orbit number, then display the beginning and ending times of the orbit if the ephemeris file was located. It will then ask for either MODEL or REAL pitch angle calculations and then proceed to loc. u the necessary files. If the necessary files are located it will then prompt for a beginning and

ending time for an average spectrum along with a pitch angle range. Instrument specific software is then used to output to a file the differential flux with the corresponding energies. The next prompt is for a new beginning and ending time, or another instrument, or another orbit, or to quit.

Other software is also in place that builds upon the four basic software packages above.

Static Radiation Belt Model. Work continues on the development of a static radiation belt model. The creation of a 1/20th of an L-SHELL file for each orbit is about 90 percent complete for PROTEL, HEEF, MEA, and DOSIMETER. Work has begun for EPAS and SEP. Each record in these files is a summation of the counts over a 1/20th of an L-shell in time. The data within this record is also sorted by energy and pitch angle (19 five degree bins). A total number of observations per bin is also stored for computing averages. There is also a complete set of EPHEMERIS files, one for each orbit, that contains 11 of the more frequently used parameters. These files are all formatted to be compatible with downloading to PCs. Batch jobs on the VAX can process a number of orbits at a time for all instruments involved and store results on the VAX scratch space (if available). The files can then be copied directly to a WORM drive using the PCSA system. Some nice PC software made available by Don Brautigam can then access these files and display the flux of the various energy channels across the whole orbit, along with the spectra for a given pitch angle bin and the pitch angle distribution for a given energy. Other uses of this data base are:

1) Merged Orbits, Mapped to the Equator. Any number of orbits may be merged to form a model for either a quiet time period or active time period. This is done by mapping the

pitch angle bin for a given L-shell and orbit to its projected equatorial pitch angle. The assembled results are then merged.

2) Loss Cone Subtraction. Code for calculating the loss cone for a given L-shell and orbit was provided by Jim Bass (RADEX). This information is used to identify contamination that can be used in background removal techniques. The process is being applied to the protel data.

Status of the CRRES Data Base. It appears that the THDB task is now finite and that routine processing of the data from the instruments discussed should be soon accomplished. There are other instruments (SEP included) that were never fully processed because of one problem or another that should soon be given a high priority. It is expected that other instruments will be added to the list of the 1/20th of an L-shell data base. This too should be accomplished in good time. More emphasis will be put on the science involved with radiation belt modeling. Eventually, the VAX and MASSTOR systems will be replaced and there is concern how that will be done. The replacement is not supposed to take place as immediately as for the CYBER. The VAX is much more compatible with any type of UNIX operating system, and much of the software is already in place on PCs.

Other Projects and Services. Software upgrades were made to accommodate the transfer of data from the NOS to the NOS\VE mainframe computers. This work applied to both the CRRES and DMSP satellites. The difference in word size between the computers required important changes in the written programs and testing of the revised logic. The magnetic tape based interface routine for the DMSP J/4 data base that runs on NOS is named EHLSJ4. The revised and modified version for NOS\VE is named VELS J4.

For the convenience and use of scientists at the Geographic Laboratory, additional services were provided in software development and modification, testing, and establishing procedures and limitations to access selected Air Force data bases onto PCs. Much CRRES data could be accessed in this manner.

Contributions were made to the development and testing of the CRRES data base itself, including search and access capabilities by users. Custom software installations were made for PC users at the Geophysics Laboratory to avoid debugging problems and to promote convenient access.

Data reduction and data analysis services were provided after the successful launch of CRRES and the onset of data transmission. Processed data was prepared for the Time History Data Base (THDB) as part of the MASSTOR system for access and use by project scientists. Data gaps, instrument performance, and the integrity of data received required much attention during CRRES operations. The development and maintenance of products for use by CRRES scientists included a file locator system, a Science Summary Data Base system, and some graphics tools.

D. Other Data Bases

<u>SCATHA - 5</u>. The SCATHA - 5 data base has been used rather sparingly. There were some event studies done in April 1979 that made use of SCATHA-5 data. Most importantly, the SCATHA data served as practice set for CRRES. Many of the binning procedures and ephemeris interpolation functions originated with SCATHA-5 because of its somewhat similar orbit and requirements for pitch angle, L-shell, and other magnetic field model ephemerides that were never a factor with DMSP. As for the status of the data, like DMSP, it is stored on 9-track tape and formatted in 60 bit binary words that are compatible with only the NOS system on the CYBER. No attempt is being made at this

time for migrating the data to a new system. If the time comes that someone needs the data, any tape can be read if it has to be.

P78-1. The P78-1 satellite was a precursor to the F2 DMSP satellite. It had a similar orbit with two J3 detectors. It was also spinning so that pitch angles were needed to sort the data. Like SCATHA-5, this data was used for an April 1979 event study and was also useful for preparing for CRRES. The status of the data is identical to that of SCATHA-5.

REFERENCES

Gussenhoven, M.S., and D. Madden, "Monitoring the Polar Rain over a Solar Cycle", J. Geophys. Res., 95, 10, 399-10, 416 (1990).

Madden, D. and M.S. Gussenhoven, Auroral Boundary Index from 1983 to 1990, 37 pp, GL-TR-90-0358, Environmental Research Papers No. 1075 (1990). ADA232845.